Mon. Not. R. Astron. Soc. **000**, 1–32 (2003) Printed 5 February 2008 (MN LaTeX style file v2.2)

Simulating cosmic rays in clusters of galaxies – II. A unified scheme for radio halos and relics with predictions of the γ-ray emission

Christoph Pfrommer,[1⋆] Torsten A. Enßlin,[2⋆] Volker Springel[2⋆]
[1]*Canadian Institute for Theoretical Astrophysics, University of Toronto, 60 St. George Street, Toronto, Ontario, M5S 3H8, Canada*
[2]*Max-Planck-Institut für Astrophysik, Karl-Schwarzschild-Straße 1, Postfach 1317, 85741 Garching, Germany*

5 February 2008

ABSTRACT
The thermal plasma of galaxy clusters lost most of its information on how structure formation proceeded as a result of dissipative processes. In contrast, non-equilibrium distributions of cosmic rays (CR) preserve the information about their injection and transport processes and provide thus a unique window of current and past structure formation processes. This information can be unveiled by observations of non-thermal radiative processes, including radio synchrotron, hard X-ray, and γ-ray emission. To explore this, we use high-resolution simulations of a sample of galaxy clusters spanning a mass range of about two orders of magnitudes, and follow self-consistent CR physics on top of the radiative hydrodynamics. We model relativistic electrons that are accelerated at cosmological structure formation shocks and those that are produced in hadronic interactions of CRs with ambient gas protons. We find that the CR proton pressure traces the time integrated non-equilibrium activities of clusters and is modulated by the recent dynamical activities. In contrast, the pressure of primary shock-accelerated CR electrons resembles current accretion and merging shock waves that break at the shallow cluster potential in the virial regions. The resulting synchrotron emission is predicted to be polarised and has an inhomogeneous and aspherical spatial distribution which matches the properties of observed radio relics. We propose a unified scheme for the generation of giant radio halos as well as radio mini-halos that naturally arises from our simulated synchrotron surface brightness maps and emission profiles. Giant radio halos are dominated in the centre by secondary synchrotron emission with a transition to the radio synchrotron radiation emitted from primary, shock-accelerated electrons in the cluster periphery. This model is able to explain the regular structure of radio halos by the dominant contribution of hadronically produced electrons. At the same time, it is able to account for the observed correlation of mergers with radio halos, the larger peripheral variation of the spectral index, and the large scatter in the scaling relation between cluster mass and synchrotron emission. Future low-frequency radio telescopes (LOFAR, GMRT, MWA, LWA) are expected to probe the accretion shock regions of clusters and the warm-hot intergalactic medium, depending on the adopted model for the magnetic fields. The hadronic origin of radio halos can be scrutinised by the detection of pion-decay induced γ-rays following hadronic CR interactions. The high-energy γ-ray emission depends only weakly on whether radiative or non-radiative gas physics is simulated due to the self-regulated nature of the CR cooling processes. Our models predict a γ-ray emission level that should be observable with the GLAST satellite.

Key words: cosmology: large-scale structure of Universe, galaxies: cluster: general, magnetic fields, cosmic rays, radiation mechanisms: non-thermal

1 INTRODUCTION

1.1 Motivation

A substantial number of luminous X-ray clusters show diffuse large-scale radio emission. Generally these radio phenomena can be divided into two categories that differ morphologically, in their degree of polarisation, as well as in their characteristic emission regions with respect to the cluster halo. The large-scale "radio relic" or "radio gischt" emission (Kempner et al. 2004), that has a high degree of polarisation, is irregularly shaped and occurs at peripheral cluster regions, can be attributed to merging or accretion shock waves as proposed by Ensslin et al. (1998). Prominent examples for large scale "radio relic" emission have been observed

⋆ e-mail: pfrommer@cita.utoronto.ca (CP); ensslin@mpa-garching.mpg.de (TAE); volker@mpa-garching.mpg.de (VS)

in Abell 3667 (Röttgering et al. 1997), Abell 3376 (Bagchi et al. 2006), and Abell 2256 (Bridle & Fomalont 1976; Masson & Mayer 1978; Bridle et al. 1979; Rottgering et al. 1994; Clarke & Enßlin 2006). In contrast, the origin of "cluster radio halos" that resemble the regular morphology of the X-ray emitting intra-cluster plasma is not understood to date. Prominent examples for "radio halo" emission can be obtained from Giovannini et al. (1999) and include the Coma cluster (Kim et al. 1989; Deiss et al. 1997) and the galaxy cluster 1E 0657-56 (Liang et al. 2000). In principle, observations of non-thermal cluster phenomena could provide an independent and complementary way of studying the growth of structure in our Universe and could shed light on the existence and the properties of the warm-hot intergalactic medium (WHIM), provided the underlying processes are understood. Sheets and filaments are predicted to host this WHIM with temperatures in the range $10^5\,\mathrm{K} < T < 10^7\,\mathrm{K}$ whose evolution is primarily driven by shock heating from gravitational perturbations breaking on mildly nonlinear, non-equilibrium structures (Hellsten et al. 1998; Cen & Ostriker 1999; Davé et al. 2001; Furlanetto & Loeb 2004; Kang et al. 2005). Once a cluster has virialised, the thermal plasma lost most information on how the formation proceeded due to the dissipative processes driving the plasma towards a Maxwell-Boltzmann momentum distribution that is characterised by its temperature only. In contrast, non-equilibrium distributions of cosmic rays preserve the information about their injection and transport processes much better, and thus provide a unique window of current and past structure formation processes.

The information about these non-equilibrium processes is encoded in the spectral and spatial distribution of cosmic ray electrons and protons. Radiative loss processes of these non-thermal particle distributions produce characteristic radio synchrotron, hard X-ray inverse Compton, and hadronically induced γ-ray emission. Suitably combining various non-thermal emission processes will allow us to infer the underlying non-equilibrium processes of clusters as well as to improve our knowledge about fundamental plasma physics. The upcoming generation of radio, hard X-ray, and γ-ray instruments opens up the extragalactic sky in unexplored wavelength ranges: low-frequency radio arrays (*GMRT*[1], *LOFAR*[2], *MWA*[3], *LWA*[4]), the future hard X-ray satellite missions *NuSTAR*[5] and *Simbol-X*, and γ-ray instruments (the *GLAST*[6] satellite and imaging atmospheric Čerenkov telescopes *H.E.S.S.*[7], *MAGIC*[8], *VERITAS*[9], and *CANGAROO*[10]) will allow us to probe non-thermal cluster physics with a multi-faceted approach. There have been pioneering efforts to simulate the non-thermal emission from clusters by numerically modelling discretised cosmic ray (CR) energy spectra on top of Eulerian grid-based cosmological simulations (Miniati 2001; Miniati et al. 2001a,b; Miniati 2002, 2003). However, these approaches neglected the hydrodynamic pressure of the CR component, were unable to resolve the observationally accessible, dense central regions of clusters, and they neglected dissipative gas physics including radiative cooling, star formation, and supernova feedback. To allow studies of the dynamical effects of CR protons in radiatively cooling galactic and cluster environments, we have developed a CR proton formalism that is based on smoothed particle hydrodynamical representation of the equations of motion. The emphasis is given to the dynamical impact of CR protons on hydrodynamics, while simultaneously allowing for the important CR proton injection and loss processes in a cosmological setting (Enßlin et al. 2007; Jubelgas et al. 2007; Pfrommer et al. 2006). This enables us to account for the pressure support provided by CR protons to the plasma of clusters of galaxies. A substantial CR proton pressure contribution might have a major impact on the properties of the intra-cluster medium (ICM) and could modify thermal cluster observables such as the X-ray emission and the Sunyaev-Zel'dovich (SZ) effect (Pfrommer et al. 2007).

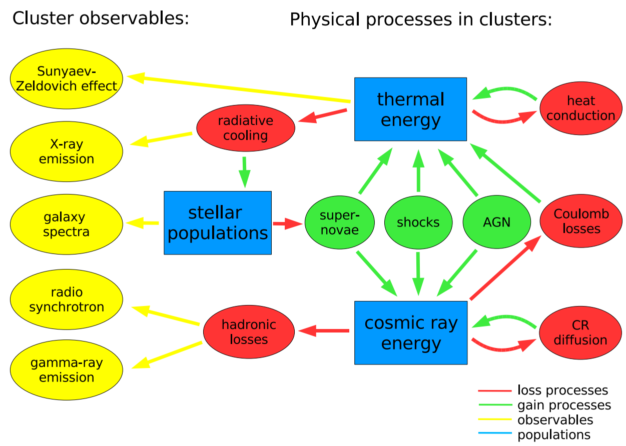

Figure 1. Overview over the relevant physical processes in galaxy clusters. The right side shows the interplay of different physical processes highlighting the interplay of the energy reservoirs of the thermal plasma and cosmic ray protons (shown in blue) while the left side shows observables that inform about the properties of clusters and their dynamical state. Gain processes are denoted in green, while loss or redistribution processes are denoted in red.

1.2 Cosmic ray physics

We give a short and simplified overview over the relevant physical processes in galaxy clusters in Fig. 1 before introducing different CR populations that are relevant for the non-thermal emission from clusters. The *upper central part* of Fig. 1 shows standard processes which are usually considered in simulations. Radiative cooling of the gas leads eventually to star formation in the densest regions that exceed a certain density threshold. This happens in the central cluster regions and within substructures leading to individual galaxies. Once the nuclear energy has been used up, massive stars explode in supernovae that drive strong shock waves into the ambient interstellar medium (ISM) which resupply thermal and turbulent energy. On larger scales, structure formation shock waves dissipate gravitational energy associated with hierarchical clustering into thermal energy of the gas, thus supplying the ICM with entropy and thermal pressure support. There are three main observables associated with these processes: the hot ICM emits thermal bremsstrahlung radiation with an X-ray luminosity that depends on the square of the electron number density. The amplitude of the Sunyaev-Zel'dovich effect (Sunyaev & Zeldovich 1972) depends

[1] **G**iant **M**eterwave **R**adio **T**elescope
[2] **LO**w **F**requency **AR**ray
[3] **M**ileura **W**idefield **A**rray
[4] **L**ong **W**avelength **A**rray
[5] **Nu**clear **S**pectroscopic **T**elescope **Ar**ray
[6] **G**amma-ray **L**arge **A**rea **S**pace **T**elescope
[7] **H**igh **E**nergy **S**tereoscopic **S**ystem
[8] **M**ajor **A**tmospheric **G**amma **I**maging **C**erenkov **T**elescope
[9] **V**ery **E**nergetic **R**adiation **I**maging **T**elescope **A**rray **S**ystem
[10] **C**ollaboration of **A**ustralia and **N**ippon for a **GA**mma **R**ay **O**bservatory in the **O**utback

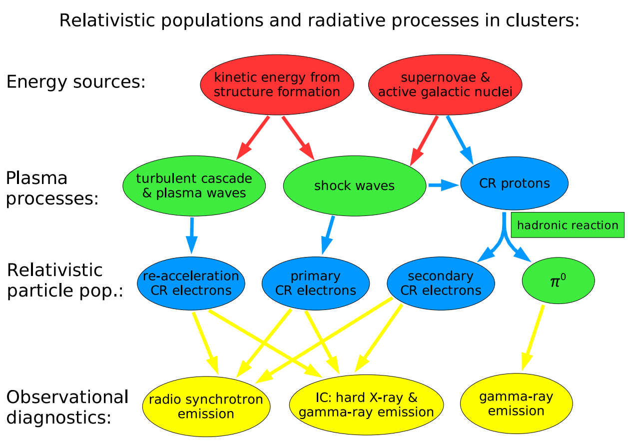

Figure 2. Schematic overview over non-thermal radiative processes in galaxy clusters. Various gravitational and non-gravitational energy sources (shown in red) are able to accelerate relativistic particle populations (shown in blue) by means of different plasma processes (shown in green). Non-thermal cluster observables (shown in yellow) are tracers of these cosmic ray populations: any cosmic ray electron population can emit radio synchrotron radiation as well as inverse Compton emission that extends from the X-ray into the γ-ray regime. In contrast, the characteristic spectral signature accompanying γ-ray emission from hadronic cosmic ray interactions is a unique sign of a cosmic ray proton population in the intra-cluster plasma.

on the pressure of the thermal electron population integrated along the line-of-sight through the cluster. Finally, galaxy spectra probe directly the stellar populations of intra-cluster galaxies and indirectly the cluster's potential through their velocity dispersion (for reviews see Sarazin 1988; Voit 2005).

The *lower part* of Fig. 1 sketches the cosmic ray physics within clusters. CR protons behave differently compared to the thermal gas. Their equation of state is softer, they are able to travel actively over macroscopic distances, and their energy loss timescales are typically larger than the thermal ones. Besides thermalization, collisionless shocks are also able to accelerate ions of the high-energy tail of the Maxwellian through diffusive shock acceleration (for reviews see Drury 1983b; Blandford & Eichler 1987; Malkov & O'C Drury 2001). These energetic ions are reflected at magnetic irregularities through magnetic resonances between the gyro-motion and waves in the magnetised plasma and are able to gain energy in moving back and forth through the shock front. This acceleration process typically yields a CR proton population with a power-law distribution of the particle momenta. CRs are accelerated on galactic scales through supernova shocks while they are injected by structure formation shock waves on even larger scales up to tens of Mpc. So far, we have neglected feedback from active galactic nuclei (AGN) in our simulations despite its importance (for first numerical simulations of thermal 'radio-mode' feedback within cosmological simulations, see Sijacki & Springel 2006). Gravitational energy associated with the accretion onto super-massive black holes is converted into large-scale jets and eventually dissipated into thermal and CR energy.

The ubiquitous cosmic magnetic fields couple the otherwise dynamically independent ingredients like the ICM plasma, and the CR gas into a single, however complex fluid. Magnetic fields prevent charged relativistic particles to travel macroscopic distances with their intrinsic velocity close to the speed of light. Instead, the particles gyrate around, and travel slowly along magnetic field lines. Occasionally, they get scattered on magnetic irregularities. On macroscopic scales, the transport can often be described as a diffusion process that redistributes the CR energy density macroscopically provided the gyro-radius of charged relativistic particles can be regarded to be small. Thus, the diffusive CR transport in tangled magnetic fields effectively confines the CRs with energies $E < 2 \times 10^7$ GeV to clusters and yields to CR proton lifetimes of the order of the Hubble time (Völk et al. 1996; Ensslin et al. 1997; Berezinsky et al. 1997; Colafrancesco & Blasi 1998), long enough to diffuse away from the production site and to maintain a space-filling distribution over the cluster volume. Thermal heat conduction is an analogous process that reallocates the thermal energy of the ICM.

The CR energy reservoir suffers two main loss processes: (1) CR energy is transferred into the thermal energy reservoir through individual electron scatterings in the Coulomb field of the CR particle as well as by small momentum transfers through excitations of quantised plasma oscillations. We refer to the sum of both effects as Coulomb losses (Gould 1972a). (2) Provided the CR momentum exceeds the threshold $p \simeq 0.8\,\mathrm{GeV}/c$ for the hadronic reaction with ambient protons, they produce pions which decay into secondary electrons, positrons, neutrinos, and γ-rays:

$$\begin{aligned}\pi^\pm &\rightarrow \mu^\pm + \nu_\mu/\bar{\nu}_\mu \rightarrow e^\pm + \nu_e/\bar{\nu}_e + \nu_\mu + \bar{\nu}_\mu\\ \pi^0 &\rightarrow 2\gamma\,.\end{aligned}$$

Only CR protons above this kinematic threshold are therefore visible through their decay products via radiative processes, making them directly observationally detectable. As shown in Fig. 2, these *secondary relativistic electrons and positrons* can emit a halo of radio synchrotron emission in the presence of ubiquitous intra-cluster magnetic fields (Dennison 1980; Vestrand 1982; Blasi & Colafrancesco 1999; Dolag & Enßlin 2000; Miniati et al. 2001b; Pfrommer & Enßlin 2003, 2004a,b; Marchegiani et al. 2007) as well as inverse Compton emission by scattering photons from the cosmic microwave background into the hard X-ray and γ-regime.[11] Future γ-ray satellites should be able to detect the associated hadronically induced γ-ray emission resulting from neutral pion decay and allow unambiguous conclusions on the parent CR population in clusters.

Structure formation shocks can also directly accelerate so-called *primary CR electrons* giving rise to an irregularly shaped radio and inverse Compton morphology due to the comparatively short synchrotron lifetimes of CR electrons of $\tau \simeq 10^8$ yr. To complicate this picture even more, there are other processes that accelerate relativistic electrons. Re-acceleration processes of 'mildly' relativistic electrons ($\gamma \simeq 100 - 300$) that are being injected over cosmological timescales into the ICM by sources like radio galaxies, supernova remnants, merger shocks, or galactic winds can provide an efficient supply of highly-energetic CR electrons. Owing to their long lifetimes of a few times 10^9 years these 'mildly' relativistic electrons can accumulate within the ICM (Sarazin 2002), until they experience continuous in-situ acceleration either via interactions with magneto-hydrodynamic waves, or through turbulent spectra (Jaffe 1977; Schlickeiser et al. 1987; Brunetti et al. 2001; Ohno et al. 2002; Brunetti et al. 2004; Brunetti & Lazarian 2007). This gives rise to a third population of *re-accelerated CR electrons* that also contributes to the observed radio and inverse Compton emission. Since the distribution of magnetic field strengths with

[11] In the following, we use the term secondary CR electrons synonymously for the likewise produced electrons and positrons.

cluster radius is also not well known, radio synchrotron emission alone has limited predictive power. Unfortunately, the conceptually simpler inverse Compton emission is hard to observe because of the strong radiation background in the soft and hard X-ray regime.

Nevertheless, there seems to be growing evidence for an excess of hard X-ray emission compared to the expected thermal bremsstrahlung in a number of clusters that is based on observations with instruments on board five different X-ray satellites. Prominent examples include the Coma cluster (Rephaeli et al. 1999; Fusco-Femiano et al. 1999; Rephaeli & Gruber 2002; Fusco-Femiano et al. 2004, 2007;[12] Eckert et al. 2007; using the *Rossi X-ray Timing Explorer* (*RXTE*), *BeppoSAX*, and *INTEGRAL*) , the "Bullet" cluster 1ES 0657–558 (Petrosian et al. 2006, using *RXTE*), Abell 2256 (Rephaeli & Gruber 2003, using *RXTE*), the Ophiuchus cluster (Eckert et al. 2007, using *INTEGRAL*), and the Perseus cluster (Sanders et al. 2005; Molendi 2007, using *Chandra* and *XMM-Newton*). The currently favoured theoretical explanation of inverse Compton radiation by CR electrons faces problems since the magnetic field estimates inferred by combining synchrotron and inverse Compton emission are much smaller than those derived from Faraday rotation measurements (cf. Pfrommer 2007, for an extensive discussion). It has been proposed that a fraction of the diffuse cosmological γ-ray background radiation originates from the same processes (Loeb & Waxman 2000; Miniati 2002; Reimer et al. 2003; Berrington & Dermer 2003; Kuo et al. 2005).

This paper studies directly the CR related multi-frequency observables aiming at understanding the cluster radio halo emission. In a companion paper, we study the interplay of thermal gas and CRs and their effect on the observables of the thermal gas such as X-ray emission and the Sunyaev-Zel'dovich effect (Pfrommer et al. 2007, hereafter Paper I). For consistency reasons with that paper, we scale cluster masses and length units with the dimensionless Hubble constant, h, where $H_0 = 100\,h$ km s^{-1} Mpc^{-1}. However, non-thermal surface brightness and luminosities (for radio, hard X-ray, and γ-ray emission) are reported in units of the currently favoured Hubble constant, h_{70}, where $H_0 = 70\,h_{70}$ km s^{-1} Mpc^{-1} since primary and secondary emission processes have a different scaling with h. We derive cluster scaling relations for non-thermal observables and compare our results to observations in our follow-up paper (Pfrommer 2007, hereafter Paper III).

The outline of the paper is as follows. Section 2 describes our methodology including the general setup of the simulations, our cluster sample, the different physical processes which we simulated, and highlights important properties of radiative processes considered in this work. In Sect. 3, we present and interpret the results on the line-of-sight projections and emission profiles of the different non-thermal emission mechanisms, and correlations of various non-thermal emission processes with the thermal X-ray emission. We compare our results to previous findings in the literature and point out future theoretical work that is needed to complement this work (cf. Sect. 4). The conclusions are drawn in Sect. 5. Appendix A describes the modelling of the primary and secondary CR electron population while Appendix B describes the formulae of the non-thermal emission mechanisms ranging from radio synchrotron radiation, inverse Compton emission, as well as hadronically induced γ-ray emission.

[12] The results of these papers have been challenged by an analysis that takes into account all systematic uncertainties in the critical parameters including the choice of a source-free background field and the modelling of the thermal model for the ICM (Rossetti & Molendi 2004, 2007).

2 METHODOLOGY

2.1 General approach

We follow the CR proton pressure dynamically in our simulations while taking into account all relevant CR injection and loss terms in the ICM, except for a possible production of CR protons by AGN. In contrast, we model the CR electron population in a post-processing step since it does not modify the hydrodynamics owing to its negligible pressure contribution. In this paper, we concentrate on three observationally motivated wave-bands. (1) Radio synchrotron emission between 15 MHz and 1.4 GHz, (2) non-thermal hard X-ray emission at energies $E_\gamma > 10$ keV, and (3) γ-ray emission at energies $E_\gamma > 100$ MeV. Studying our simulated radio synchrotron maps and emission profiles, we develop a *unified scheme* for the generation of the diffuse large scale radio emission of clusters such as giant radio halos, mini-halos, as well as the radio relic emission.[13]

2.2 The simulations

2.2.1 General setup and cluster sample

This section provides a short overview of the simulations and physical models used. Further details can be found in Paper I. All simulations were performed using the "concordance" cosmological cold dark matter model with a cosmological constant (ΛCDM). The cosmological parameters of our model are: $\Omega_\mathrm{m} = \Omega_\mathrm{DM} + \Omega_\mathrm{b} = 0.3$, $\Omega_\mathrm{b} = 0.039$, $\Omega_\Lambda = 0.7$, $h = 0.7$, $n = 1$, and $\sigma_8 = 0.9$. Here, Ω_m denotes the total matter density in units of the critical density for geometrical closure today, $\rho_\mathrm{crit} = 3H_0^2/(8\pi G)$. Ω_b and Ω_Λ denote the densities of baryons and the cosmological constant at the present day. The Hubble constant at the present day is parametrised as $H_0 = 100\,h$ km s^{-1}Mpc^{-1}, while n denotes the spectral index of the primordial power-spectrum, and σ_8 is the *rms* linear mass fluctuation within a sphere of radius 8 h^{-1}Mpc extrapolated to $z = 0$.

Our simulations were carried out with an updated and extended version of the distributed-memory parallel TreeSPH code GADGET-2 (Springel 2005; Springel et al. 2001) that includes self-consistent cosmic ray physics (Enßlin et al. 2007; Jubelgas et al. 2007; Pfrommer et al. 2006). Gravitational forces were computed using a combination of particle-mesh and tree algorithms. Hydrodynamic forces are computed with a variant of the smoothed particle hydrodynamics (SPH) algorithm that conserves energy and entropy where appropriate, i.e. outside of shocked regions (Springel & Hernquist 2002).

We have performed high-resolution hydrodynamic simulations of the formation of 14 galaxy clusters. The clusters span a mass range from $5 \times 10^{13}\,h^{-1}\,\mathrm{M}_\odot$ to $2 \times 10^{15}\,h^{-1}\,\mathrm{M}_\odot$ and show a variety of dynamical states ranging from relaxed cool core clusters to violent merging clusters (cf. Table 1). The clusters have originally been selected from a low-resolution dark-matter-only simulation (Yoshida et al. 2001). Using the 'zoomed initial conditions' technique (Katz & White 1993), the clusters have been re-simulated with higher mass and force resolution by adding short-wavelength modes within the Lagrangian regions in the initial conditions that

[13] Our 'unified scheme' unifies apparently different diffuse radio phenomena in clusters (giant relics, halos, and mini-halos) with a simple and physically motivated model. The 'unified scheme' should not be confused with a 'complete model' and we want to point out that we have not accounted for all possible CR processes that could be of interest in the context of cluster physics.

Table 1. : CLUSTER SAMPLE

Cluster	sim.'s	dyn. state$^{(1)}$	$M_{200}^{(2)}$ [$h^{-1}\,\mathrm{M}_\odot$]	$R_{200}^{(2)}$ [h^{-1} Mpc]	$kT_{200}^{(3)}$ [keV]
1	g8a	CC	1.8×10^{15}	2.0	13.1
2	g1a	CC	1.3×10^{15}	1.8	10.6
3	g72a	PostM	1.1×10^{15}	1.7	9.4
4	g51	CC	1.1×10^{15}	1.7	9.4
5	g1b	M	3.7×10^{14}	1.2	4.7
6	g72b	M	1.5×10^{14}	0.87	2.4
7	g1c	M	1.4×10^{14}	0.84	2.3
8	g8b	M	1.0×10^{14}	0.76	1.9
9	g1d	M	9.2×10^{13}	0.73	1.7
10	g676	CC	8.8×10^{13}	0.72	1.7
11	g914	CC	8.5×10^{13}	0.71	1.6
12	g1e	M	6.4×10^{13}	0.65	1.3
13	g8c	M	5.9×10^{13}	0.63	1.3
14	g8d	PreM	5.4×10^{13}	0.61	1.2

NOTES:
(1) The dynamical state has been classified through a combined criterion invoking a merger tree study and the visual inspection of the X-ray brightness maps. The labels for the clusters are M–merger, PostM–post merger (slightly elongated X-ray contours, weak cool core region developing), PreM–pre-merger (sub-cluster already within the virial radius), CC–cool core cluster with extended cooling region (smooth X-ray profile).
(2) The virial mass and radius are related by $M_\Delta(z) = \frac{4}{3}\pi\,\Delta\,\rho_{\mathrm{crit}}(z)R_\Delta^3$, where $\Delta = 200$ denotes a multiple of the critical overdensity $\rho_{\mathrm{crit}}(z) = 3H(z)^2/(8\pi G)$.
(3) The virial temperature is defined by $kT_\Delta = GM_\Delta\,\mu\,m_{\mathrm{p}}/(2R_\Delta)$, where μ denotes the mean molecular weight.

will evolve later-on into the structures of interest (Paper I). We re-simulated three isolated clusters (cluster 4, 10, and 11) and three super-cluster regions which are each dominated by a large cluster (cluster 1, 2, and 3) and surrounded by satellite clusters (cluster 5 to 9 and 12 to 14). In high-resolution regions, the dark matter particles had masses of $m_{\mathrm{DM}} = 1.13\times10^9\,h^{-1}\,\mathrm{M}_\odot$ and SPH particles had $m_{\mathrm{gas}} = 1.7\times10^8\,h^{-1}\,\mathrm{M}_\odot$ so each individual cluster is resolved by 8×10^4 to 4×10^6 particles, depending on its final mass. The SPH densities were computed from 48 neighbours, allowing the SPH smoothing length to drop at most to half of the value of the gravitational softening length of the gas particles. This choice of the SPH smoothing length leads to our minimum gas resolution of approximately $8\times10^9\,h^{-1}\,\mathrm{M}_\odot$. For the initial redshift we chose $1+z_{\mathrm{init}} = 60$. The gravitational force softening was of a spline form (e.g., Hernquist & Katz 1989) with a Plummer equivalent softening length that is assumed to have a constant comoving scale down to $z = 5$, and a constant value of $5\,h^{-1}$kpc in physical units at later epochs.

We analysed the clusters with a halo-finder based on spherical overdensity followed by a merger tree analysis in order to get the mass accretion history of the main progenitor. We also produced projections of the X-ray emissivity at redshift $z = 0$ in order to get a visual impression of the cluster morphology. The dynamical state of a cluster is defined by a combined criterion: (i) if the cluster did not experience a major merger with a progenitor mass ratio 1:3 or larger after $z = 0.8$ (corresponding to a look-back time of $\sim 5\,h^{-1}$ Gyr) and (ii) if the visual impression of the cluster's X-ray morphology is relaxed, it was defined to be a cool core cluster. The spherical overdensity definition of the virial mass of the cluster is given by the material lying within a sphere centred on a local density maximum, whose radial extend R_Δ is defined by the enclosed

Table 2. : DIFFERENT PHYSICAL PROCESSES IN OUR SIMULATIONS:

Simulated physics$^{(1)}$	simulation models$^{(1)}$: S1	S2	S3
thermal shock heating	✓	✓	✓
radiative cooling		✓	✓
star formation		✓	✓
Coulomb CR losses	✓	✓	✓
hadronic CR losses	✓	✓	✓
shock-CRs	✓	✓	✓
supernova-CRs			✓

NOTES:
(1) This table serves as an overview over our simulated models. The first column shows the simulated physics and the following three columns show our different simulation models with varying gas and cosmic ray physics. Model S1 models the thermal gas non-radiatively and includes CR physics, while the models S2 and S3 use radiative gas physics with different variants of CR physics.

threshold density condition $M(<R_\Delta)/(4\pi R_\Delta^3/3) = \rho_{\mathrm{thres}}$. We chose the threshold density $\rho_{\mathrm{thres}}(z) = \Delta\,\rho_{\mathrm{crit}}(z)$ to be a multiple $\Delta = 200$ of the critical density of the universe $\rho_{\mathrm{crit}}(z) = 3H(z)^2/(8\pi G)$. We assume a constant $\Delta = 200$ although some treatments employ a time-varying Δ in cosmologies with $\Omega_{\mathrm{m}} \neq 1$ (Eke et al. 1996). In the reminder of the paper, we use the terminology R_{vir} instead of R_{200}.

2.2.2 The models

For each galaxy cluster we ran three different simulations with varying gas and cosmic ray physics (cf. Table 2). The first set of simulations used non-radiative gas physics only, i.e. the gas is transported adiabatically unless it experiences structure formation shock waves that supply the gas with entropy and thermal pressure support. Additionally we follow cosmic ray (CR) physics including adiabatic CR transport processes, injection by cosmological structure formation shocks with a Mach number dependent acceleration scheme, as well as CR thermalization by Coulomb interaction and catastrophic losses by hadronic interactions (model S1). The second set of simulations follows the radiative cooling of the gas, star formation, supernova feedback, and a photo-ionising background (details can be found in Paper I). As before in model S1, we account for CR acceleration at structure formation shocks and allow for all CR loss processes (model S2). The last set of simulations additionally assumes that a constant fraction $\zeta_{\mathrm{SN}} = \varepsilon_{\mathrm{CR,inj}}/\varepsilon_{\mathrm{diss}} = 0.3$ of the kinetic energy of a supernova ends up in the CR population (model S3), which is motivated by TeV γ-ray observations of a supernova remnant that find an energy fraction of $\zeta_{\mathrm{SN}} \simeq 0.1-0.3$ when extrapolating the CR distribution function (Aharonian et al. 2006). We choose a maximum value for this supernova energy efficiency owing to the large uncertainties and our aim to bracket the realistic case with the two radiative CR simulations. Generally, we use model S2 as our standard case which is a conservative choice for the CR pressure and explore how the physics of the other models change the resulting non-thermal cluster observables. In this work, we don't account for AGN sources of cosmic rays, but that this will be addressed in upcoming work (Sijacki et al. 2007).

Radiative cooling was computed assuming an optically thin gas of primordial composition (mass-fraction of $X_{\mathrm{H}} = 0.76$ for hydrogen and $1 - X_{\mathrm{H}} = 0.24$ for helium) in collisional ionisation equilibrium, following Katz et al. (1996). We have also included heating by a photo-ionising, time-dependent, uniform ultraviolet (UV) background expected from a population of quasars (Haardt & Madau 1996), which reionises the Universe at $z \simeq 6$. Star formation is treated using the hybrid multiphase model for the interstellar medium introduced by Springel & Hernquist (2003). In short, the ISM is pictured as a two-phase fluid consisting of cold clouds that are embedded at pressure equilibrium in an ambient hot medium. The clouds form from the cooling of high density gas, and represent the reservoir of baryons available for star formation. When stars form, the energy released by supernovae heats the ambient hot phase of the ISM, and in addition, clouds in supernova remnants are evaporated. These effects establish a tightly self-regulated subresolution model for star formation in the ISM.

Cosmic ray physics was computed by using a new formulation that follows the most important injection and loss processes self-consistently while accounting for the CR pressure in the equations of motion (Enßlin et al. 2007; Jubelgas et al. 2007; Pfrommer et al. 2006). We refer to these papers for a detailed description of the formalism, providing here only a short summary of the model. In our methodology, the non-thermal cosmic ray population of each gaseous fluid element is approximated by a simple power law spectrum in particle momentum, characterised by an amplitude, a low-momentum cut-off, and a fixed slope $\alpha = 2.3$. This choice is justified by taking the mean of the Mach number distribution weighted by the dissipated energy at shocks which is closely related to the spectral index of a CR power-law distribution (Paper I). Adiabatic CR transport processes such as compression and rarefaction, and a number of physical source and sink terms which modify the cosmic ray pressure of each particle are modelled. The most important sources considered are injection by supernovae (in our radiative simulations) and diffusive shock acceleration at cosmological structure formation shocks, while the primary sinks are thermalization by Coulomb interactions, and catastrophic losses by hadronic interactions.

2.3 Essentials of radiative processes

We are interested in the non-thermal emission of the inter-galactic medium at radio frequencies ($\nu > 10$ MHz) as well as at hard X-ray/γ-ray energies ($E_\gamma > 10$ keV). This non-thermal emission is generated by CR electrons with energies $E_\mathrm{e} >$ GeV as can be readily inferred from the classical synchrotron and inverse Compton formulae,

$$\nu_\mathrm{synch} = \frac{3eB}{2\pi\, m_\mathrm{e} c}\,\gamma^2 \simeq 1\,\mathrm{GHz}\,\frac{B}{\mu\mathrm{G}}\left(\frac{\gamma}{10^4}\right)^2, \quad (1)$$

$$h\nu_\mathrm{IC} = \frac{4}{3}\,h\nu_\mathrm{init}\,\gamma^2 \simeq 90\,\mathrm{keV}\,\frac{\nu_\mathrm{init}}{\nu_\mathrm{CMB}}\left(\frac{\gamma}{10^4}\right)^2, \quad (2)$$

where e denotes the elementary charge, h the Planck constant, c the speed of light, m_e the electron mass, the particle kinetic energy $E/(m_\mathrm{e}c^2) = \gamma - 1$ is defined in terms of the Lorentz factor γ, and $B = \sqrt{\langle \boldsymbol{B}^2\rangle}$ is the *rms* of the magnetic vector field $\boldsymbol{B}$. We chose CMB photons $h\nu_\mathrm{CMB} \simeq 0.66$ meV as source for the inverse Compton emission using Wien's displacement law. Thus, the same CR electron population seen in the radio band via synchrotron emission can be observed in the hard X-ray regime through the IC process.

2.3.1 *Synchrotron and IC emission from equilibrium spectra*

The synchrotron and IC emissivities of an equilibrium distribution of CR electrons is characterised by two distinctive regimes.

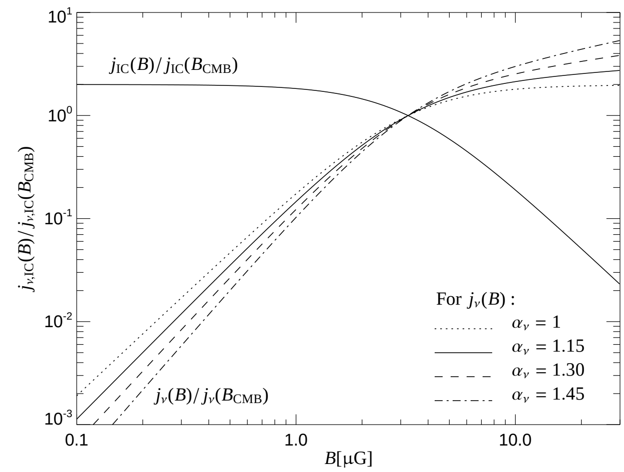

Figure 3. The synchrotron and inverse Compton (IC) emissivity of an equilibrium distribution of CR electrons is shown for various spectral indices α_ν. The normalisation is given by the respective emissivities at the equivalent magnetic field strength of the energy density of the CMB, $B_\mathrm{CMB} = 3.24\,\mu$G. The weak field regime on the left-hand side is characterised by the dominant inverse Compton (IC) emission while the strong field regime on the right side has the synchrotron emission as the dominant electron cooling channel.

The weak field regime is characterised by the dominating IC emission while the strong field regime has the synchrotron emission as the dominant electron cooling channel. Using the formulae for the equilibrium distribution of CR electrons (Eqns. (A35) or (A48)), the synchrotron and IC emissivities depend on the magnetic field strength as follows:

$$j_\nu \propto \frac{B^{\alpha_\nu+1}}{\varepsilon_B + \varepsilon_\mathrm{CMB}} \quad \text{and} \quad j_\mathrm{IC} \propto \frac{1}{\varepsilon_B + \varepsilon_\mathrm{CMB}}, \quad (3)$$

where α_ν denotes the synchrotron spectral index that is defined by $j_\nu \propto \nu^{-\alpha_\nu}$, and $\varepsilon_B = B^2/(8\pi)$. Figure 3 shows these emissivities, normalised by respective emissivities at the equivalent magnetic field strength of the CMB energy density at $z = 0$, $B_\mathrm{CMB} = 3.24\,\mu$G. In the IC dominated electron cooling regime leftwards of B_CMB, the synchrotron emissivity quickly decreases relative to the IC emissivity, showing thus a strong dependence on the magnetic field strength. There is an interesting twist associated with the different spectral indices of the synchrotron emission in clusters. Paper I shows that the characteristic shock strength increases as one moves outwards from the cluster centre due to the decrease of the sound velocity in combination with the shallower peripheral cluster potential. CR acceleration crucially depends on the shock strength according to Eqn. (A19) predicting steep CR spectra at the centre that flatten on average towards the cluster periphery. Since the magnetic field has a decreasing profile with radius (Eqn. 5), the synchrotron emission of clusters should qualitatively be given by the upper envelope of the family of emissivity curves labelled by different spectral indices of Fig. 3. This simplified picture assumes that the electron spectra are dominated by injection and are neither qualitatively modified by CR transport processes such as CR diffusion nor by the hadronically injected electron spectra.

2.3.2 *Comparison of inverse Compton and γ-ray spectra*

Figure 4 compares the spectral distribution of the pion-decay induced γ-ray emission (broken power-laws) with the inverse Comp-

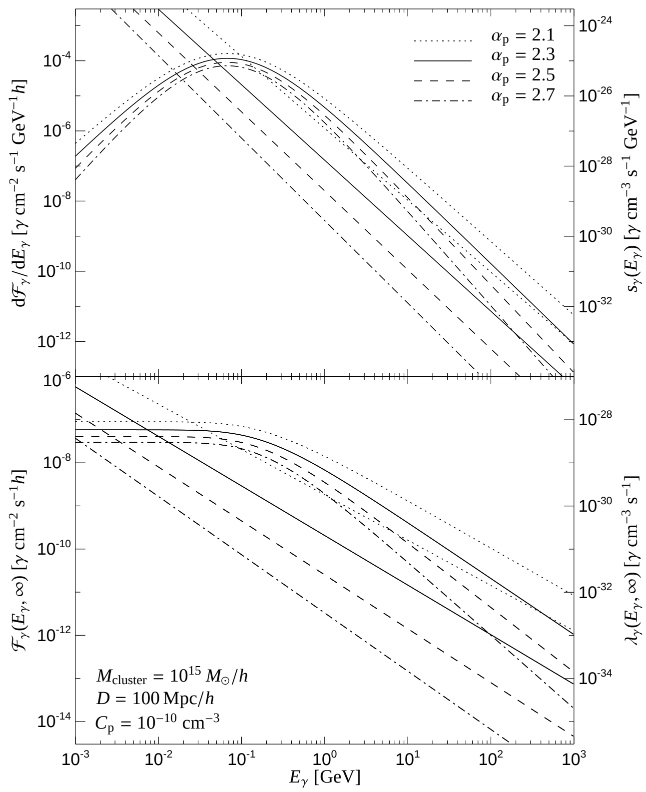

Figure 4. Spectral distribution of the differential γ-ray flux $\mathrm{d}\mathcal{F}_\gamma/\mathrm{d}E_\gamma$ (upper panel) and the integrated γ-ray flux $\mathcal{F}_\gamma(E_\gamma,\infty)$ (bottom panel) for different spectral indices. Shown are inverse Compton spectra from a secondary CR electron population and pion decay induced γ-ray spectra (broken power-laws) both resulting from hadronic CR proton interactions. The model calculations assume a normalisation for the CR proton distribution of $C_\mathrm{p} = 10^{-10}\,\mathrm{cm}^{-3}$, a nucleon density of $n_\mathrm{N} = 10^{-3}\,\mathrm{cm}^{-3}$ (for λ_γ), and put the fiducial cluster with mass $M_\mathrm{cluster} = 10^{15}\,M_\odot/h$ at a distance $D = 100\,\mathrm{Mpc}/h$ to derive $\mathcal{F}_\gamma$.

ton emission both resulting from hadronic CR proton interactions. Note, that the relative normalisation of both emission components is governed by hadronic physics and does not depend on the gas and CR proton number densities. For our choice of the CR proton spectral index of $\alpha_\mathrm{p} = 2.3$, the ratio of pion-decay to secondary IC emission in the energy range $E_\gamma > 100$ MeV can be readily inferred to be $\mathcal{F}_\gamma/\mathcal{F}_\mathrm{IC} = 20$. The asymptotic behaviour for the γ-ray number flux of both emission components at high energies is given by

$$\mathcal{F}_\gamma \propto E_\gamma^{-\alpha_\mathrm{p}+1} \quad \text{and} \quad \mathcal{F}_\mathrm{IC} \propto E_\gamma^{-\alpha_\nu} = E_\gamma^{-\alpha_\mathrm{p}/2}. \tag{4}$$

Assuming a spectral CR index of $\alpha_\mathrm{p} = 2$ yields the same asymptotic behaviour while increasing α_p results in a shallower decline for $\mathcal{F}_\mathrm{IC}$ with energy such that eventually the IC component will surpass the pion decay emission. This however is well above the energy range $E_\gamma \gg 10$ TeV that is of interest for imaging air Čerenkov telescopes. For an energy range $E_\gamma < 1$ MeV the secondary IC emission dominates the hadronically induced channel. In contrast to the secondary IC emission, the IC emission level of primary CR electrons depends on the dynamical activity of the region, in particular on the shock strength and the associated amount of dissipated energy. Comparing the primary to the secondary IC emission will be one goal of this paper.

3 RESULTS

3.1 Cluster environment and cosmic ray pressure

Figure 5 shows the region around the largest cluster with merging activity in our sample ($M \simeq 10^{15} h^{-1}\,\mathrm{M}_\odot$, with the identifier g72a) in our simulation with radiative gas physics, star formation, and CRs from structure formation shocks only (model S2). This galaxy cluster experienced a large merger with a mass ratio of $m_\mathrm{merger}/m_\mathrm{progenitor} = 0.3$ at redshift $z = 0.25$ preceded by a minor merger mass ratio of $m_\mathrm{merger}/m_\mathrm{progenitor} = 0.1$ at $z = 0.4$. The environment is dominated by the large central post-merging cluster and surrounded by smaller satellite clusters and groups. The line-of sight average of the density shows the suitably normalised quantity $1 + \delta_\mathrm{gas} = \rho/(\Omega_\mathrm{b}\,\rho_\mathrm{crit})$. While the ICM of the central massive cluster reaches central temperatures above that of the virial temperature of $kT_\mathrm{vir} = 9.4$ keV, the surrounding warm-hot intergalactic medium (WHIM) acquires temperatures of $kT \sim (10^{-2}–10^{-1})$ keV. The spatial distribution of shock strengths can be studied best by looking at the Mach numbers weighted by the energy dissipation rate at structure formation shocks (represented by the colour hue in the bottom left panel of Fig. 5). The brightness scales logarithmically with the projected dissipation rate $\langle\dot{\varepsilon}_\mathrm{diss}\rangle_\mathrm{los}$. Within this super-cluster region most of the energy is dissipated in weak internal shocks with Mach numbers $\mathcal{M} \lesssim 2$ which are predominantly central flow shocks or merger shock waves traversing the cluster centre. Collapsed cosmological structures are surrounded by several quasi-spherical shells of external shocks with successively higher Mach numbers, but they play only a minor role in the energy balance of thermalization as can be inferred by its dim brightness. Clearly visible are spherical shells of shocks at different radii from the cluster centre. Two distinct outgoing shock waves at distances of 2 and 3 h^{-1} Mpc to the cluster centre are visible that are triggered by the merger, followed by shells of stronger shocks further outwards. This picture is dramatically changed if we perform the weighting of the Mach numbers with the energy injection rate of CR protons, $\dot{\varepsilon}_\mathrm{CR}$ (shown in colour while the brightness displays the logarithm of the CR proton energy injection rate, bottom right side). Only CR protons with a dimensionless momentum $q = \beta\gamma > 30$ ($E \gtrsim 30$ GeV) have been considered for calculating the CR energy density since lower energetic CR protons are not detectable at radio frequencies $\nu > 120$ MHz by means of hadronically produced secondary electrons (assuming $B = 1\,\mu$G). As expected, weak shocks with Mach numbers $1 < \mathcal{M} < 2$ almost disappear in this representation due to their small acceleration efficiency. This effect is amplified by considering only energetic CR protons with $q > 30$. Comparing the Mach numbers weighted by $\dot{\varepsilon}_\mathrm{CR}$ to those weighted by $\dot{\varepsilon}_\mathrm{diss}$ uncovers the three-dimensional picture of these shock surfaces. The powerful (in terms of energy dissipation rate) but weak (in terms of shock strength) internal shock waves are surrounded by shock surfaces of successively increasing Mach numbers that are only revealed in these projections if one disfavours these internal shocks in the weighting function.

What are the consequences for the CR proton pressure within galaxy clusters? Similar to the thermal pressure, it peaks in the centre and falls of with radius. The CR pressure is additionally enhanced at strong shock waves, that have a modulating effect on the underlying CR pressure distribution. The latter can be seen by looking at the strong tangential shock wave at $r \simeq 600\,h^{-1}$ kpc southwards from the cluster centre in the mass weighted CR proton pressure map (top left panel in Fig. 6). The CR pressure peaks roughly at $P_\mathrm{CR} \simeq 10^{-12}\mathrm{erg\ cm}^{-3}\,h_{70}^2$ at the cluster centre. Even more revealing is the mass-weighted CR proton pressure relative to the total

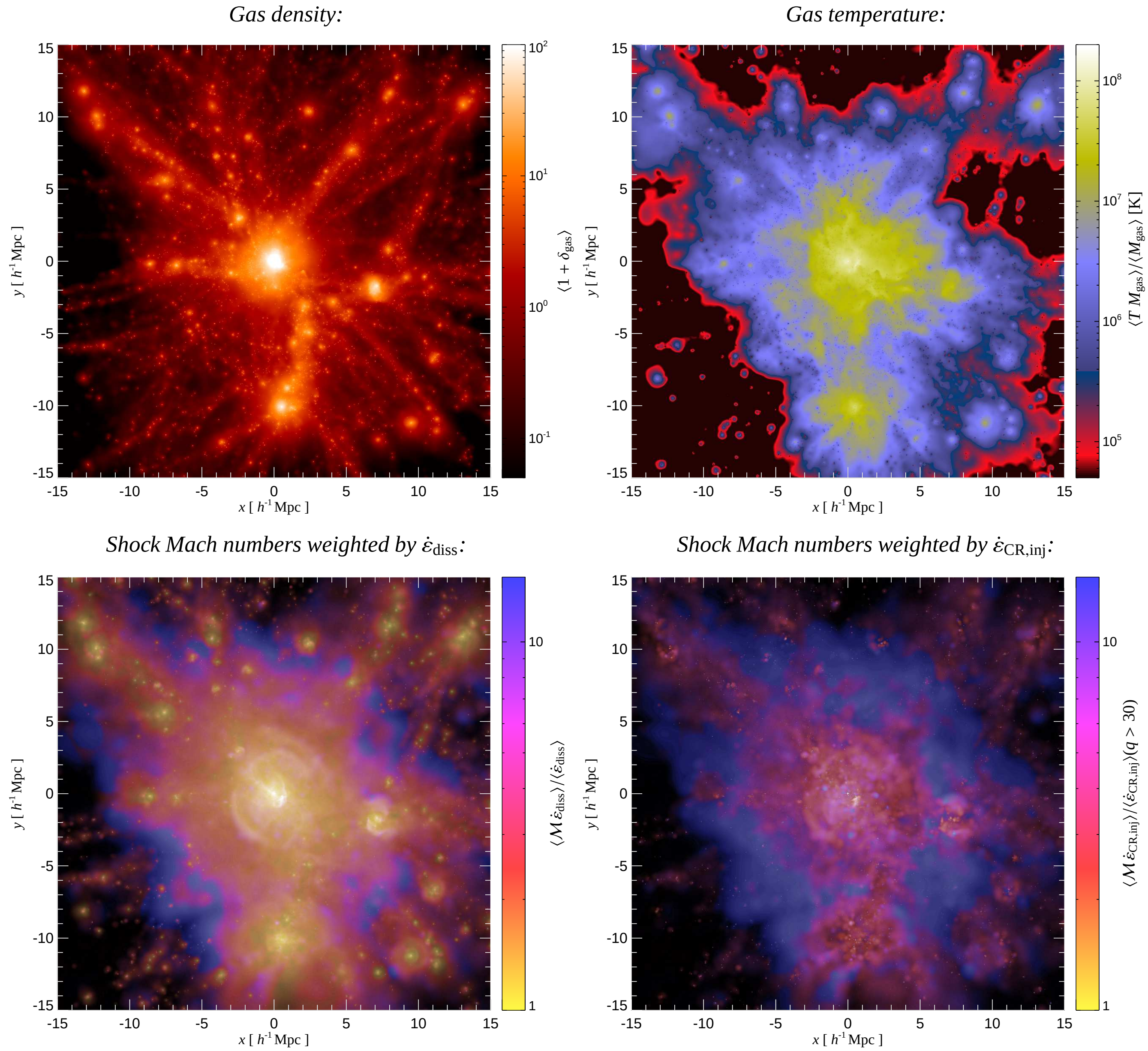

Figure 5. The environment of a large post-merging galaxy cluster ($M \simeq 10^{15} h^{-1}\,\mathrm{M}_\odot$) in our simulation with radiative gas physics and star formation including CRs from structure formation shocks only (model S2). Shown are the line-of-sight averaged density (top left side), the mass weighted temperature (top right side), the Mach number of shocks weighted by the energy dissipation rate in colour (while the brightness displays the logarithm of the dissipation rate, bottom left side), and the Mach number of shocks weighted by the energy injection rate of CR protons in colour (while the brightness displays the logarithm of the CR proton energy injection rate, bottom right side). For better comparison, we used the same colour and brightness scale in the bottom plots. Only CR protons with a dimensionless momentum $q = \beta\gamma > 30$ have been considered for calculating the CR energy density since lower energetic CR protons are not detectable at radio frequencies $\nu > 120$ MHz by means of hadronically produced secondary electrons.

pressure $X_{\rm CR} = P_{\rm CR}/P_{\rm tot}$, where $P_{\rm tot} = P_{\rm CR} + P_{\rm th}$ (top right panel in Fig. 6). The relative CR pressure $X_{\rm CR}$ acquires comparatively high values within the WHIM that are hydrodynamically important, their importance decreases (on average) as we move inwards due to a combination of the following reasons: (1) weak central flow shocks are inefficient in accelerating CRs (e.g., Paper I) and (2) adiabatic compression of a composite of CRs and thermal gas disfavours the CR pressure relative to the thermal pressure due to the softer equation of state of CRs. Within each individual galaxy as well as within the cluster centre, the CR pressure reaches equipartition or dominates the thermal pressure as can be seen by the numerous yellow points sprinkled over the map, each corresponding to a galaxy. This is due to the long CR cooling time scales compared to those of the thermal gas, an effect that diminishes the thermal gas pressure relative to that of CRs (Paper I).

It is very instructive to compare the CR proton to the CR electron pressure since protons and electrons are subject to different cooling mechanisms due to their large mass difference. The CR proton cooling timescale is generally larger than that of CR electrons such that protons accumulate within the ICM on a Hubble

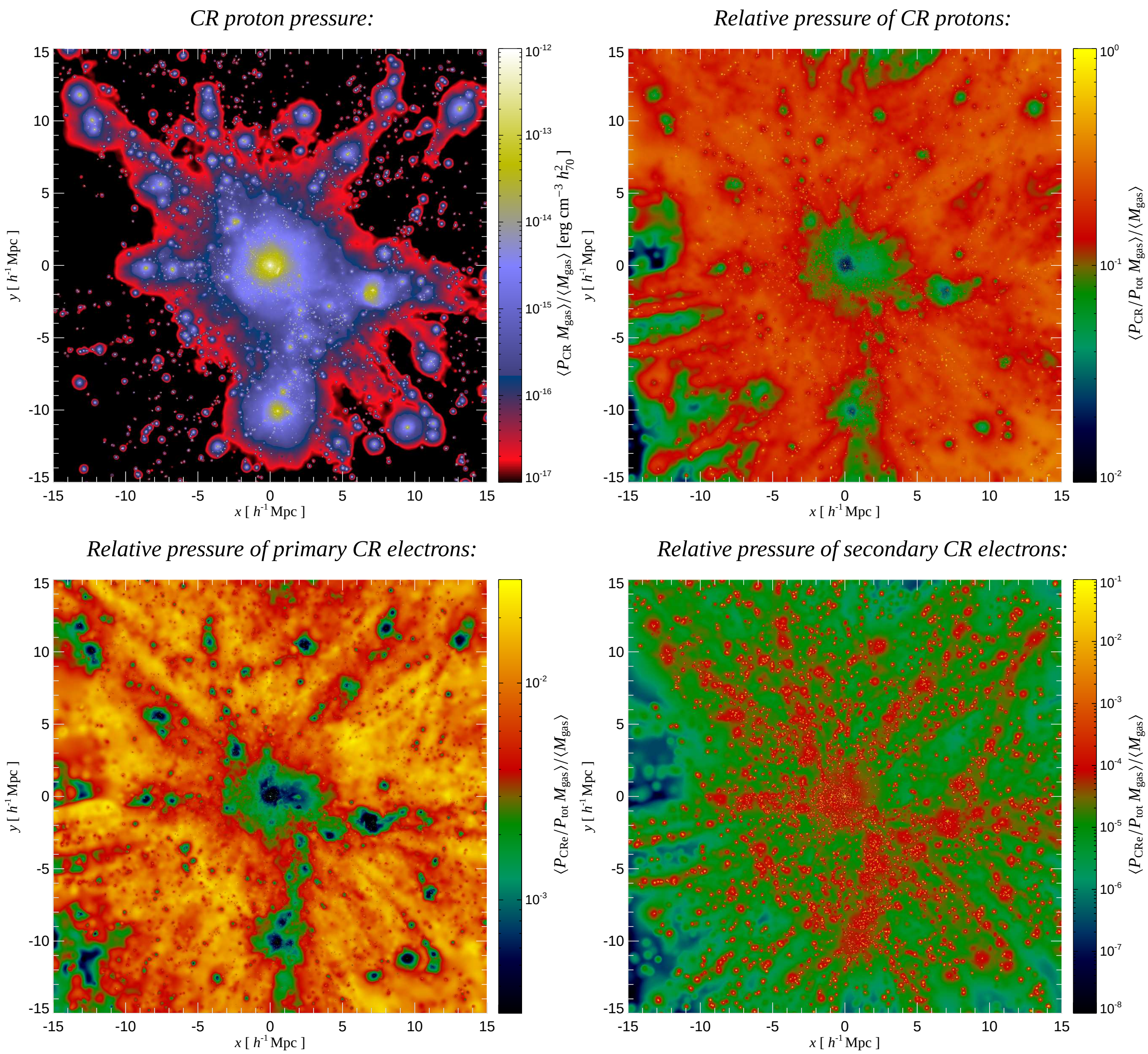

Figure 6. CR proton and electron pressure maps in the super-cluster environment of a large post-merging galaxy cluster ($M \simeq 10^{15} h^{-1}\,\mathrm{M}_\odot$) in our radiative simulation (model S2). The mass weighted CR pressure (top left side) is contrasted with the mass weighted CR pressure *relative* to the total gas pressure (top right side). Since the CR proton pressure decreases less steeply than the gas pressure as a function of cluster radius this results in an increasing relative CR pressure profile towards the periphery. In the bottom panels, we show the mass weighted CR electron pressure relative to the total pressure for primary, shock-accelerated electrons (left side) and secondary electrons resulting from hadronic CR proton interactions (right side). The CR electron pressure derives from the respective equilibrium distribution functions that balance acceleration and cooling processes.

timescale and maintain a comparatively smooth distribution over the cluster volume (top panels of Fig. 6). This implies that the CR proton pressure traces the time integrated non-equilibrium activities of a cluster and is only modulated by recent dynamical activities (see also Paper I, for average values of the relative CR energy in different dynamical cluster environments). In contrast, the pressure of primary CR electrons resembles the current dynamical, non-equilibrium activity of the forming structure and results in an inhomogeneous and aspherical spatial distribution. To underpin this argument, in the bottom panels of Fig. 6, we show the mass-weighted CR electron pressure relative to the total pressure $X_{\rm CRe} = P_{\rm CRe}/P_{\rm tot}$. On the left side, we show the relative pressure of primary, shock-accelerated electrons while the relative pressure of secondary electrons resulting from hadronic CR proton interactions is shown on the right side. The CR electron pressure derives from the respective equilibrium distribution functions that balance acceleration and cooling processes as laid out in Appendices A3.2 and A4.2. Note that the colour scale for the relative pressure of *primary CR electrons* spans exactly two orders of magnitude (like in the case of CR protons), peaking in the dilute WHIM at roughly 3 per cent rather than 30 per cent as in the case of CR protons. The relative CR electron pressure $X_{\rm CRe,prim}$ decreases towards clusters and groups due to larger Coulomb losses and smaller shock acceleration efficiencies within collapsed objects as in the case of CR protons. Interestingly, $X_{\rm CRe,prim}$ within galaxies is suppressed by roughly one order of magnitude with respect to the ambient intergalactic medium in which the galaxy resides due to large Coulomb losses. This is quite different from CR protons that acquire equipartition with the thermal gas inside galaxies. In general, the spatial variations of $X_{\rm CRe,prim}$ are larger than in the case of protons, showing that the CR electron pressure indeed reflects the active dynamical structure formation activities mediated by shock waves. In contrast, the mass weighted relative pressure of *secondary CR electrons* is shown on a colour scale that spans seven orders of magnitude, due to the high dynamic range of this quantity. The CR electron pressure is proportional to the number densities of CR protons and of the gas $P_{\rm CRe,sec} \propto n_{\rm CR} n_{\rm N}$, causing $X_{\rm CRe,sec}$ to peak towards densest structures and thus filling in the diminishing primary CR electron pressure inside dense structures such as galaxies. As a word of caution, we do not account for the re-acceleration of CR electrons e.g. via resonant pitch angle scattering by compressible magneto-hydrodynamical (MHD) modes neither do we account for a previously injected and aged electron population which could change the presented picture. Further work is required to elucidate these electron components in simulations.

3.2 Radio synchrotron emission

3.2.1 Projected radio maps

Figure 7 shows the large-scale "radio web"of the super-cluster region of our Coma-like cluster that experienced a recent merger. The radio emission is computed assuming a simple scaling model for the magnetic field of

$$\varepsilon_B = \varepsilon_{B,0} \left(\frac{\varepsilon_{\rm th}}{\varepsilon_{\rm th,0}}\right)^{2\alpha_B}, \qquad (5)$$

where the central magnetic energy density $\varepsilon_{B,0}$ and α_B are free parameters in our model, and $\varepsilon_{\rm th,0}$ denotes the thermal energy density at the cluster centre. It is motivated by turbulent dynamo theories of the growth of magnetic field strength that are typically saturating at a level proportional to the turbulent energy density or the thermal energy density (e.g., Subramanian 2003; Schekochihin & Cowley 2006). This allows us to explore the unknown behaviour of the large scale magnetic field parametrically (cf. Appendix B1 for more discussion). Our standard model (also adopted in Fig. 7) assumes a central magnetic field strength of $B_0 = 10\,\mu$G and $\alpha_B = 0.5$ which implies a constant ratio of thermal-to-magnetic pressure of 20 in our Coma-like cluster.

In the top panels of Fig. 7, we separately show the synchrotron emission of *primary CR electrons* that were accelerated directly at structure formation shocks as well as the radio emission of *secondary CR electrons* that results from hadronic CR proton interactions with ambient gas protons. The combined radio synchrotron emission (shown in the bottom left panel) shows that the morphologically smooth secondary component dominates the radio emission of the central cluster regions. In contrast, the irregularly shaped primary radio relic emission dominates in the cluster periphery and the super-cluster region that is believed to host the warm-hot intergalactic medium (WHIM). These observations are supported by the radio spectral index map between 150 MHz and 1.4 GHz (bottom right panel) which shows larger variations in the peripheral cluster regions. These are caused by projecting the radio emission from inhomogeneously accelerated primary CR electrons and reflect the strong variation of the Mach numbers of structure formation shocks at the outer cluster regions. Based on these findings, we put forward a new *unified scheme* for the generation of giant radio halos as well as radio mini-halos. The *giant radio halo* emission in merging clusters shows a transition from the secondary radio emission in the centre to the dominant primary emission component at the outer parts of radio halos. Gravitational energy, that is associated with the merger, is virialised by a morphologically complex network of strong shock waves in the cluster outskirts. This induces an irregular radio 'gischt' emission in the cluster periphery that represents radio synchrotron radiation emitted from shock-accelerated electrons. Our simulated radio emission maps of relaxed cool core clusters show a significantly reduced level of this primary emission component such that the diffuse radio emission in these systems is solely determined by the secondary radio emission, producing a *radio mini-halo*. Note that our simple magnetic model does not take into account the adiabatic compression of magnetic fields during the formation of a cool core. This effect should furthermore decrease the emission size of radio mini-halos making it comparable to the cool core region.

Closer inspection of the primary radio emission map (top left panel in Fig. 7) shows a bright *radio relic* on the lower right with respect to the cluster centre at a distance of $r \simeq 0.6 h^{-1}$ Mpc. This is caused by an outgoing merger shock wave that steepens as it reaches the shallower peripheral cluster potential. Further outwards at a distance of 2 and 3 h^{-1} Mpc to the cluster centre, there is a class of tangentially curved radio relics visible in orange and red. These are uniquely associated with strong shock waves as can be inferred by comparing the primary radio emission to the dissipated energy at shock waves (shown as brightness in the bottom left panel of Fig. 5). The statistical study of the radio emission at different frequencies and Faraday rotation of these objects will enable us to investigate non-equilibrium processes of virialisation including the acceleration of cosmic rays, the growth of magnetic fields, and kinetic energy in bulk motions that are expected to source turbulence in clusters. Comparing the emission level of the projected radio surface brightness maps to the LOFAR point source sensitivity of 0.25 mJy / (arcmin hour) at $\nu = 120$ MHz shows that moderately long exposures of super cluster regions have the potential to detect the large-scale "radio web" and to study the magnetic field on Mpc-scales that is woven into the web. Ongoing work that includes simulated mock observations for radio interferometers studies associated questions in greater detail (Battaglia et al. in prep.).

Figure 8 shows the dependence of the primary and secondary radio synchrotron emission on the observing frequency, the model for the magnetic field, as well as the type of simulated gas physics (radiative versus non-radiative). The top panels show the high- and low-frequency radio emission (1.4 GHz and 15 MHz) in our radiative simulation (model S2) using our standard model for the magnetic field. This demonstrates the potential of low-frequency radio arrays in studying non-thermal properties of the inter-galactic medium especially since the associated radio spectrum is steeper compared to that of the Galactic foreground emission. This will allow us to address questions such as the existence and properties of the WHIM and the existence and origin of large scale magnetic fields. The bottom left panel shows the total radio emission at 150 MHz in our non-radiative simulation (model S1) assuming our standard parameters for the magnetic field, and should be compared to the same panel in Fig. 7. The level of the primary radio emission in the cluster periphery and the super-cluster region is reduced in the non-radiative simulation (model S1) compared to the radiative case (model S2). Some relics in the bottom panel (model

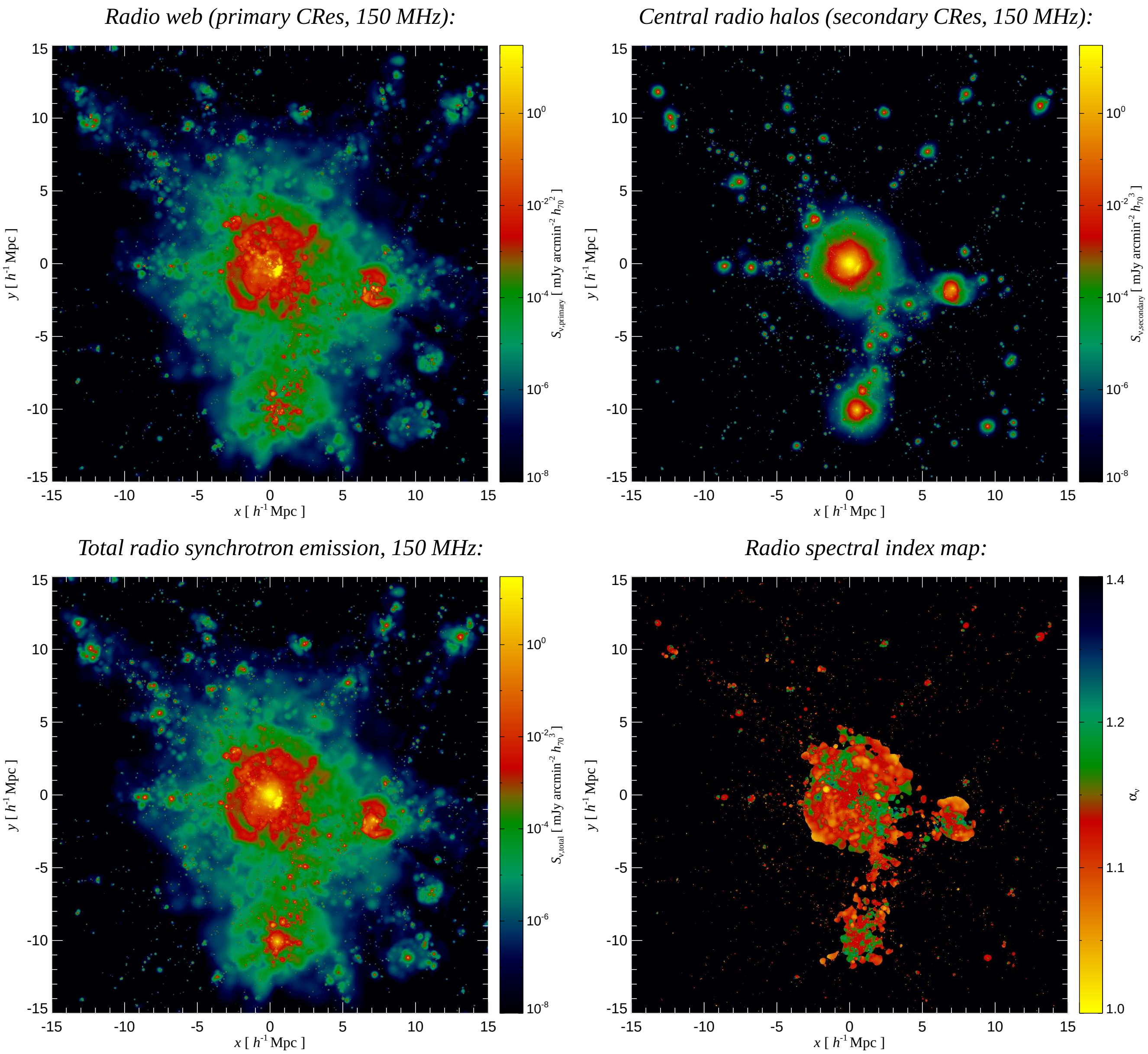

Figure 7. The large-scale "radio web" at 150 MHz of the super-cluster region of our Coma-like cluster that experienced a recent merger (g72a) in our radiative simulation (model S2). We show the synchrotron emission of *primary CR electrons* that were accelerated directly at structure formation shocks (top left side) as well as the radio emission of *secondary CR electrons* that results from hadronic CR proton interactions with ambient gas protons (top right side). The bottom left panel shows the *giant radio halo* emission of this cluster that is characterised in the centre by the regular smooth morphology of the secondary radio emission. At larger radii, we observe a transition to the the irregularly shaped primary radio "gischt" emission with a prominent radio relic to the lower right of the cluster. The radio spectral index between 150 MHz and 1.4 GHz (bottom right panel) shows larger variations in the peripheral cluster regions. These are caused by projecting the radio emission from inhomogeneously accelerated primary CR electrons and reflect the strong variation of the Mach numbers of structure formation shocks at the outer cluster regions.

S1) that are at distances of $\gtrsim 2\,h^{-1}$ Mpc to the cluster centre even show radio emission at the level that is comparable to that in the panel above (model S2) despite the lower frequency that should provide a flux level that is increased by an order of magnitude assuming $\alpha_\nu \simeq 1$. The reason for this stems from the larger shock strength (higher Mach numbers) of characteristic shocks that dissipate gravitational energy into thermal energy in radiative simulations (Paper I). The enhanced acceleration efficiency of CRs at stronger shocks leads to the increased primary radio emission in radiative simulations compared to the non-radiative case. The bottom right panel again shows the total radio emission at 150 MHz in our non-radiative simulation, however, with a shallower magnetic decline, $\alpha_B = 0.25$ which results in $\varepsilon_B \propto \varepsilon_{\rm th}^{0.5}$. Although the radial decline of this model for the magnetic field might be almost too shallow, it serves for illustrative purposes demonstrating that low-frequency radio arrays in combination with high-resolution simulations can tightly constrain the large scale behaviour of the magnetic field.

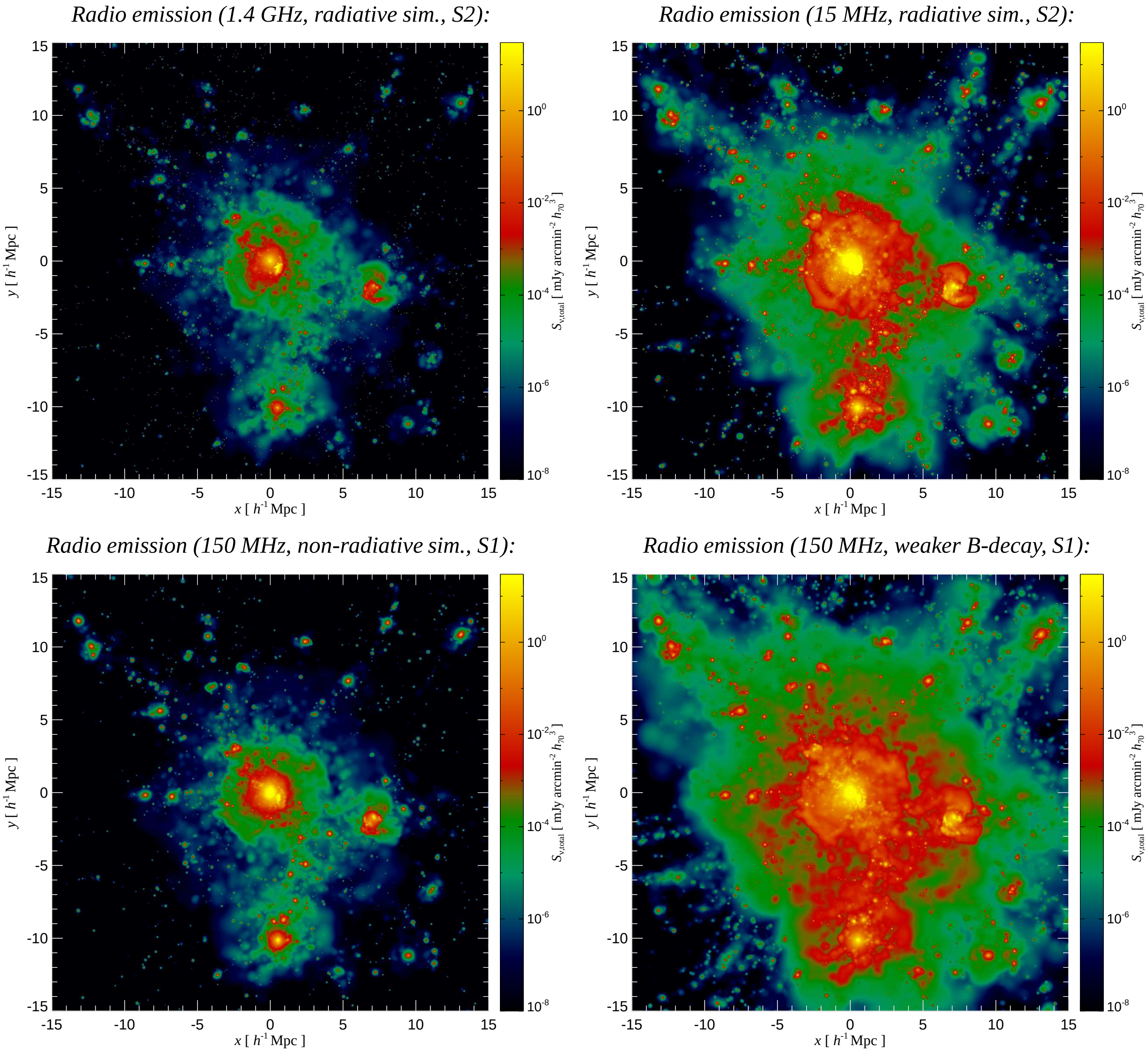

Figure 8. Dependence of the primary and secondary radio synchrotron emission on the observing frequency, the model for the magnetic field, as well as the type of simulated gas physics (radiative versus non-radiative). The top panels show the synchrotron radiation at 1.4 GHz and 15 MHz in our radiative simulation (S2) assuming a simple scaling of the magnetic energy density with the thermal energy density, $\varepsilon_B \propto \varepsilon_{\mathrm{th}}$. This demonstrates the potential of low-frequency radio arrays in studying non-thermal properties of the inter-galactic medium. The bottom left panel shows the total radio emission at 150 MHz in our non-radiative simulation (S1) with the same magnetic model. The bottom right panel again shows the total radio emission at 150 MHz in our non-radiative simulation, however, with a shallower magnetic decline, $\varepsilon_B \propto \varepsilon_{\mathrm{th}}^{0.5}$. For convenience, the colour scale is the same in all panels such that the emission at 15 MHz in the central cluster region is highly saturated.

3.2.2 *Radio emission profiles*

Radio synchrotron profiles allow us to confirm and quantify the proposed unified scheme for the cluster radio halo emission.

Primary versus secondary radio emission: The left side of Fig. 9 compares the synchrotron emission of *primary CR electrons* that were accelerated directly at structure formation shocks with that of *secondary CR electrons* that result from hadronic CR proton interactions with ambient gas protons. In cool core clusters, the azimuthally averaged secondary radio emission dominates the primary emission component for radii $r < 3R_{\mathrm{vir}}$. The smooth secondary component typically falls of at a radius $r \simeq 0.2R_{\mathrm{vir}}$ which resembles the characteristics of observed radio mini halos as observed e.g. in the Perseus cluster (Pedlar et al. 1990) or RX J1347.5-1145 (Gitti et al. 2007). Our model predicts diffuse secondary radio emission in virtually every cool core cluster.

Interestingly, our post-merging cluster g72a shows a transition from the secondary to the primary radio emission component towards the outer cluster regions triggered by the dynamical merger activity with strong shock waves traversing the cluster in order to thermalize the gas. These shock waves steepen as they break on

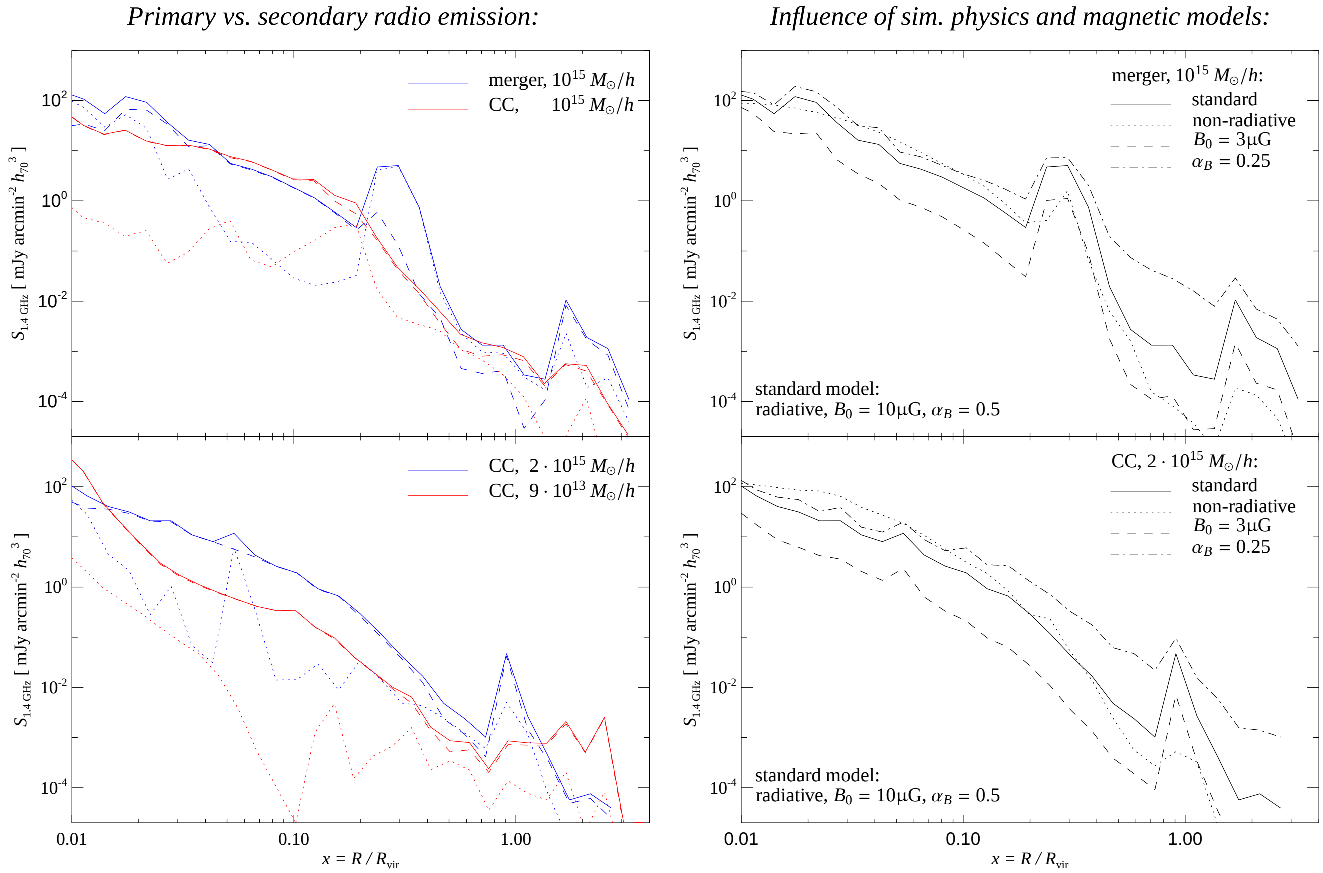

Figure 9. Azimuthally averaged radio synchrotron brightness profiles at $\nu = 1.4$ GHz. The left side compares the synchrotron emission of *primary CR electrons* that were accelerated directly at structure formation shocks (dotted lines) with that of *secondary CR electrons* that result from hadronic CR proton interactions with ambient gas protons (dashed line) while the solid line shows the sum of both emission components. The upper panel compares a post-merging cluster (g72a) with a cool core (CC) cluster (g51) of the same mass and the bottom panel compare the radio emission of two differently sized CC clusters (g8a versus g676). The right side shows the influence of different simulation and magnetic field models on the total synchrotron emission profiles for the post-merging cluster g72a (upper panel) and the CC cluster g8a (bottom panel). The standard model uses radiative gas physics (S2), has a central magnetic field strength of $B_0 = 10\ \mu$G, and scales as $\varepsilon_B \propto \varepsilon_{\mathrm{th}}^{2\alpha_B}$ with $\alpha_B = 0.5$. The other lines result from varying each of these assumptions separately leaving the others unchanged. The radio emission in our non-radiative simulation (S1, dotted lines) declines faster. The emission profiles for a lower central magnetic field strength (dashed lines) and with a weaker magnetic decline (dash-dotted lines) illustrate the uncertainty in the simulated radio profiles.

the shallower peripheral cluster potential. The associated increase in the primary radio emission comes hand in hand with a stronger variation of the radio spectral index towards the cluster periphery (cf. Fig. 7). In the particular case of g72a, the resulting radio halo profile reaches out to $r \simeq 0.45 R_{\mathrm{vir}}$ which corresponds to the observed size of $R_{\mathrm{max}} \simeq 1\ \mathrm{Mpc}/h_{70}$ of the Coma radio halo at $\nu = 1.4$ GHz (Deiss et al. 1997; Reiprich & Böhringer 2002). We verified that the transition from the secondary to the primary radio emission in our simulated giant radio halos is independent on the chosen projection and a generic prediction for merging clusters. Our simple scaling model for the magnetic field of Eqn. (5) does clearly not include non-equilibrium effects related to the growth of the magnetic field. The enhancement of the magnetic field strength through turbulent dynamo processes will saturate on a level which is determined by the strength of the magnetic back-reaction (e.g., Subramanian 2003) and is typically a fraction of the turbulent energy density. Thus, in a real cluster, the strong shocks at the cluster periphery are expected to drive turbulence and strong shear motions which should in turn lead to a stronger magnetic field amplification. Our adopted scaling of the magnetic field with the thermal energy density might partially neglect these effects and should somewhat underestimate the peripheral radio synchrotron emission.

Influence of magnetic parametrisation on radio emission: The right side of Fig. 9 shows the influence of different simulations and magnetic field models on the total synchrotron emission profiles for our massive post-merging cluster and cool core cluster. The emission profiles for lower central magnetic field strength (dashed lines, $B_0 = 3\ \mu$G) shows a small decrease of the central radio emission by a factor of two while it is considerably suppressed by an order of magnitude towards larger radii. This is due to the two distinctive regimes of a synchrotron emitting equilibrium distribution of CR electrons (cf. Fig. 3). For field strengths $B > 3\ \mu$G, the synchrotron flux is almost insensitive to the field strength while it scales as $j_\nu \propto B^{\alpha\nu+1}$ for weaker fields $B < 3\ \mu$G which are present at larger cluster radii. The emission profile for a weaker magnetic decline (dash-dotted lines, $\alpha_B = 0.25$) is more extended than our standard model, as expected. Current cosmological MHD SPH simulations (e.g., Dolag et al. 2001) may not sufficiently resolve small scale turbulent dynamo processes and large shear motions that are thought to amplify the magnetic field in the coarsely sampled supercluster regions beyond the accretion shocks. The model with the

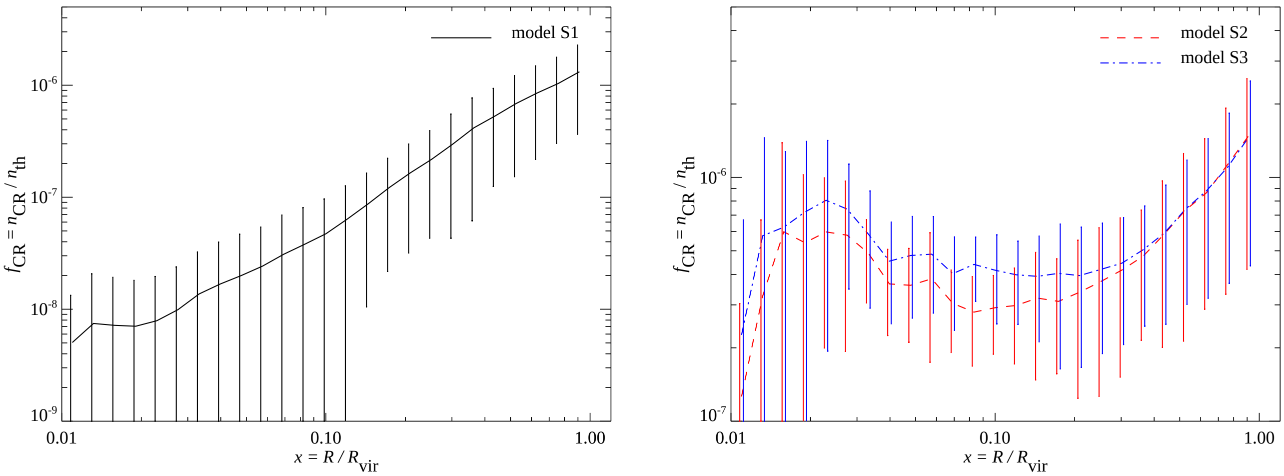

Figure 10. Average profiles for the spherically averaged CR fraction $f_{CR} = n_{CR}/n_{th}$ of our sample of all 14 clusters at redshift $z = 0$. The error bars represent the standard deviation from the sample mean. The increase of f_{CR} with radius is independent of the modelled CR physics (S1 – solid, S2 – dashed, S3 – dash-dotted) and continues beyond the virial radius suggesting that this is a generic property of CR physics. The increase of f_{CR} in our radiative models for small radii $r < 0.1R_{vir}$ is due to the short cooling timescale of the gas compared to that of CR protons (cf. Paper I). Note the different axes scales in both panels.

weaker magnetic decline is an attempt to parametrise those uncertainties. Note that despite the uncertainties in the parametrisation of the magnetic field and thus the overall radio emission, the conclusions with respect to the different emission components (primary versus secondary) and their emission characteristics remain unchanged.

Influence of simulated physics on radio emission: The radio emission in our non-radiative simulations (S1, dotted lines) is much smoother and declines faster since there is only a very weak transition to the primary component due to the weaker shocks in the cluster periphery compared to the radiative simulations (S2). It is surprising that the central radio emission in simulation models S1 and S2 almost coincide despite the large difference of the central CR fraction $f_{CR} = n_{CR}/n_{th}$ in both models (cf. Fig. 10). At $r = 0.02R_{vir}$ the CR fraction is two orders of magnitude larger in our radiative simulations compared to our non-radiative simulations. This can be understood by the self-regulated nature of CR feedback. The secondary synchrotron emission scales as $j_\nu \propto n_{CR} n_{gas} \propto f_{CR} n_{gas}^2$ neglecting the weak additional density dependence through the magnetic field in the synchrotron regime (cf. Fig. 3). The lower gas density in the radiative simulations (cf. Figs. 3 and 5 in Paper I) almost exactly balances this difference of the CR fraction such that the resulting secondary synchrotron emission level in the centre remains only slightly modified. This is due to a combination of the following reasons. (1) The CR cooling timescales due to Coulomb and hadronic interactions of CRs, $\tau_{pp,Coul} \propto n_{gas}^{-1}$, is almost an order of magnitude larger in our non-radiative simulations compared to our radiative case owing to the central density difference. (2) A second sub-dominant effect is the reduced depletion of the CR pressure in our radiative simulations due to adiabatic compression of our composite of CRs and thermal gas which disfavours the CR pressure relative to the thermal pressure.

Part of this density difference is reinforced in contemporary cosmological radiative simulations that do not include feedback from AGN. This leads to the well-known over-cooling problem which results in an overproduction of the amount of stars, enhanced central gas densities, and too small central temperatures compared to X-ray observations. The density enhancement at the very centre and the associated star formation take place at the expense of the surrounding ICM which ends up being less dense compared to its initial stage before cooling set in. This hypothetical initial stage is realised by our non-radiative simulations that does not take into account radiative cooling. We show that the secondary CR emission (radio synchrotron, inverse Compton, and pion decay induced γ-ray emission) within the framework of our CR model is almost independent of those short-comings in the central cluster regions. The difference of the radio emission at larger radii between our models S1 and S2 however is a robust finding and primarily caused by the difference of the primary radio emission. This difference is due to the on average stronger shock waves that lead to more efficient CR electron acceleration in our radiative simulations.

3.2.3 Discussion of synchrotron polarisation

Synchrotron emission from primary accelerated electrons is polarised due to a combination of two effects. (1) Shock compression aligns unordered magnetic fields with the shock plane (Ensslin et al. 1998). Furthermore, shearing motions induced by oblique shocks stretch these field lines which leads to a larger magnetic coherence length of two-dimensional field configurations (Schekochihin & Cowley 2006). If the synchrotron emitting structure that is energised by the formation shock wave is seen at some angle between the line-of-sight and the normal of the shock front, the magnetic field structure projected onto the plane of sky shows a preferential direction which implies a preferred intrinsic synchrotron polarisation. (2) The combination of the localised acceleration site of CR electrons at these shock fronts and the short synchrotron cooling times (cf. Fig. A1) leads to a small synchrotron emission volume. Thus, these peripheral radio relics are expected to show a preferred synchrotron polarisation with the magnetic field aligned with the shock surface (as observed e.g. in Abell 3667 by Röttgering et al. 1997). Superposing many causally unconnected radio relics in projection leads to a decrease of the degree of polarisation.

Hadronically induced synchrotron emission of the smooth radio halo is virtually unpolarised assuming statistically isotropic distribution of magnetic field vectors without a preferred direction.

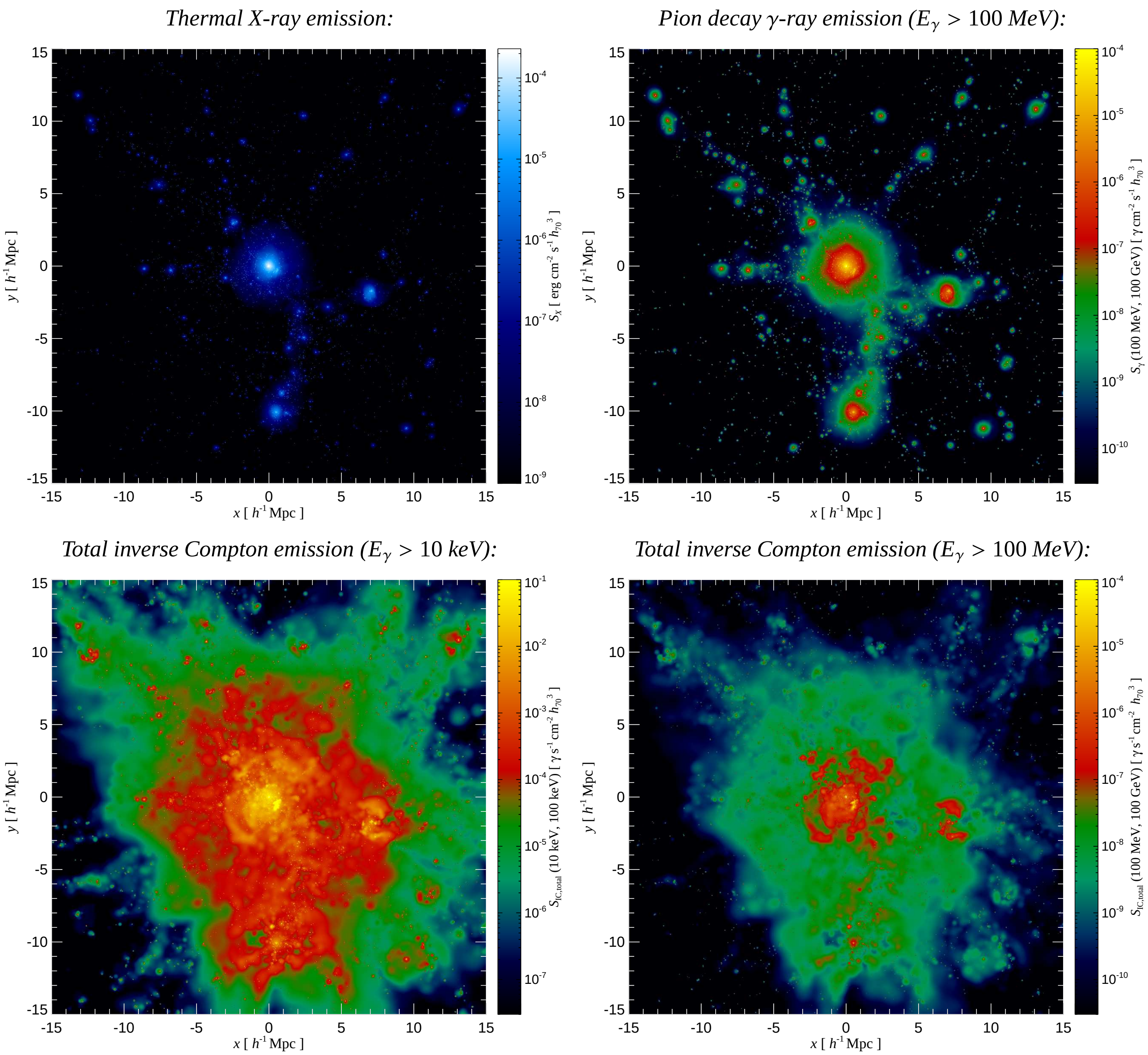

Figure 11. The top panels compare the thermal X-ray emission and the γ-ray emission resulting from hadronic CR interaction with ambient gas protons of the super-cluster region of our Coma-like cluster in our radiative simulation (model S2, cluster g72a). The hadronic γ-ray emission shows a shallow decline with radius due to the rising CR-to-thermal number density profile. The bottom panels show the inverse Compton emission from primary and secondary CR electrons in the hard X-ray (left side) as well as the γ-ray band (right side). The primary CR electrons dominate the emission signal on large scales. Comparing the γ-ray emission components (right panels) shows that the pion decay γ-rays exceed the total IC emission at energies $E_\gamma > 100$ MeV.

The large emission volume is filled with magnetised plasma that causes the plane of polarisation to Faraday rotate. Hadronically generated CR electrons fill the same cluster volume. Thus, each radio emitting volume element along the line-of-sight, that is separated by more than the magnetic correlation length or the Faraday depth, if shorter, radiates causally unconnected intrinsically polarised emission that averages out to a net unpolarised emission, e.g. radio halos are Faraday depolarised.

Combining these considerations with the previously developed model for the radio halo emission implies a transition from the virtually unpolarised radio halo emission at small impact parameters to a small degree of polarisation at the halo periphery, characterised by the dominating primary emission there. In order to detect this polarisation one might be forced to go out to large impact parameters with a small resulting synchrotron surface brightness where the emission is dominated by very few relics along the line-of-sight. Owing to the different injection timescales of primary and secondary CR electrons, we conclude that the secondary halo emission traces the time integrated non-equilibrium activities of a cluster and is modulated by the recent dynamical activities (Paper I). In contrast, the polarised radio relic emission resembles the current dynamical, non-equilibrium activity of a forming structure and results in an inhomogeneous and aspherical spatial distribution.

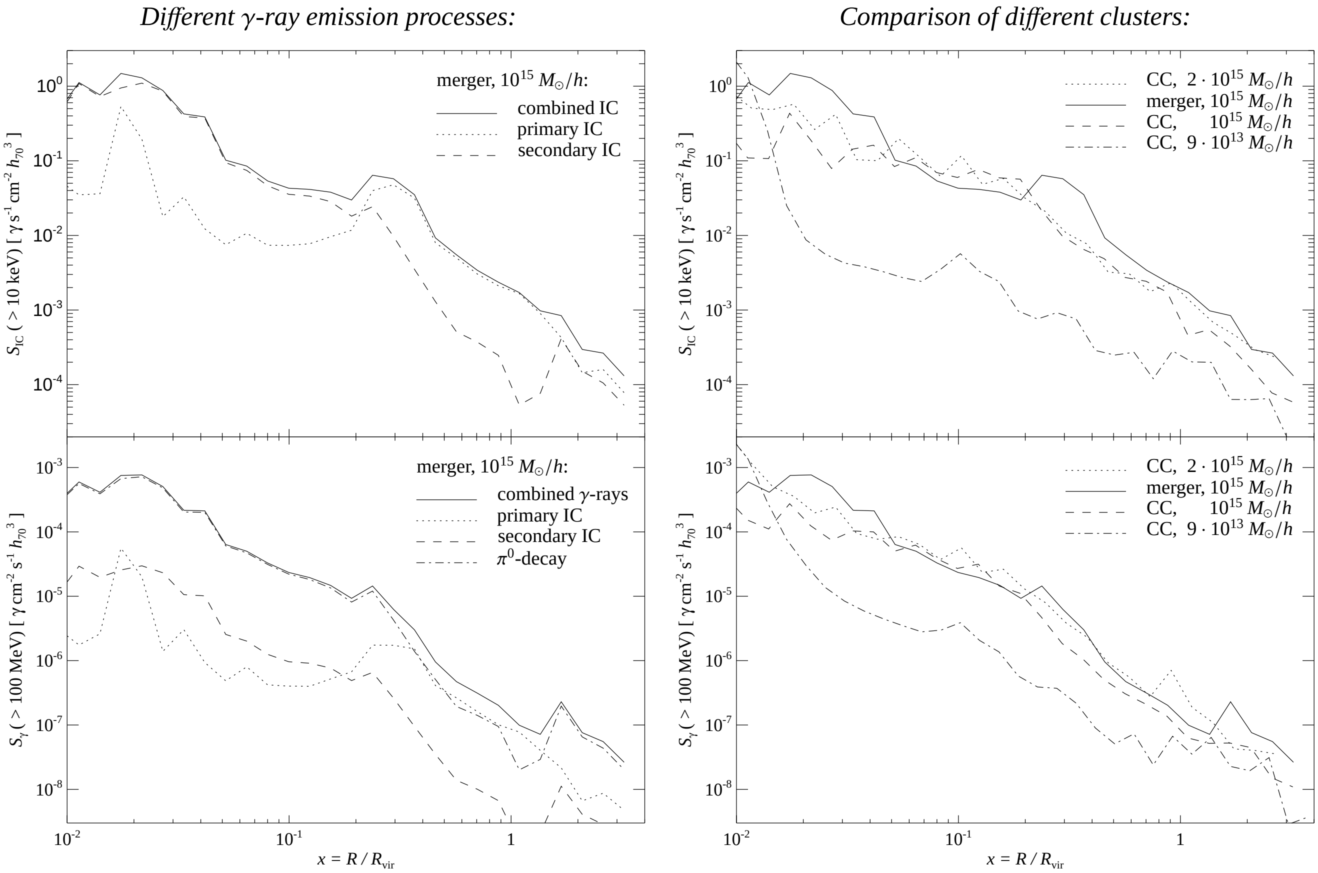

Figure 12. Azimuthally averaged profiles of the inverse Compton (IC) surface brightness for energies $E_\gamma > 10$ keV (upper panels) and γ-ray emission profiles for $E_\gamma > 100$ MeV (bottom panels). Using the simulation of the post-merging cluster g72a, the left side compares the IC emission of *primary CR electrons* that were accelerated directly at structure formation shocks (dotted lines) with that of *secondary CR electrons* that result from hadronic CR proton interactions with ambient gas protons (dashed lines) while the solid lines shows the sum of both emission components. The dominant emission component at energies $E_\gamma > 100$ MeV is the pion decay induced γ-ray emission (dash-dotted lines). The right side compares the total hard X-ray and γ-ray emission, respectively, for for the different clusters g8a (dotted lines), g72a (solid lines), g51 (dashed lines), and g676 (dashed-dotted lines). While the hard X-ray/γ-ray emission clearly scales with the cluster mass, the dynamical state of the cluster is equally important and can even reverse the mass trend as can be inferred from the IC emission for $E_\gamma > 10$ keV comparing the top two clusters in the figure legend.

3.3 Hard X-ray and γ-ray emission

3.3.1 *Projected X-ray and γ-ray maps*

Different non-thermal γ-ray emission processes are compared to the thermal X-ray emission in Fig. 11. The top panels compare the morphology of the thermal X-ray surface brightness (for details of the projection, cf. Paper I) to that of the γ-ray emission resulting from hadronic CR interactions with ambient gas protons of our Coma cluster region in our radiative simulation. Although they resemble each other, the pion decay induced γ-ray emission declines slower with radius and makes the γ-ray halo more extended. The bremsstrahlung emission of the thermal gas scales as $n_{\rm th}^2$ (neglecting the radial dependence of the cooling function) while the hadronically induced γ-ray emission scales as $n_{\rm gas} n_{\rm CR}$. The discrepancy between the radial behaviour of the thermal and non-thermal emission can be understood by looking at the right side of Fig. 10 which shows average profiles of the spherically averaged CR fraction $f_{\rm CR} = n_{\rm CR}/n_{\rm th}$ of our sample of all clusters. There is an increase of $f_{\rm CR}$ with radius that is independent of the modelled CR physics and continues beyond the virial radius. This generic prediction of CR physics is due to the more efficient CR acceleration at the peripheral strong accretion shocks compared to weak central flow shocks.

The bottom panels of Fig. 11 show the inverse Compton emission from primary and secondary CR electrons in the hard X-ray (left side) as well as the γ-ray band (right side). The primary CR electrons dominate the hard X-ray emission signal on large scales. The primary IC emission directly reflects the inhomogeneous virialisation process that manifests itself through a filigree web spun by shocks (cf. Fig. 5). In principle, IC emission is the cleanest way of probing structure formation shock waves since the inverse Compton emission is not weighted by the magnetic energy density as it is the case for synchrotron emission. Visually comparing the right panels of Fig. 11 implies that the pion decay induced γ-ray emission dominates the total IC emission in the energy range that is of interest to GLAST.

3.3.2 *Hard X-ray IC and γ-ray emission profiles*

Figure 12 shows azimuthally averaged profiles of the IC surface brightness for energies $E_\gamma > 10$ keV (upper panels) and γ-ray emission profiles for $E_\gamma > 100$ MeV (bottom panels). Using the simulation of the post-merging cluster g72a, the left side compares the IC emission of *primary CR electrons* that were accelerated directly at structure formation shocks with that of *secondary CR electrons* that result from hadronic CR proton interactions with ambient gas protons. The primary and especially the secondary IC emission is generally more inhomogeneous compared to both radio emission components. Secondly, the IC emission declines less steeply with radius and shows almost a power-law profile compared with the β-profile in the case of synchrotron emission. Both effects are due to the weighting by the magnetic field which in the latter case tends to smooth out the inhomogeneous CR electron distribution and causes a steeper decrease of the radio synchrotron emission (at least in our model of the magnetic field).

At energies $E_\gamma > 100$ MeV, the pion decay induced γ-ray emission is the dominant emission component everywhere except in the peripheral regions of the post-merging cluster g72a where the primary IC emission is of similar strength (cf. bottom left panel of Fig. 12). As a word of caution it should be added, that our simulation assumes a CR proton spectral index of $\alpha_\mathrm{p} = 2.3$. Lowering this value would result in a larger secondary IC component (cf. Fig. 4). Future work is required to study such a scenario which might find applications in the outer parts of clusters. However, the pion decay component at $E_\gamma > 100$ MeV should be robust with respect to variations of α_p since it samples the pion bump that is sensitive to threshold effects of the hadronic cross-section but not to the spectrum of the parent CR distribution. Despite the fact that the secondary IC emission still dominates the primary IC emission at $E_\gamma > 100$ MeV, the primary IC component is increased by a factor of two compared to the hard X-ray emission at $E_\gamma > 10$ keV. We conclude that the mean IC spectral index is obviously smaller than that of the secondary emission, $\alpha_\nu = 1.15$. This can be understood by combining the facts that a superposition of different power-law spectra produces a concave spectrum and that IC emission at $E_\gamma > 100$ MeV results from CR electrons with a Lorentz factor $\gamma \gtrsim 3 \times 10^5$ according to Eqn. (2). This again stresses the importance of correctly modelling the peripheral regions of a cluster since they show predominantly the conditions for strong shock waves that are able to accelerate such flat CR electron populations.

We move on to compare the hard X-ray and γ-ray emission for clusters of different masses and dynamical states. While the hard X-ray/γ-ray emission clearly scales with the cluster mass, the dynamical state of the cluster is equally important and can even reverse the mass trend (cf. the right side of Fig. 12). The reason for this lies in the enhanced CR pressure in merging clusters (Paper I) as well as in the primary IC emission that sensitively traces current non-equilibrium or merging activities of clusters.

Figures 14 and 13 study the influence of different simulated physics on γ-ray emission at $E_\gamma > 100$ MeV. The γ-ray emission is more inhomogeneous in radiative simulations compared to non-radiative simulations. This is due to the CR pressure equipartition within each galaxy. The overall γ-ray luminosity, however, is very similar as can be inferred from the azimuthally averaged emission profiles. This confirms our finding for the synchrotron emission in Fig. 9 and confirms our explanation that this is indeed a self-regulated effect of CR feedback and not biased due to the magnetic weighting of the synchrotron emission. The complete CR model that also accounts for CR from SNe (dashed lines, model S3) shows a slightly enhanced γ-ray emission level since we opened up a new acceleration channel compared to our standard model S2.

Influence of simulated physics on γ-ray emission:

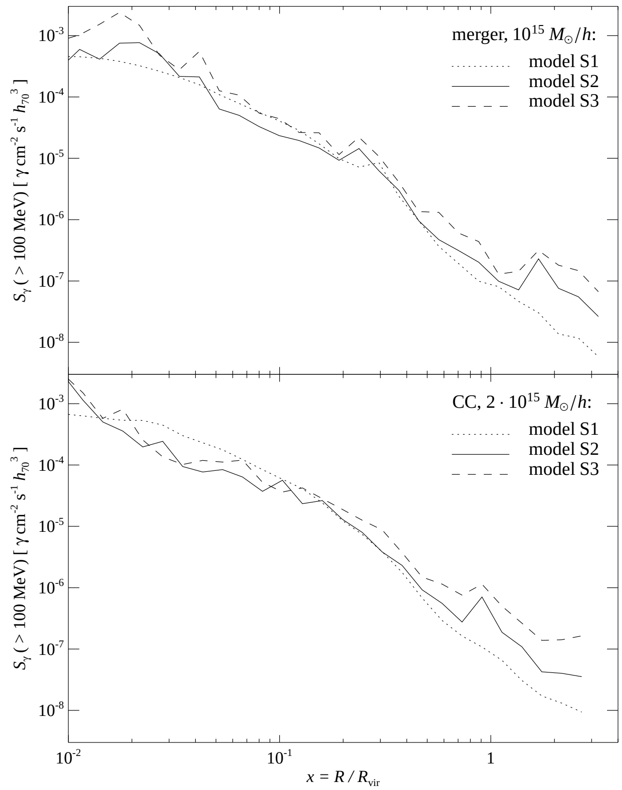

Figure 13. Influence of simulated physics on azimuthally averaged γ-ray emission profiles for $E_\gamma > 100$ MeV. The top panel shows the emission profile of the post-merging cluster g72a while the bottom panel that of the large cool core cluster g8a. Shown are our non-radiative simulations (dotted lines, model S1), our radiative simulations with CR protons injected at structure formation shocks (solid lines, model S2), and the complete CR model where we additionally take CR acceleration at SNe shocks into account (dashed lines, model S3). Despite the different physics in these simulations, the γ-ray emission level is similar.

3.4 Correlations between thermal and non-thermal emission

Compressing intrinsically non-spherical emission purely into surface brightness profiles causes loss of information and might yield biased results. In addition to emission maps and surface brightness profiles, we complete our analysis using pixel-to-pixel correlations of the thermal X-ray surface brightness with non-thermal cluster emission processes. To this end we compare these correlations of our post-merging cluster simulation g72 (Fig. 15) to the cool core cluster simulation g8 (Fig. 16). Each of these figures shows the correlation space density of the radio surface brightness (top panels) and the γ-ray surface brightness for $E_\gamma > 100$ MeV (bottom panels), as well as that of the hadronically induced non-thermal emission (left side, red colour scale) and the non-thermal emission of *primary CR electrons* that were accelerated directly at structure formation shocks (right side, blue colour scale).

While the hadronically induced non-thermal emission is tightly correlated with the thermal bremsstrahlung emission, the correlation is much weaker and the scatter is increased in the case of primary non-thermal emission where structures in the correlation space density correspond to individual structure formation shock waves. We can see preferably tangential shocks that are characterised by a varying non-thermal emission for a constant X-ray sur-

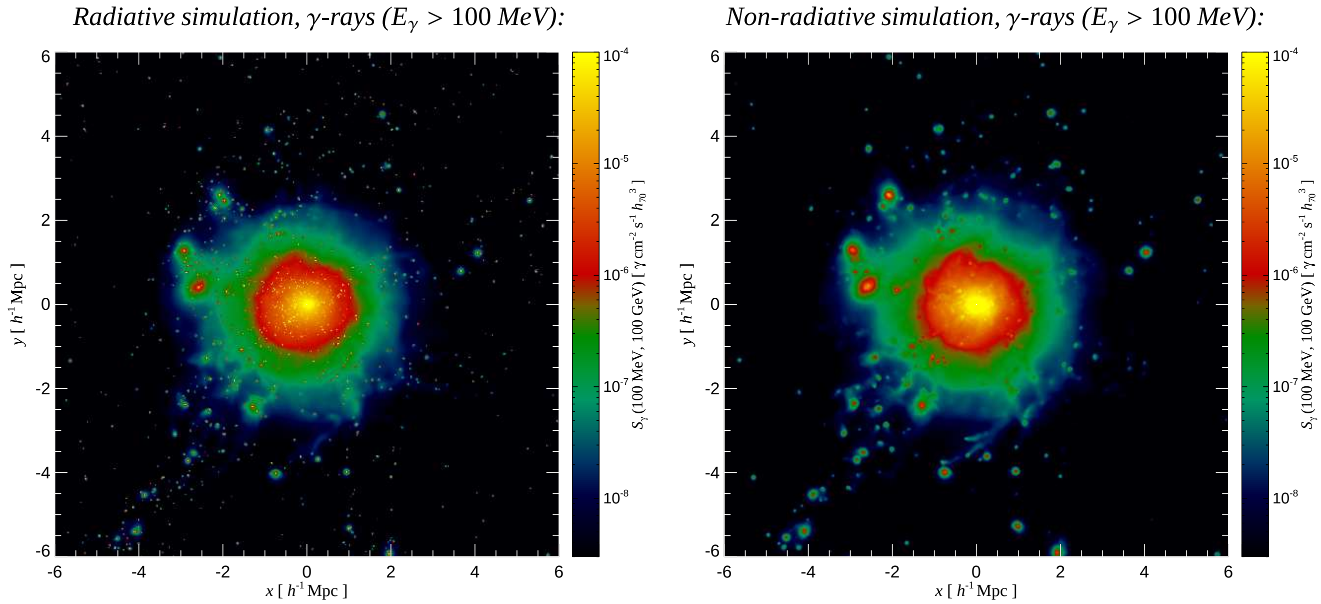

Figure 14. Influence of simulated physics on pion decay γ-ray emission maps for $E_\gamma > 100$ MeV of the large cool core cluster g8a. The peaked emission of each galaxy in the radiative simulation (left panel, model S2) contrasts the smoother and fluffier γ-ray emission of our non-radiative simulation with CR protons injected at structure formation shocks (right side, model S1).

face brightness and to a smaller extend radial shocks where the role of thermal and non-thermal emission is interchanged.

3.4.1 *Correlations of the synchrotron emission*

Closer inspection of the *secondary synchrotron emission* (top left panel in Fig. 15) shows flattening of the correlation

$$S_\nu = S_{\nu,0} \left(\frac{S_X}{S_{X,0}} \right)^a, \tag{6}$$

where the power-law index changes from $a = 1.7$ to $a = 1.3$ above $S_{X,0} = 3 \times 10^{-6}$ erg cm^{-2} s^{-1} h_{70}^3, with a normalisation $S_{\nu,0} = 0.057$ mJy arcmin^{-2} h_{70}^3. This is due to a combination of the following two effects. (1) Towards higher X-ray surface brightness, the radio emission experiences a transition from IC to synchrotron regime with a weaker dependence on magnetic field that goes along with weaker density dependence. (2) The merger displaces the central cool core and disturbs the ICM by means of merging shock waves that dissipate the gravitational binding energy associated with the merger. This yields an increased CR proton pressure and number density relative to the thermal gas within the central X-ray luminous regions and causes the change in the correlation. Since the thermal energy distribution is equally effected by these re-distribution of energy, this merger induced effect can be furthermore amplified by the transition from the IC to synchrotron regime as explained above. The change of the power-law index of the correlation is more pronounced for our post-merging cluster simulation g72 compared to our cool core cluster g8 suggesting the importance of the second effect. Note that the explicit values of the correlation, in particular $S_{\nu,0}$, depend on the assumed model for the magnetic field. There is a second branch in the correlation of the hadronically induced non-thermal emission visible that is due to the other smaller cluster forming in that simulation.

The correlation of the *primary synchrotron emission* (top right side) shows a large scatter especially at large surface brightness such that the correlation of the *total synchrotron brightness* is expected to broaden and to become flatter towards lower surface brightness to yield a roughly linear correlation. The exact realisation of the correlation at a surface brightness that is substantially supported by primary synchrotron emission sensitively depends on the mass ratio, geometry, and the advanced state of the merger. Thus our simulations can only provide quantitative predictions for the statistical behaviour rather than deterministic predictions for the correlations. Our correlations are strikingly similar to the ones found in observed radio halos (cf. Govoni et al. 2001). They find a linear relation between the radio and X-ray surface brightness that is tight at high surface brightness while it broadens and flattens towards dimmer brightness. This behaviour is one of the strongest arguments in favour of our new model for radio halos that should be dominated in the centre by secondary emission with a transition to the primary synchrotron emission in the cluster periphery. In accordance with our findings, their radio halo emission is slightly more extended compared to the thermal X-ray emission. Varying spectral index distributions preferably in the cluster periphery (Feretti et al. 2004) support this picture. In particular, our model supports a strong link between radio halos and cluster mergers for which there is a strong evidence in the literature (Feretti et al. 2004, and references therein).

3.4.2 *Correlations of the γ-ray emission*

The bottom left panels in Figs. 15 and 16 include pion decay γ-ray emission as well as IC emission from secondary CR electrons. These tight correlations are characterised by a sub-linear power-law relation. This is due to the shallower decay of the CR number density $n_{\rm CR}$ compared to that of the thermal gas leading to an increase of the CR fraction $n_{\rm CR}/n_{\rm th}$ (cf. Fig. 10). Our post-merging cluster g72a shows a small variation of the power-law index of the γ-ray to X-ray correlation at high surface brightness albeit not as pronounced as in the case of radio synchrotron emission. This con-

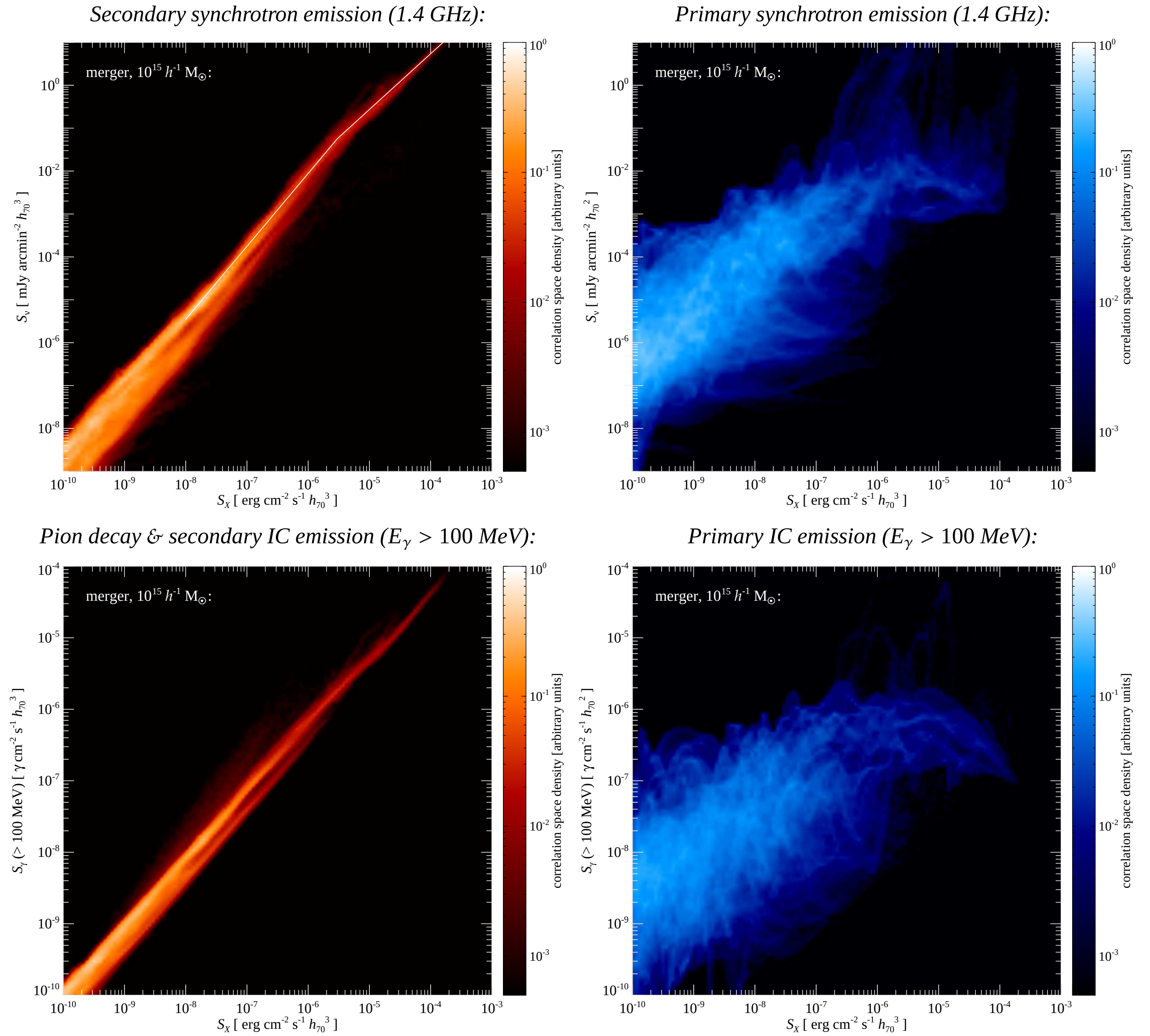

Figure 15. Pixel-to-pixel correlation of the thermal X-ray surface brightness with both the radio surface brightness (top panels) and the γ-ray surface brightness for $E_\gamma > 100$ MeV (bottom panels) for our post-merging cluster simulation g72 using our model S2. Shown is the correlation space density of the hadronically induced non-thermal emission (left side, red colour scale) and the non-thermal emission of *primary CR electrons* that were accelerated directly at structure formation shocks (right side, blue colour scale). The bottom left panel includes pion decay γ-ray emission as well as IC emission from secondary CR electrons. While the hadronically induced non-thermal emission is tightly correlated with the thermal bremsstrahlung emission, the correlation is much weaker and the scatter is increased in the case of primary non-thermal emission where the structures in the correlation space density correspond to individual structure formation shock waves. The line in the top left panel is a fit to the correlation where the slope flattens from 1.7 to 1.3 towards high luminosities.

firms that both the merger induced boost of the CR pressure and the transition from IC to synchrotron regime is responsible for the flattening of the correlation between radio and X-ray surface brightness. The primary IC emission of the cool core cluster simulation g8a (lower right panel of Fig. 16) shows a complete absence of any correlation. The influence of the merger activity of a cluster on enhancing the non-thermal cluster emission can thus unchallengeably be studied with the primary IC γ-ray emission (lower right panel of Fig. 15). Comparing this primary IC γ-ray emission to its counterpart radio emission indicates that a large part of that correlation with the X-ray emission is indeed owed to the merger induced CR enhancement and only in parts by the density dependence of the magnetic field.

4 DISCUSSION AND FUTURE WORK

4.1 Comparison to previous literature

There have been a series of pioneering papers simulating the non-thermal emission from clusters by numerically modelling discre-

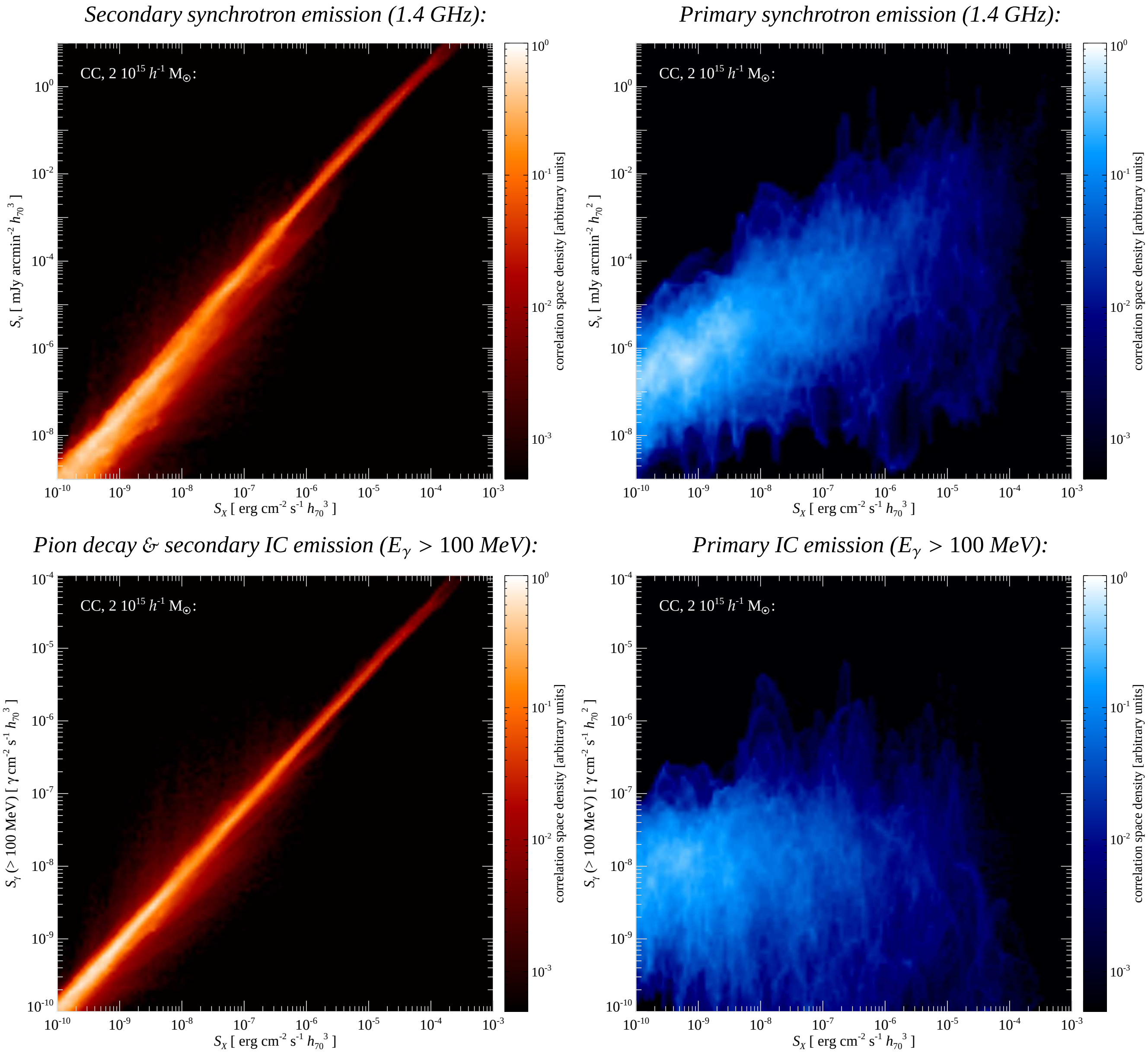

Figure 16. Same as Fig. 15 but for our cool core cluster simulation g8. Note the absence of any correlation in the bottom right panel showing the primary IC surface brightness for $E_\gamma > 100$ MeV which suggests that the correlation of the primary radio emission (top right panel) is solely due to our assumed model of the magnetic field, $\varepsilon_B \propto \varepsilon_{\rm th}$.

tised CR energy spectra on top of Eulerian grid-based cosmological simulations (Miniati 2001; Miniati et al. 2001a,b; Miniati 2002, 2003). In contrast to our approach, these models neglected the hydrodynamic pressure of the CR component, were quite limited in their adaptive resolution capability, and they neglected dissipative gas physics including radiative cooling, star formation, and supernova feedback. Comparing the non-thermal emission characteristics of primary CR electrons, hadronically generated secondary CR electrons, and pion decay γ-rays, we confirm the general picture put forward by these authors while we find important differences on smaller scales especially in cluster cores. Our inhomogeneous, peripheral radio relic emission resembles their findings. However, the hadronic component of our simulated radio halos is more centrally concentrated (cf. Miniati et al. 2001b). Our simulations both agree that the predicted level of hard X-ray inverse Compton emission falls short of the claimed detection in Coma and Perseus albeit the discrepancy is more dramatic in our simulations. We confirm that the high-energy γ-ray emission ($E_\gamma > 100$ MeV) from cluster cores is dominated by pion decays while at lower energies, the IC emission of secondary CR electrons takes over (Miniati 2003) – at least for non-merging clusters. We reproduce their finding that the γ-ray emission in the virial regions of clusters and beyond in super-cluster regions stems from IC emission of primary shock accelerated electrons. Contrarily to these authors, we find that the surface brightness of this emission component remains sub-dominant in projection compared to the hadronically induced emission components in the cluster core and that the pion decay completely dominates the high-energy γ-ray emission of clusters. We note that our

γ-ray fluxes from clusters are typically a factor of two smaller than the estimates given in Miniati et al. (2001a). As worked out in Paper III, this has important implications for the number of detectable γ-ray clusters by GLAST.

All the discrepancies can be understood by two main effects that lead to an overestimation of the CR pressure inside the clusters simulated by Miniati et al. (2001a) and thus overproduced the resulting non-thermal emission: (1) Miniati et al. (2000) identified shocks with Mach numbers in the range $4 \lesssim \mathcal{M} \lesssim 5$ as the most important in thermalizing the plasma. In contrast, Ryu et al. (2003) and Pfrommer et al. (2006) found that the Mach number distribution peaks in the range $1 \lesssim \mathcal{M} \lesssim 3$. Since diffusive shock acceleration of CRs depends sensitively on the Mach number, this implies a more efficient CR injection in the simulations by Miniati et al. (2001a). (2) The grid-based cosmological simulations have been performed in a cosmological box of side-length $50\,h^{-1}$ Mpc with a spatial resolution of $200\,h^{-1}$ kpc, assuming an Einstein-de Sitter cosmological model (Miniati et al. 2001a). The lack of resolution in the observationally accessible, dense central regions of clusters in the grid-based approach underestimates CR cooling processes such as Coulomb and hadronic losses. Secondly, these simulations are unable to resolve the adiabatic compression of a composite of CRs and thermal gas, an effect that disfavours the CR pressure relative to the thermal pressure. To summarise, their modest resolution in non-radiative simulations anticipates some of the results that we obtained using high-resolution simulations with *radiative hydrodynamics and star formation*, however for different reasons.

4.2 Limitations and future work

An accurate description of CRs should follow the evolution of the spectral energy distribution of CRs as a function of time and space, and keep track of their dynamical, non-linear coupling with the hydrodynamics. We made several simplifying assumptions to enable the task of following CR physics self-consistently in cosmological simulations of smoothed particle hydrodynamics (SPH). In the following, we outline the possibly most severe limitations of our approach for computing the non-thermal emission processes that will be addressed in future work (cf. Enßlin et al. 2007, for a more complete list of the assumptions of our CR formalism).

(i) We assumed a simple scaling of the magnetic energy density with the thermal energy density that allows us to effectively scan the observationally allowed parameter space for the magnetic field. Note that current SPH implementations that are capable of following magneto-hydrodynamics (MHD) are presently still fraught with numerical and physical difficulties, in particular when following dissipative gas physics (Dolag et al. 1999, 2005; Price & Monaghan 2004, 2005). While the inverse Compton and pion decay emission are mostly independent of the magnetic field, our synchrotron maps might be modified when the magneto-hydrodynamics is properly accounted for.

(ii) We neglected the population of re-accelerated electrons throughout this work: strong merger shocks and shear motions at the cluster periphery might inject hydrodynamic turbulence that cascades to smaller scales, feeds the MHD turbulence and eventually might be able to re-accelerate an aged CR electron population. Due to non-locality and intermittency of turbulence, this could partly smooth the very inhomogeneous primary emission component predominantly in the virial regions of clusters where simulations indicate a higher energy density in random motions. However, to study these effects, high-resolution AMR simulations are required that refine not only on the mass but also on some tracer for turbulence such as the dimensionless vorticity parameter.

(iii) In our model, the emphasis is given to the dynamical impact of CRs on hydrodynamics, and not on an accurate spectral representation of the CRs. The pion decay emission is almost independent on the spectral CR properties. However, the secondary CR component starts to be affected by this simplification since the dimensionless CR momentum $q \simeq 16\gamma_{\rm e}\, m_{\rm e}/m_{\rm p} \simeq 100$, that gives rise to synchrotron/IC emitting electrons with a Lorentz factor of $\gamma_{\rm e} \simeq 10^4$ is already quite high. Improving the spectral description of CR physics will not only allow us to study the spectral variations of the CR proton component but also enable reliable predictions for the TeV γ-ray emission. This is of great interest for imaging air Čerenkov telescopes.

(iv) We neglected microscopic CR diffusion in our simulations. The diffusivity can be rewritten into a macroscopic advection term that we fully resolve in our Lagrangian SPH simulations by construction and a microscopic diffusivity. The advection term dominates over microscopic term, in particular for merging clusters that are relevant for radio halos as the following estimate for the diffusivities shows: $\kappa_{\rm adv} = 100$ kpc 1000 km/s $= 10^{31.5}$ cm^2/s $\gg \kappa_{\rm diff} = 10^{29}$ cm^2/s.

(v) Our model of the diffusive shock acceleration mechanism assumes a featureless power-law for both, the proton and the electron acceleration, that is injected from the thermal distribution. The complete theoretical understanding of this mechanism is currently an active research topic that includes thermalization processes of the time evolution of the kinetic distribution of particles (Wolfe & Melia 2006) as well as non-linear effects and magnetic field amplification (Vladimirov et al. 2006). Phenomenologically however, we believe that there are strong indications for the diffusive shock acceleration mechanism to be at work which come from observations of supernova remnants over a wide range of wavelengths from the radio, X-rays into the TeV γ-rays (e.g., Ellison 2000; Hughes et al. 2000; Ellison & et al. 2005; Warren et al. 2005; Aharonian et al. 2004, 2006) as well as the bow shock of the Earth (Ellison et al. 1990; Shimada et al. 1999). Future work will be dedicated on improving our model to incorporate more elaborate plasma physical models and to study the uncertainty of our results with respect to the saturated value of our CR acceleration efficiency (e.g., Kang & Jones 2007; Edmon et al. 2007). Varying the physics in our simulations (non-radiative versus radiative) results in a very different Mach number distribution and changes the injection efficiency dramatically (Paper I). However, the resulting non-thermal emission is almost independent of the simulated physics. For this reason, we are confident that our model produces reliable results due to the self-regulated nature of CR proton feedback.

(vi) In this work, we did not account for feedback processes by AGN despite their importance for understanding the nature of the very X–ray luminous cool cores found in many clusters of galaxies. In particular we neglected an additional CR population that diffuses out of AGN-inflated bubbles and postpone their study to future work (Sijacki et al. 2007).

(vii) We furthermore neglected a hypothetical source of secondary electrons that are produced “in-situ” in dark matter (DM) neutralino annihilations (Colafrancesco et al. 2006). However, we see two main challenges associated with the DM model for giant radio halos. (1) Only a sub-class of clusters that seems to be associated with past or present merging events exhibit radio halos. This fact makes it hard to believe that the dark matter with its nearly universal density profile in halos (Navarro et al. 1996, 1997) could be responsible for such an infrequent cluster property, especially given the stringent upper limit on the diffuse radio emission in some massive clusters (Brunetti et al. 2007). (2) In order to explain the extended radio halo emission, the DM model needs to invoke a profile for the magnetic energy density, that increases by two orders of magnitude beyond the thermal core causing the plasma beta parameter to decrease by a factor of 220 to a value of 15. This behaviour is not only in contrast to the magnetic profile predicted by numerical MHD simulations of galaxy clusters Dolag et al. (2001) but also in contrast to turbulent dynamo models for the growth of the magnetic fields that will saturate on a level which is determined by the strength of the magnetic back-reaction (e.g., Subramanian 2003; Schekochihin & Cowley 2006) and is typically a fraction of the turbulent energy density. Observationally, it is clear that the rotation measure values towards radio galaxies show a larger dispersion for smaller projected separation from the cluster centre in a large rotation measure sample (Clarke et al. 2001). This is mainly due to the distribution of these sources within the cluster atmosphere causing some foreground objects to experiencing a small Faraday rotation depth which is however no argument in favour of a decreasing magnetic profile towards the cluster centre.

5 CONCLUSIONS

We find that the cosmic ray (CR) proton pressure traces the time integrated non-equilibrium activities of clusters and is only modulated by the recent dynamical activities. In contrast, the pressure of primary shock accelerated CR electrons resembles the current dynamical, non-equilibrium activity of forming structure and results in an inhomogeneous and aspherical spatial distribution. This is due to the different cooling time scales of CR electrons and protons and reflects their large mass difference. Hence, the radio synchrotron and inverse Compton emission of primary electrons provides a snapshot of violent non-equilibrium processes that are responsible for dissipating gravitational energy associated with structure formation such as merger shock waves. Signatures of this emission component are irregular morphologies, large spectral variations, and a high degree of synchrotron polarisation. On the other hand, non-thermal emission processes of pions and secondary CR electrons produced in hadronic CR proton interactions trace the comparably smooth CR proton distribution centred on the cluster that the CR protons accumulate over the Hubble time.

5.1 Radio synchrotron emission

Unified scheme: we propose a *unified scheme for the generation of giant radio halos*, *radio mini-halos*, and *radio relics* that naturally arises from our simulated radio synchrotron maps and emission profiles. It is schematically shown in a cartoon in Fig. 17. It predicts that the diffuse radio emission from a cluster varies with its dynamical stage as follows:

(i) Once a cluster relaxes and develops cool core, a *radio mini-halo* develops due to synchrotron emission of hadronically produced CR electrons. Adiabatic compression of magnetic fields during the formation of the cool core should confine the observable radio synchrotron emission to the cooling region of the cluster. Since the cooling gas accretes onto the central black hole, this triggers the radio mode feedback of the AGN. Radio emission from the jet typically outshines the diffuse mini-halo which implies a high dynamic flux range. This leads to a negative selection effect that disfavours the detection of radio mini-halos or makes it very challenging.

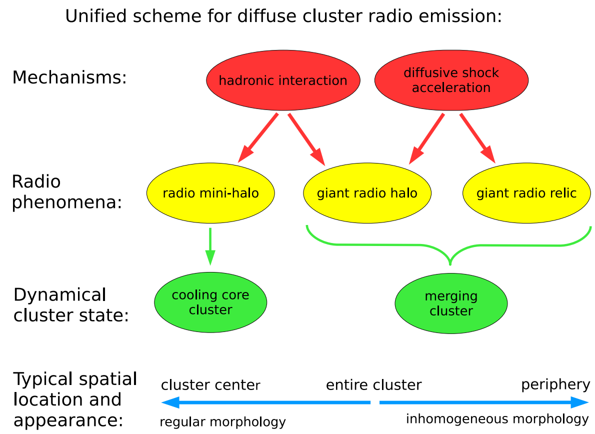

Figure 17. A cartoon showing our unified scheme for the diffuse cluster emission. Hadronic cosmic ray proton interactions with ambient protons of the thermal ICM are thought to be responsible for radio mini-halos in cooling core clusters and the central parts of giant cluster radio halos in merging clusters. This emission mechanism produces a regular cluster-wide morphology resembling the thermal bremsstrahlung emission. In contrast, the radio synchrotron emission of shock accelerated cosmic ray electrons (through the Fermi 1 mechanism) is believed to be responsible for giant radio relics that have an inhomogeneous morphology and are primarily located at the cluster periphery.

(ii) If a cluster experiences a major merger, two leading shock waves are produced at first core passage that move outwards and become stronger as they break at the shallow peripheral cluster potential. Relativistic electrons are efficiently accelerated by means of diffusive shock acceleration and magnetic fields are amplified by shock compression and MHD turbulence at these shocks. Due to the short cooling times of $\tau \sim 10^8$ yrs, the synchrotron radiating electrons are confined to a narrow emission volume around the shock wave. In combination with the preferred magnetic field direction in the shock surface, this implies a high degree of synchrotron polarisation. The observer will typically observe one or two large-scale *radio relics*, depending on the merger characteristics such as the relative cluster masses, concentrations, and gas fractions, the merger geometry with respect to the line-of-sight, as well as the time dependent merger stage. Our cosmological simulations supports the picture put forward in isolated cluster merging simulations (Roettiger et al. 1996).

(iii) Simultaneously, virialisation of the gravitational energy, that is associated with the merger, generates a morphologically complex network of shock waves. The lower sound speed in the cluster outskirts imply stronger shocks that accelerate a spatially irregular distribution of CR electrons in these regions. The injected MHD turbulence amplifies magnetic fields through strong shear motions and turbulent dynamo processes. The induced radio synchrotron emission traces these non-equilibrium processes similarly as the water ‘gischt’ traces breaking non-linear waves. A *giant radio halo* develops due to (1) boost of the hadronically generated radio emission in the centre and a transition to the (2) irregular radio ‘gischt’ emission in the cluster outskirts that represents radio synchrotron radiation emitted from primary, shock-accelerated electrons.

Predictions: The observational consequences of our unified scheme can be summarised as follows:

(i) Clusters undergoing major mergers are expected to have a giant radio halo with an extended radio synchrotron emission region ($R_{\mathrm{halo}} \simeq 0.5\,R_{200}$) while relaxed cool core clusters should host a smaller radio-mini halo.

(ii) Our simulated radio luminosities reproduce observed luminosities of halos/relics for magnetic fields derived from Faraday rotation measurements (cf. Paper III).

(iii) The regular morphology of the central parts of giant radio halos is a consequence of the dominant contribution of hadronically produced electrons.

(iv) The morphology and the radio spectral index in the radio halo periphery is predicted to show large variations due to the dominant contribution from primary CR electrons generated by shock waves. Superposing in projection many causally disconnected synchrotron emitting shock regions with different shock strength and thus electron spectral indices leads to spectral variations.

(v) The amount of the primary radio emission depends critically on the characteristics of the merger. We thus expect a large scatter in the scaling relation of the radio halo luminosities with cluster mass as well as in the pixel-to-pixel correlation of the thermal X-ray brightness with radio surface brightness.

(vi) The central radio emission should be Faraday depolarised assuming statistically isotropic distribution of magnetic field while the external emission regions are expected to have a small degree of polarisation. As a word of caution, in order to detect this polarisation one might be forced to go out to large impact parameters where the resulting synchrotron surface brightness is small and the emission is dominated by very few contributing emission regions along the line-of-sight.

These predictions from our cosmological high-resolution simulations successfully reproduce characteristics of observed radio relics, giant radio halos, as well as radio mini halos (Feretti et al. 2004; Cassano et al. 2006). In our approach, we choose the magnetic energy density to scale with the thermal energy. The formation of a cool core is expected to compress the magnetic field adiabatically and should be responsible for the peaked central radio mini-halo emission profile. This effect should reinforce our observed difference in emission size between giant radio halos and mini-halos.

The observed correlation between radio halos and merging clusters implies a departure of these systems from hydrostatic equilibrium and leads to a complicated non-spherical morphology. The resulting X-ray mass estimates are subject to large uncertainties which makes the analysis and theoretical model building based on azimuthally averaged quantities questionable if not impossible since it causes loss of information and might yield biased results. For this reason, we analyse *pixel-to-pixel correlations* of the thermal X-ray surface brightness with non-thermal cluster emission processes. We find that the hadronically induced non-thermal emission is tightly correlated with the thermal bremsstrahlung emission with the slope depending on the realisation of the magnetic field. In contrast, the correlation is much weaker and the scatter is increased in the case of primary non-thermal emission where structures in the correlation space density correspond to individual structure formation shock waves. This implies that in general, simulations will only be able to provide quantitative predictions for the statistical behaviour rather than deterministic predictions for the correlations. Our new radio halo model matches qualitatively the observed tight correlation at high surface brightness which broadens and flattens towards dimmer brightness (cf. Govoni et al. 2001). However, our correlation is slightly steeper than observed ones. Taking into account the uncertainty of the magnetic field model we conclude that observed pixel-to-pixel correlations support our model.

Future: What can we learn from a future, large sample of clusters that show diffuse radio emission?

(i) Radio relics and giant radio halos occur in dynamically merging clusters and indicate a departure of these systems from hydrostatic equilibrium and spherical symmetry. This has to be taken into account in the derivation of the cluster mass.

(ii) The orthogonal information about the dynamical cluster activity, that in general can not be obtained from the thermal cluster observables such as X-ray emission and Sunyaev-Zel'dovich effect, will help us in constructing a 'gold cluster sample' for cosmology.

(iii) The property of the spatially confined radio relic emission from shock accelerated electrons might be employed to solve the inversion problem of reconstructing the course of a merger event given the thermal and radio synchrotron observables.

(iv) Combining high-resolution X-ray, Sunyaev-Zel'dovich, and radio observations will allow us to probe fundamental plasma physics: diffusive shock acceleration, large scale magnetic fields, and turbulence.

5.2 Inverse Compton and γ-ray emission

In principle, inverse Compton (IC) emission and high-energy γ-ray emission from decaying pions, produced in hadronic CR interactions, is the cleanest way of probing current structure formation shock waves as well as time integrated non-equilibrium cluster activity. This is because these non-thermal emission components are not weighted with the magnetic energy density as it is the case for synchrotron emission. Our main findings can be summarised as follows.

(i) We identify two main regions for the generation of non-thermal emission in clusters of galaxies: the core that is also emitting thermal X-rays and the virial regions where the accretion shocks reside and merging shock waves break at the shallower cluster potential.

(ii) In the *cluster core regions*, the emission for energies $E_\gamma >$ 100 MeV is dominated by pion decay γ-rays. At lower energies, the IC emission from secondary CR electrons dominate the emission. Only in merging clusters, the situation may be reversed for the *outer cluster regions* where the primary IC emission can attain a similar flux level as the pion decay emission and even exceed the secondary IC emission at lower energies.

(iii) While the total high-energy γ-ray emission is always dominated by the pion decay component irrespective of the clusters dynamical state, the total hard X-ray IC emission can be dominated by either primary or secondary emission components, depending whether a major merger takes place that boosts the primary IC emission.

(iv) A corollary of this is that the high-energy γ-ray emission can be reliably predicted for massive clusters using a scaling relation of non-thermal emission and the cluster mass. In contrast, the hard X-ray emission of even massive clusters is subject to large flux variations that depend sensitively on the dynamical state of the cluster.

(v) Due to larger variation of merging histories and the smaller gravitational potential in less massive systems, their CR pressure and the associated γ-ray emission level is subject to larger modulation and reflects more sensitively the current merging activity of the cluster than it is the case in large systems.

(vi) The morphology of the pion decay as well as the secondary

IC component resemble the thermal X-ray emission albeit they decrease less steeply with growing radius and extend further out. This is due to the increasing CR number fraction $f_{\rm CR} = n_{\rm CR}/n_{\rm th}$ with increasing radius and reflects the more efficient CR acceleration at stronger shocks in the cluster periphery. The morphology of the primary IC emission is irregularly shaped and traces current non-equilibrium phenomena such as merger or accretion shock waves.

(vii) Possibly most surprising, we find that the dominant emission component at the centre (primary or secondary IC for $E_\gamma >$ 10 keV and pion decay γ-rays for $E_\gamma >$ 100 MeV) depends only weakly on whether radiative or non-radiative gas physics is simulated provided we consider in both cases only CRs from structure formation shocks. This is mainly due to self-regulating effects of the CR pressure.

(viii) Measuring the hard X-ray and γ-ray emission will have a huge astrophysical impact and teach us about: the CR pressure contribution to the intra-cluster medium, the generating mechanisms of radio halos (such that we can use them in addition to thermal observables to characterise clusters), the contribution of the pion decay emission as well as the primary and secondary IC radiation to the γ-ray background.

(ix) Detecting the non-thermal spectrum ranging from X-rays to γ-rays will enable us to probe fundamental plasma physics on large cluster scales such as inferring the energy conversion efficiency of diffusive shock acceleration of protons and electrons as well as probing the large scale magnetic fields.

ACKNOWLEDGEMENTS

All computations were performed on CITA's McKenzie cluster (Dubinski et al. 2003) which was funded by the Canada Foundation for Innovation and the Ontario Innovation Trust.

REFERENCES

Abramowitz M., Stegun I. A., 1965, Handbook of mathematical functions. New York: Dover
Aharonian F., Akhperjanian A. G., Bazer-Bachi A. R., Beilicke M., Benbow W., Berge D., Bernlöhr K., Boisson C., Bolz O., Borrel V., Braun I., Breitling F., et al. 2006, Nature, 439, 695
Aharonian F. A., Akhperjanian A. G., Aye K.-M., Bazer-Bachi A. R., Beilicke M., Benbow W., Berge D., Berghaus P., Bernlöhr K., Bolz O., Boisson C., Borgmeier C., et al. 2004, Nature, 432, 75
Badhwar G. D., Golden R. L., Stephens S. A., 1977, Phys. Rev. D, 15, 820
Bagchi J., Durret F., Neto G. B. L., Paul S., 2006, Science, 314, 791
Bell A. R., 1978a, MNRAS, 182, 147
Bell A. R., 1978b, MNRAS, 182, 443
Berezhko E. G., Yelshin V. K., Ksenofontov L. T., 1994, Astroparticle Physics, 2, 215
Berezinsky V. S., Blasi P., Ptuskin V. S., 1997, ApJ, 487, 529
Berrington R. C., Dermer C. D., 2003, ApJ, 594, 709
Blandford R., Eichler D., 1987, Phys. Rep., 154, 1
Blasi P., Colafrancesco S., 1999, Astroparticle Physics, 12, 169
Bridle A. H., Fomalont E. B., 1976, A&A, 52, 107
Bridle A. H., Fomalont E. B., Miley G. K., Valentijn E. A., 1979, A&A, 80, 201
Brunetti G., Blasi P., Cassano R., Gabici S., 2004, MNRAS, 350, 1174
Brunetti G., Lazarian A., 2007, MNRAS, 378, 245
Brunetti G., Setti G., Feretti L., Giovannini G., 2001, MNRAS, 320, 365
Brunetti G., Venturi T., Dallacasa D., Cassano R., Dolag K., Giacintucci S., Setti G., 2007, ApJL, 670, L5
Cassano R., Brunetti G., Setti G., 2006, MNRAS, 369, 1577
Cen R., Ostriker J. P., 1999, ApJ, 514, 1
Clarke T. E., Enßlin T. A., 2006, AJ, 131, 2900
Clarke T. E., Kronberg P. P., Böhringer H., 2001, ApJL, 547, L111
Colafrancesco S., Blasi P., 1998, Astroparticle Physics, 9, 227
Colafrancesco S., Profumo S., Ullio P., 2006, A&A, 455, 21
Davé R., Cen R., Ostriker J. P., Bryan G. L., Hernquist L., Katz N., Weinberg D. H., Norman M. L., O'Shea B., 2001, ApJ, 552, 473
Deiss B. M., Reich W., Lesch H., Wielebinski R., 1997, A&A, 321, 55
Dennison B., 1980, ApJL, 239, L93
Dermer C. D., 1986a, ApJ, 307, 47
Dermer C. D., 1986b, A&A, 157, 223
Dolag K., Bartelmann M., Lesch H., 1999, A&A, 348, 351
Dolag K., Enßlin T. A., 2000, A&A, 362, 151
Dolag K., Grasso D., Springel V., Tkachev I., 2005, Journal of Cosmology and Astro-Particle Physics, 1, 9
Dolag K., Schindler S., Govoni F., Feretti L., 2001, A&A, 378, 777
Drury L., 1983a, Space Science Reviews, 36, 57
Drury L. O., 1983b, Reports of Progress in Physics, 46, 973
Drury L. O., Markiewicz W. J., Völk H. J., 1989, A&A, 225, 179
Dubinski J., Humble R. J., Loken C., Pen U.-L., Martin P. G., 2003, in Proc. of the 17th Annual International Symposium on High Performance Computing Systems and Applications: McKenzie: A Teraflops Linux Beowulf Cluster for Computational Astrophysics
Eckert D., Neronov A., Courvoisier T. J.-L., Produit N., 2007, A&A, 470, 835
Eckert D., Produit N., Paltani S., Neronov A., Courvoisier T. J. ., 2007, ArXiv:0712.2326
Edmon P. P., Jones T. W., Kang H., 2007, ArXiv:0706.0587
Eke V. R., Cole S., Frenk C. S., 1996, MNRAS, 282, 263
Ellison D. C., 2000, in Mewaldt R. A., Jokipii J. R., Lee M. A., Möbius E., Zurbuchen T. H., eds, Acceleration and Transport of Energetic Particles Observed in the Heliosphere Vol. 528 of American Institute of Physics Conference Series, The Cosmic Ray-X-ray Connection: Effects of Nonlinear Shock Acceleration on Photon Production in SNRs. p. 383
Ellison D. C., et al. 2005, in International Cosmic Ray Conference Vol. 3 of International Cosmic Ray Conference, Thermal Particle Injection in Nonlinear Diffusive Shock Acceleration. p. 261
Ellison D. C., Jones F. C., Eichler D., 1981, Journal of Geophysics Zeitschrift Geophysik, 50, 110
Ellison D. C., Moebius E., Paschmann G., 1990, ApJ, 352, 376
Ensslin T. A., Biermann P. L., Klein U., Kohle S., 1998, A&A, 332, 395
Ensslin T. A., Biermann P. L., Kronberg P. P., Wu X.-P., 1997, ApJ, 477, 560
Enßlin T. A., Pfrommer C., Springel V., Jubelgas M., 2007, A&A, 473, 41
Feretti L., Brunetti G., Giovannini G., Kassim N., Orrú E., Setti G., 2004, Journal of Korean Astronomical Society, 37, 315
Fermi E., 1950, Prog. Theor. Phys., 5, 570

Furlanetto S. R., Loeb A., 2004, ApJ, 611, 642
Fusco-Femiano R., dal Fiume D., Feretti L., Giovannini G., Grandi P., Matt G., Molendi S., Santangelo A., 1999, ApJL, 513, L21
Fusco-Femiano R., Landi R., Orlandini M., 2007, ApJL, 654, L9
Fusco-Femiano R., Orlandini M., Brunetti G., Feretti L., Giovannini G., Grandi P., Setti G., 2004, ApJL, 602, L73
Giovannini G., Tordi M., Feretti L., 1999, New Astronomy, 4, 141
Gitti M., Ferrari C., Domainko W., Feretti L., Schindler S., 2007, A&A, 470, L25
Gould R. J., 1972a, Physica, 58, 379
Gould R. J., 1972b, Physica, 60, 145
Govoni F., Enßlin T. A., Feretti L., Giovannini G., 2001, A&A, 369, 441
Haardt F., Madau P., 1996, ApJ, 461, 20
Hellsten U., Gnedin N. Y., Miralda-Escudé J., 1998, ApJ, 509, 56
Hernquist L., Katz N., 1989, ApJS, 70, 419
Hughes J. P., Rakowski C. E., Decourchelle A., 2000, ApJL, 543, L61
Jaffe W. J., 1977, ApJ, 212, 1
Jones T. W., Kang H., 1993, ApJ, 402, 560
Jubelgas M., Springel V., Enßlin T. A., Pfrommer C., 2007, A&A, in print, arXiv:astro-ph/0603485
Kang H., Jones T. W., 1995, ApJ, 447, 944
Kang H., Jones T. W., 2007, Astroparticle Physics, 28, 232
Kang H., Ryu D., Cen R., Song D., 2005, ApJ, 620, 21
Katz N., Weinberg D. H., Hernquist L., 1996, ApJS, 105, 19
Katz N., White S. D. M., 1993, ApJ, 412, 455
Kempner J. C., Blanton E. L., Clarke T. E., Enßlin T. A., Johnston-Hollitt M., Rudnick L., 2004, in The Riddle of Cooling Flows in Galaxies and Clusters of galaxies, Conference Note: A Taxonomy of Extended Radio Sources in Clusters of Galaxies. p. 335
Keshet U., Waxman E., Loeb A., Springel V., Hernquist L., 2003, ApJ, 585, 128
Kim K. ., Kronberg P. P., Giovannini G., Venturi T., 1989, Nature, 341, 720
Kuo P., Bowyer S., Hwang C., 2005, ApJ, 618, 675
Liang H., Hunstead R. W., Birkinshaw M., Andreani P., 2000, ApJ, 544, 686
Loeb A., Waxman E., 2000, Nature, 405, 156
Malkov M. A., O'C Drury L., 2001, Reports of Progress in Physics, 64, 429
Malkov M. A., Völk H. J., 1998, Advances in Space Research, 21, 551
Malkov M. A., Völk H. J., 1995, A&A, 300, 605
Marchegiani P., Perola G. C., Colafrancesco S., 2007, A&A, 465, 41
Masson C. R., Mayer C. J., 1978, MNRAS, 185, 607
Miniati F., 2001, Computer Physics Communications, 141, 17
Miniati F., 2002, MNRAS, 337, 199
Miniati F., 2003, MNRAS, 342, 1009
Miniati F., Ryu D., Kang H., Jones T. W., 2001a, ApJ, 559, 59
Miniati F., Jones T. W., Kang H., Ryu D., 2001b, ApJ, 562, 233
Miniati F., Ryu D., Kang H., Jones T. W., Cen R., Ostriker J. P., 2000, ApJ, 542, 608
Molendi S., 2007, private communication
Navarro J. F., Frenk C. S., White S. D. M., 1996, ApJ, 462, 563
Navarro J. F., Frenk C. S., White S. D. M., 1997, ApJ, 490, 493
Ohno H., Takizawa M., Shibata S., 2002, ApJ, 577, 658
Pedlar A., Ghataure H. S., Davies R. D., Harrison B. A., Perley R., Crane P. C., Unger S. W., 1990, MNRAS, 246, 477
Petrosian V., Madejski G., Luli K., 2006, ApJ, 652, 948
Pfrommer C., 2007, ArXiv:0707.1693
Pfrommer C., Enßlin T. A., 2003, A&A, 407, L73
Pfrommer C., Enßlin T. A., 2004a, A&A, 413, 17
Pfrommer C., Enßlin T. A., 2004b, MNRAS, 352, 76
Pfrommer C., Enßlin T. A., Springel V., Jubelgas M., Dolag K., 2007, MNRAS, 378, 385
Pfrommer C., Springel V., Enßlin T. A., Jubelgas M., 2006, MNRAS, 367, 113
Price D. J., Monaghan J. J., 2004, MNRAS, 348, 139
Price D. J., Monaghan J. J., 2005, MNRAS, 364, 384
Reimer O., Pohl M., Sreekumar P., Mattox J. R., 2003, ApJ, 588, 155
Reiprich T. H., Böhringer H., 2002, ApJ, 567, 716
Rephaeli Y., Gruber D., 2002, ApJ, 579, 587
Rephaeli Y., Gruber D., 2003, ApJ, 595, 137
Rephaeli Y., Gruber D., Blanco P., 1999, ApJL, 511, L21
Roettiger K., Burns J. O., Loken C., 1996, ApJ, 473, 651
Rossetti M., Molendi S., 2004, A&A, 414, L41
Rossetti M., Molendi S., 2007, astro-ph/0702417
Rottgering H., Snellen I., Miley G., de Jong J. P., Hanisch R. J., Perley R., 1994, ApJ, 436, 654
Röttgering H. J. A., Wieringa M. H., Hunstead R. W., Ekers R. D., 1997, MNRAS, 290, 577
Rybicki G. B., Lightman A. P., 1979, Radiative processes in astrophysics. New York, Wiley-Interscience
Ryu D., Kang H., Hallman E., Jones T. W., 2003, ApJ, 593, 599
Sanders J. S., Fabian A. C., Dunn R. J. H., 2005, MNRAS, 360, 133
Sarazin C. L., 1988, X-ray emission from clusters of galaxies. Cambridge Astrophysics Series, Cambridge: Cambridge University Press, 1988
Sarazin C. L., 1999, ApJ, 520, 529
Sarazin C. L., 2002, in ASSL Vol. 272: Merging Processes in Galaxy Clusters The Physics of Cluster Mergers. pp 1–38
Schekochihin A. A., Cowley S. C., 2006, Physics of Plasmas, 13, 6501
Schlickeiser R., Sievers A., Thiemann H., 1987, A&A, 182, 21
Shimada N., Terasawa T., Hoshino M., Naito T., Matsui H., Koi T., Maezawa K., 1999, Ap&SS, 264, 481
Sijacki D., Pfrommer C., Springel V., Enßlin T., 2007, MNRAS, submitted
Sijacki D., Springel V., 2006, MNRAS, 366, 397
Springel V., 2005, MNRAS, 364, 1105
Springel V., Hernquist L., 2002, MNRAS, 333, 649
Springel V., Hernquist L., 2003, MNRAS, 339, 289
Springel V., Yoshida N., White S. D. M., 2001, New Astronomy, 6, 79
Stecker F. W., 1970, Ap&SS, 6, 377
Stecker F. W., 1971, Cosmic gamma rays. Baltimore: Mono Book Corp.
Stephens S. A., Badhwar G. D., 1981, Ap&SS, 76, 213
Subramanian K., 2003, Physical Review Letters, 90, 245003
Sunyaev R. A., Zeldovich Y. B., 1972, Comments on Astrophysics and Space Physics, 4, 173
Vestrand W. T., 1982, AJ, 87, 1266
Vladimirov A., Ellison D. C., Bykov A., 2006, ApJ, 652, 1246
Voit G. M., 2005, Reviews of Modern Physics, 77, 207
Völk H. J., Aharonian F. A., Breitschwerdt D., 1996, Space Science Reviews, 75, 279
Warren J. S., Hughes J. P., Badenes C., Ghavamian P., McKee C. F., Moffett D., Plucinsky P. P., Rakowski C., Reynoso E., Slane P., 2005, ApJ, 634, 376

Widrow L. M., 2002, Reviews of Modern Physics, 74, 775
Wolfe B., Melia F., 2006, ApJ, 638, 125
Yoshida N., Sheth R. K., Diaferio A., 2001, MNRAS, 328, 669

APPENDIX A: RELATIVISTIC ELECTRON POPULATIONS

A1 Definitions

Throughout the paper we use the following definitions for the differential source function $q(\boldsymbol{r}, E)$, the emissivity $j(\boldsymbol{r}, E)$ and the volume integrated quantities, respectively:

$$q(\boldsymbol{r}, E) = \frac{\mathrm{d}^3 N}{\mathrm{d}t\,\mathrm{d}V\,\mathrm{d}E}\,, \qquad j(\boldsymbol{r}, E) = E\, q(\boldsymbol{r}, E)\,, \tag{A1}$$

$$Q(E) = \int \mathrm{d}V\, q(\boldsymbol{r}, E)\,, \qquad J(E) = E\, Q(E)\,, \tag{A2}$$

where N denotes the integrated number of particles. From the source function the integrated number density production rate of particles $\lambda(\boldsymbol{r})$, the number of particles produced per unit time interval within a certain volume, $\mathcal{L}$, and the particle flux $\mathcal{F}$ can be derived. The definitions of the energy weighted quantities are denoted on the right hand side, respectively,

$$\lambda(\boldsymbol{r}) = \int \mathrm{d}E\, q(\boldsymbol{r}, E)\,, \qquad \Lambda(\boldsymbol{r}) = \int \mathrm{d}E\, E\, q(\boldsymbol{r}, E)\,, \tag{A3}$$

$$\mathcal{L} = \int \mathrm{d}V\, \lambda(\boldsymbol{r})\,, \qquad L = \int \mathrm{d}V\, \Lambda(\boldsymbol{r})\,, \tag{A4}$$

$$\mathcal{F} = \frac{\mathcal{L}}{4\,\pi\, D^2}\,, \qquad F = \frac{L}{4\,\pi\, D^2}\,. \tag{A5}$$

A2 Timescales

This section presents general considerations for deriving the characteristic electron momentum scales of the distribution function. To this end, we compare the energy loss timescales $\tau_\mathrm{loss} = -E/\dot{E}_\mathrm{loss}$ to the acceleration timescales as a function of particle kinetic energy for the most important processes in this context. The detailed calculations for the equipartition distribution of CR electrons can be found in the next two sections. The particle kinetic energy $E/(m_\mathrm{e} c^2) = \gamma - 1 = (1-\beta^2)^{-1/2} - 1$ is defined in terms of the Lorentz factor γ and the velocity of the electron, βc. Energy loss processes due to Coulomb interactions (Gould 1972b), inverse Compton (IC) and synchrotron emission (Rybicki & Lightman 1979) are defined as follows:

$$-\dot{E}_\mathrm{Coul} = \frac{3\,\sigma_\mathrm{T}\, m_\mathrm{e} c^3\, n_\mathrm{e}}{2\beta}\left[\ln\left(\frac{m_\mathrm{e} c^2\, \beta\, \sqrt{\gamma - 1}}{\hbar\omega_\mathrm{pl}}\right) - \left(\frac{\beta^2}{2} + \frac{1}{\gamma}\right)\ln 2 + \frac{1}{2} + \left(\frac{\gamma - 1}{4\gamma}\right)^2\right], \tag{A6}$$

$$-\dot{E}_\mathrm{IC,synch} = \frac{4}{3}\,\sigma_\mathrm{T}\, c\, \left(\varepsilon_\mathrm{ph} + \varepsilon_B\right)\gamma^2\beta^2. \tag{A7}$$

Here $\sigma_\mathrm{T} = 8\pi r_\mathrm{e}^2/3$ is the Thomson cross section, $r_\mathrm{e} = e^2/(m_\mathrm{e} c^2)$ the classical electron radius, $\omega_\mathrm{pl} = \sqrt{4\pi e^2 n_\mathrm{e}/m_\mathrm{e}}$ is the plasma frequency, and n_e is the number density of free electrons. IC losses of electrons depend on the energy density of the cosmic microwave background (CMB) and the starlight photon field, $\varepsilon_\mathrm{ph} = \varepsilon_\mathrm{CMB} + \varepsilon_\mathrm{stars}$, where we neglect the latter one for simplicity and express $\varepsilon_\mathrm{CMB} = B_\mathrm{CMB}^2/(8\pi)$ by an equivalent field strength $B_\mathrm{CMB} = 3.24\,(1+z)^2\,\mu\mathrm{G}$. Synchrotron losses of an isotropic pitch angle distribution of electrons depend on the energy density of the local magnetic field, $\varepsilon_B = \langle B^2\rangle/(8\pi)$, where $B = \sqrt{\langle \boldsymbol{B}^2\rangle}$ is the *rms* of the magnetic vector field $\boldsymbol{B}$. Comparing these two loss processes, we obtain a synchrotron dominated cooling regime for $B > B_\mathrm{CMB}$ and an IC dominated regime in the weak field limit. The timescale for CR electron injection by means of hadronic interactions of CR protons with ambient protons of the thermal plasma is given by:

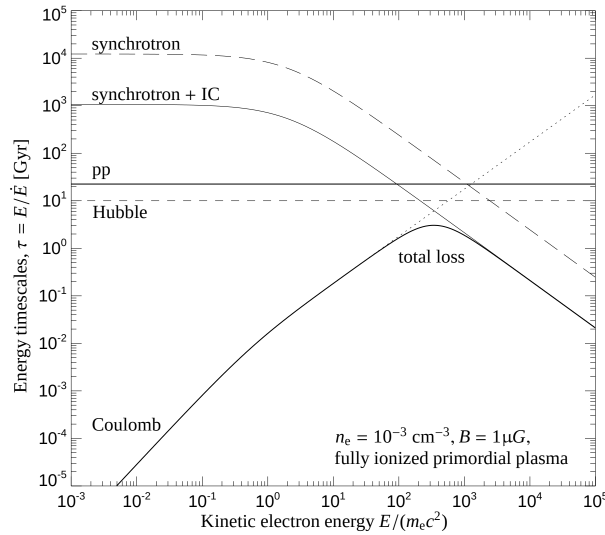

Figure A1. Energy gain and loss timescales as a function of the kinetic energy of electrons for typical conditions of the ICM. The three solid lines from the bottom to the top denote the total loss timescale for electrons, the timescale due to hadronic injection of secondary electrons (pp), and the combined inverse Compton (IC)/synchrotron cooling timescale. The dotted line shows the Coulomb timescale, the long dashed one the synchrotron timescale, and the dashed one the Hubble time. Note that the relative normalisation of the hadronic injection timescale compared to the total loss timescale is subject to different density dependencies and the shock acceleration timescale depends crucially on the properties of structure formation shocks.

$$-\dot{E}_\mathrm{pp} = E\, c\, \bar{\sigma}_\mathrm{pp}\, n_\mathrm{N}, \tag{A8}$$

where $\bar{\sigma}_\mathrm{pp} = 32$ mbarn is the average inelastic cross section for proton-proton interactions, $n_\mathrm{N} = n_\mathrm{H} + 4 n_\mathrm{He} = \rho/m_\mathrm{p}$ is the number density of target nucleons.

Comparing the different energy gain and loss rates of relativistic electrons yields characteristic momentum scales that are responsible for spectral breaks or cutoffs in the CR electron distribution function. Conveniently, we denote these characteristic momentum scales with the dimensionless electron momentum $q = \beta\gamma = P_\mathrm{e}\,(m_\mathrm{e} c)^{-1}$ and label these with the competing processes considered. Equating the timescale for Coulomb interactions and IC/synchrotron losses yields

$$q_\mathrm{Coul,IC/synch} = \left\{\frac{9\, m_\mathrm{e} c^2\, n_\mathrm{e}}{8\left(\varepsilon_\mathrm{ph} + \varepsilon_B\right)}\left[\ln\left(\frac{m_\mathrm{e} c^2 \langle\gamma^{1/2}\rangle}{\hbar\omega_\mathrm{pl}}\right) + 0.216\right]\right\}^{1/2} \simeq 300\left(\frac{n_\mathrm{e}}{10^{-3}\mathrm{cm}^{-3}}\right)^{1/2}. \tag{A9}$$

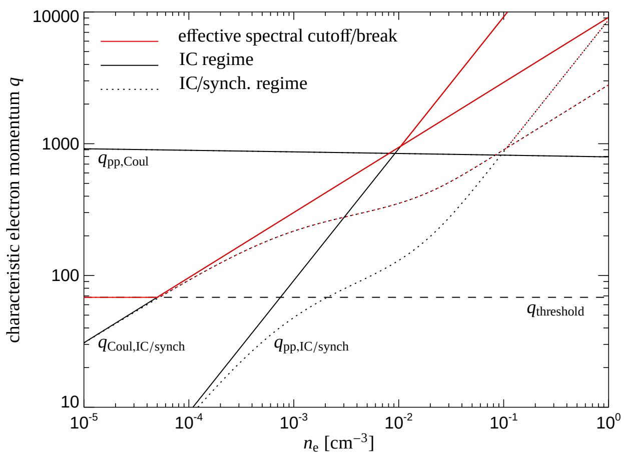

Figure A2. Density dependence of characteristic momentum scales $q = P_{\rm e}\,(m_{\rm e} c)^{-1}$ for a hadronically injected *secondary CR electron population*. Comparing the different energy gain and loss rates of competing processes such as hadronic injection of secondary electrons (pp), Coulomb cooling, and IC/synchrotron cooling yields characteristic momentum scales that are responsible for spectral breaks or cutoffs in the CR electron distribution function. The solid red line denotes the effective spectral cutoff: for $n_{\rm e} \lesssim 10^{-2}$ cm^{-3}, it denotes the lower cutoff of the power-law distribution function. At higher densities, it denotes the lower cutoff $q_{\rm Coul,IC}$ and the spectral break ($q_{\rm pp,IC}$) of the broken power-law spectrum. The dotted lines include synchrotron losses and assume a scaling of the magnetic field of $\varepsilon_B \propto \varepsilon_{\rm th}$ with a saturation value for B at $B_{\rm max} = 10\,\mu$G.

In the last step and the following numerical examples, we assume the IC cooling regime for simplicity. This energy scale provides a bottleneck through which high-energy electrons have to pass when they age and one expects a characteristic pile-up at this energy scale in their distribution function for an integration over the energy injection history of different CR electron populations (Sarazin 1999).

The timescale for diffusive shock acceleration of electrons at cosmological shock waves is much shorter than cosmologically relevant timescales, $\tau_{\rm shock} \ll 1$ Gyr. This implies that $\tau_{\rm shock}$ intersects the total loss timescale in the low-energy Coulomb regime, $\tau_{\rm Coul}$, as well as in the high-energy IC/synchrotron regime, $\tau_{\rm IC/synch}$ (cf. Fig. A1). We can thus identify two characteristic momenta of the *primary population of electrons* that are obtained by equating $\tau_{\rm shock}$ with the Coulomb and the IC/synchrotron timescale,

$$q_{\rm inj,IC/synch} = \frac{3\,m_{\rm e} c}{4\,\sigma_{\rm T} \tau_{\rm inj}\,(\varepsilon_B + \varepsilon_{\rm ph})}, \qquad \text{(A10)}$$

$$q_{\rm inj,Coul} = \frac{3}{2}\,\sigma_{\rm T} c\, n_{\rm e}\,\tau_{\rm inj}\left[\ln\left(\frac{m_{\rm e}c^2\,\langle\gamma^{1/2}\rangle}{\hbar\omega_{\rm pl}}\right) + 0.216\right]. \qquad \text{(A11)}$$

At high energies, we expect to have an IC/synchrotron cooled electron spectrum that joins at lower energies into the shock injection spectrum of CR electrons that have had no time to cool radiatively yet. The low momentum cutoff of the CR electron distribution function is determined by Coulomb losses.

Characteristic momenta of the *secondary population of electrons* are obtained by equating the energy injection rate through hadronic proton interactions with the energy loss rates,

$$q_{\rm threshold} = \frac{m_{\pi^\pm}}{4\,m_{\rm e}} \simeq 70, \qquad \text{(A12)}$$

$$q_{\rm pp,IC/synch} = \frac{3\,\bar\sigma_{pp}\,n_{\rm N}\,m_{\rm e}\,c^2}{4\,\sigma_{\rm T}\left(\varepsilon_{\rm ph} + \varepsilon_B\right)} \simeq 70\left(\frac{n_{\rm e}}{10^{-3}{\rm cm}^{-3}}\right), \qquad \text{(A13)}$$

$$q_{\rm pp,Coul} = \frac{3\,\sigma_{\rm T}\,n_{\rm e}}{2\,\bar\sigma_{\rm pp}\,n_{\rm N}}\left[\ln\left(\frac{m_{\rm e}c^2\,\langle\gamma^{1/2}\rangle}{\hbar\omega_{\rm pl}}\right) + 0.216\right] \qquad \text{(A14)}$$
$$\simeq 1300 - \ln\left(\frac{n_{\rm e}}{10^{-3}{\rm cm}^{-3}}\right)^{1/2}.$$

$q_{\rm threshold}$ reflects the threshold momentum for the inelastic proton-proton reaction. The shortest equipartition timescale at these characteristic momenta dominates the resulting electron equilibrium distribution. In the case of a double-valued solution for q, i.e. when we obtain two equipartition cutoffs with a similar timescale, we choose the larger one which is in equilibrium with the IC/synchrotron cooling. All these momentum scales have different density dependencies which are visualised in Fig. A2. At typical densities of the ICM for $n_{\rm e} \lesssim 10^{-2}$ cm^{-3}, the two momentum scales $q_{\rm pp,IC/synch}$ and $q_{\rm pp,Coul}$ have an associated timescale that is much longer than the timescale at $q_{\rm Coul,IC/synch}$ as can be readily inferred from Fig. A1. This implies that the equilibrium distribution function of secondary CR electrons has a low-energy cutoff at $q_{\rm Coul,IC/synch}$.

The situation is reversed for the dense ICM or the inter-stellar medium with electron densities $n_{\rm e} \gtrsim 10^{-2}$ cm^{-3} (assuming the IC dominated cooling regime), and the momentum scale $q_{\rm Coul,IC/synch}$ drops out of the problem due to its long timescale. The equilibrium distribution function of secondary CR electrons develops a break at $q_{\rm pp,IC/synch}$ above which the secondary electron injection is in equilibrium with IC/synchrotron cooling and below which the electron injection spectrum remains unchanged (similar to the case of the primary CR electron population). The lower cutoff of the distribution function is given by $q_{\rm pp,Coul}$, provided it exceeds the threshold $q_{\rm threshold}$ for the hadronic reaction and provided the CR proton distribution extends down to these low energies. The effective spectral cutoff $q_{\rm eff}$ of the electron distribution function is visualised in Fig. A2 as a *solid red line*. For $n_{\rm e} \lesssim 10^{-2}$ cm^{-3}, we have a simple power-law with a lower cutoff given by $q_{\rm eff}$. At higher densities, the lower solid red line denotes again the cutoff of the distribution function, while the upper red line (that coincides with $q_{\rm pp,IC}$) denotes the spectral break above which the hadronic injection and IC/synchrotron cooling established a steady state spectrum.

So far, we only considered regime of weak magnetic fields where IC cooling dominates. The complete picture including synchrotron cooling is however only slightly changed due to the following line of arguments. Assuming a simple scaling model for the magnetic energy density, $\varepsilon_B \propto n_{\rm e}$, in Eqns. (A9) and (A13) will cause these momentum scales to become independent of density, as modelled in Fig. A2 with *dotted lines*. Eventually, the enhancement of the magnetic field strength through turbulent dynamo processes will saturate on a level which is determined by the strength of the magnetic back-reaction (e.g., Subramanian 2003). For illustrative purposes in Fig. A2, we model such a saturation effect with a simple model, $\varepsilon_B = \varepsilon_{B_0}\,(1 - \exp(n_{\rm e}/n_{\rm e_0}))$, where we chose $B_{\rm max} = 10\,\mu$G and $n_{\rm e_0} = 10^{-2}$ cm^{-3}. This causes the transition to the broken power-law CR electron spectrum to occur at the higher critical electron density

$$n_{\rm e,crit} = 10^{-2}\ {\rm cm}^{-3}\left(\frac{\varepsilon_{B_{\rm max}} + \varepsilon_{\rm CMB}}{\varepsilon_{\rm CMB}}\right), \qquad \text{(A15)}$$

where $\varepsilon_{B_{\rm max}} = B_{\rm max}^2/(8\pi)$ and we assumed a plasma of primordial composition with a hydrogen mass fraction of $X_{\rm H} = 0.76$ and full ionisation. These modifications due to synchrotron losses cause a curvature of the straight lines in the log-log representation in Fig. A2 of the original power-law dependencies on $n_{\rm e}$. As before, shown in red is the spectral cutoff and spectral break, respectively, above which the hadronic injection and IC/synchrotron cooling established a steady state spectrum.

A3 Shock-accelerated electron population

A3.1 Injection spectrum

In this section, we discuss electron acceleration processes at shock waves due to gas accretion and galaxy mergers, using the framework of *diffusive shock acceleration* using the thermal leakage model originally proposed by Ellison et al. (1981). Our description follows the approach of Enßlin et al. (2007) for the acceleration of CR protons. The shock surface separates two regions: the *upstream regime* defines the region in front of the shock which is causally unconnected for super sonic shock waves, whereas the wake of the shock wave defines the *downstream regime*. The shock front itself is the region in which the mean plasma velocity changes rapidly on a scale of the order of the plasma skin depth. In the rest frame of the shock, particles are impinging onto the shock surface at a rate per unit area of $\rho_2\upsilon_2 = \rho_1\upsilon_1$. Here υ_1 and υ_2 give the plasma velocities (relative to the shock's rest frame) in the upstream and downstream regimes of the shock, respectively. The corresponding mass densities are denoted by ρ_1 and ρ_2.

We assume that after passing though the shock front most of the electron gas thermalizes to a Maxwell-Boltzmann distribution with characteristic post-shock temperature T_2 and the dimensionless electron momentum $p = P_\mathrm{e}\,(m_\mathrm{e}c)^{-1}$:

$$f_\mathrm{e}(p) = 4\pi\, n_\mathrm{e} \left(\frac{m_\mathrm{e}c^2}{2\pi\, kT_2}\right)^{3/2} p^2 \exp\left(-\frac{m_\mathrm{e}c^2\, p^2}{2\, kT_2}\right), \tag{A16}$$

where the number density of electrons of the thermal distribution in the downstream regime, $n_\mathrm{e} = n_2$, as well as T_2 can be inferred by means of the mass, momentum, and energy conservation laws at the shock surface for a gas composed of relativistic particles and thermal constituents. Note that we use an effective one-dimensional distribution function $f(p) \equiv 4\pi p^2\, f^{(3)}(p)$. In our simulations, we follow the spatial and temporal evolution of the hydrodynamic quantities such as temperature and density (although for brevity we suppress this in our notation). For cosmological applications, we have to consider the primordial composition of the cosmological fluid, i.e. the ionised electron number density is given by $n_\mathrm{e} = X_\mathrm{H} x_\mathrm{e}\rho/m_\mathrm{p}$, where $X_\mathrm{H} = 0.76$ is the primordial hydrogen mass fraction, and x_e is the ratio of electron and hydrogen number densities which we dynamically track in our radiative simulations. Assuming that a fraction of the thermalized particles experience stochastic shock acceleration by diffusing back and forth over the shock front, the test particle theory of diffusive shock acceleration predicts a resulting CR power-law distribution in momentum space. Within our model, this CR injection mechanism can be treated as an instantaneous process.

For a particle in the downstream region of the shock to return upstream it is necessary to meet two requirements. The particle's effective velocity component parallel to the shock normal has to be larger than the velocity of the shock wave, and secondly, its energy has to be large enough to escape the "trapping" process by Alfvén waves that are generated in the downstream turbulence (Malkov & Völk 1995; Malkov & Völk 1998). Thus, only particles of the high-energy tail of the distribution are able to return to the upstream shock regime in order to become accelerated. The complicated detailed physical processes of the specific underlying acceleration mechanism are conveniently compressed into a few parameters (Jones & Kang 1993; Berezhko et al. 1994; Kang & Jones 1995), one of which defines the momentum threshold for the particles of the thermal distribution to be accelerated,

$$q_\mathrm{inj} = x_\mathrm{inj}\, p_\mathrm{e} = x_\mathrm{inj} \sqrt{\frac{2\, kT_2}{m_\mathrm{e}c^2}}. \tag{A17}$$

In the linear regime of CR electron acceleration, the thermal distribution joins in a smooth manner into the resulting CR electron power-law distribution at q_inj so that x_inj represents the only parameter in our simplified diffusive shock acceleration model,

$$f_\mathrm{lin}(p) = f_\mathrm{e}(q_\mathrm{inj}) \left(\frac{p}{q_\mathrm{inj}}\right)^{-\alpha_\mathrm{inj}} \theta(p - q_\mathrm{inj}). \tag{A18}$$

The slope of the injected CR electron spectrum is given by

$$\alpha_\mathrm{inj} = \frac{r+2}{r-1}, \quad \text{where} \quad r = \frac{\rho_2}{\rho_1} = \frac{\upsilon_1}{\upsilon_2} \tag{A19}$$

denotes the shock compression ratio (Bell 1978a,b; Drury 1983a). In combination with the slope α_inj, the value of x_inj regulates the amount of kinetic energy which is transferred to the CR electrons. Theoretical and observational studies of shock acceleration of CR protons at galactic supernova remnants suggest a range of $x_\mathrm{inj} \simeq 3.3$ to 3.6, implying a particle injection efficiency of $\eta_\mathrm{lin} \simeq 10^{-4}$ to 10^{-3} (Drury et al. 1989; Jones & Kang 1993; Berezhko et al. 1994; Kang & Jones 1995; Malkov & Völk 1995; Ellison 2000; Hughes et al. 2000; Warren et al. 2005). In the linear regime, the number density of injected electrons is given by

$$\Delta n_\mathrm{lin} = \int_0^\infty \mathrm{d}p\, f_\mathrm{lin}(p) = f_\mathrm{e}(q_\mathrm{inj})\, \frac{q_\mathrm{inj}}{\alpha_\mathrm{inj} - 1}. \tag{A20}$$

This enables us to infer the particle injection efficiency which is a measure of the fraction of downstream thermal gas particles which experience diffusive shock acceleration,

$$\eta_\mathrm{lin} \equiv \frac{\Delta n_\mathrm{lin}}{n_\mathrm{e}} = \frac{4}{\sqrt{\pi}}\, \frac{x_\mathrm{inj}^3}{\alpha_\mathrm{inj} - 1}\, \mathrm{e}^{-x_\mathrm{inj}^2}. \tag{A21}$$

The particle injection efficiency is independent of the downstream post-shock temperature T_2. These considerations allow us to infer the injected electron energy density in the linear regime:

$$\Delta\varepsilon_\mathrm{lin} = \eta_\mathrm{lin} E_\mathrm{e}^\mathrm{inj}(\alpha_\mathrm{inj}, q_\mathrm{inj})\, n_\mathrm{e}(T_2). \tag{A22}$$

The average kinetic energy of $E_\mathrm{e}^\mathrm{inj}(\alpha_\mathrm{inj}, q_\mathrm{inj})$ of an injection power-law spectrum with CR electron spectral index α_inj and lower momentum cutoff q_inj is given by

$$\begin{aligned} E_\mathrm{e}^\mathrm{inj} &= \frac{\varepsilon_\mathrm{inj}}{n_\mathrm{inj}} = n_\mathrm{inj}^{-1} \int_0^\infty \mathrm{d}p\, f_\mathrm{inj}(p)\, E(p) \\ &= m_\mathrm{e}\, c^2 \left[\frac{q^{\alpha-1}}{2}\, \mathcal{B}_{\frac{1}{1+q^2}} \left(\frac{\alpha-2}{2}, \frac{3-\alpha}{2}\right) + \sqrt{1+q^2} - 1\right], \end{aligned} \tag{A23}$$

where $E(p) = (\sqrt{1+p^2} - 1)\, m_\mathrm{e}\, c^2$ is the kinetic energy of an electron with momentum p, the electron distribution function f_inj is given by Eqn. (A27), and we used the abbreviations $\alpha = \alpha_\mathrm{inj}$ and $q = q_\mathrm{inj}$. $\mathcal{B}_x(a, b)$ denotes the incomplete beta-function (Abramowitz & Stegun 1965), assuming $\alpha > 2$. In our description, the CR electron energy injection efficiency in the linear regime is defined to be the energy density ratio of freshly injected CR electrons to the total dissipated energy density in the downstream regime,

$$\zeta_\mathrm{lin} = \frac{\Delta\varepsilon_\mathrm{lin}}{\Delta\varepsilon_\mathrm{diss}}, \quad \text{where} \quad \Delta\varepsilon_\mathrm{diss} = \varepsilon_\mathrm{e2} - \varepsilon_\mathrm{e1} r^\gamma. \tag{A24}$$

The dissipated energy density in the downstream regime, $\Delta\varepsilon_\mathrm{diss}$, is given by the difference of the thermal energy densities in the pre- and post-shock regimes, corrected for the contribution of the adiabatic part of the energy increase due to the compression of the gas over the shock.

In order to obey energy conservation as well as the saturation effect for strong shocks, we propose the following modification of the electron injection efficiency at high values of the Mach number:

$$\zeta_{\mathrm{inj}} = \left[1 - \exp\left(-\frac{\zeta_{\mathrm{lin}}}{\zeta_{\mathrm{max}}}\right)\right] \zeta_{\mathrm{max}}. \tag{A25}$$

Keshet et al. (2003) suggest a value of $\zeta_{\mathrm{max}} \simeq 0.05$ for the limiting case of the electron energy injection efficiency. One can then infer the injected CR electron energy density in terms of the energy injection efficiency of diffusive shock acceleration processes,

$$\Delta\varepsilon_{\mathrm{inj}} = \zeta_{\mathrm{inj}} \Delta\varepsilon_{\mathrm{diss}}. \tag{A26}$$

Putting these considerations together, one arrives at the injection spectrum for the electrons,

$$f_{\mathrm{inj}}(p)\mathrm{d}p = C_{\mathrm{inj}}\, p^{-\alpha_{\mathrm{inj}}}\, \theta(p - q_{\mathrm{inj}})\mathrm{d}p, \tag{A27}$$

$$C_{\mathrm{inj}} = \left(1 - \mathrm{e}^{-\delta}\right) \delta^{-1}\, f_{\mathrm{e}}(q_{\mathrm{inj}})\, q_{\mathrm{inj}}^{\alpha_{\mathrm{inj}}}, \tag{A28}$$

$$\delta = \frac{\Delta\varepsilon_{\mathrm{e,lin}}}{\zeta_{\mathrm{max}}\, \Delta\varepsilon_{\mathrm{diss}}} \simeq \frac{\eta_{\mathrm{e,lin}}\, E_{\mathrm{e}}^{\mathrm{inj}}(\alpha_{\mathrm{inj}}, q_{\mathrm{inj}})}{\zeta_{\mathrm{max}}\, \dot{E}_{\mathrm{diss}} \tau_{\mathrm{shock}}}, \tag{A29}$$

$$f_{\mathrm{e}}(q_{\mathrm{inj}}) = \frac{4}{\pi}\, n_{\mathrm{e}}\, x_{\mathrm{inj}}^3\, q_{\mathrm{inj}}^{-1} \mathrm{e}^{-x_{\mathrm{inj}}^2}, \tag{A30}$$

where $\dot{E}_{\mathrm{diss}} = \dot{E}_{\mathrm{diss,\,SPH}}\, m_{\mathrm{p}}/(M_{\mathrm{SPH}}\, X_{\mathrm{H}}\, x_{\mathrm{e}})$ denotes the dissipated energy per timestep and per electron and $\tau_{\mathrm{shock}} = f_h h/\upsilon$ is the time it takes the particle to pass through the broadened shock front. The front has a characteristic length scale that is a multiple of the SPH smoothing length h (with $f_h = 2$), and one may approximate υ with the pre-shock velocity $\upsilon_1 = \mathcal{M}_1 c_{\mathrm{s}1}$.

A3.2 Equilibrium spectrum of shock accelerated electrons

This section describes the steady-state approximation for the equilibrium CR electron spectrum. This is only justified if the dynamical and diffusive timescales are long compared to the shock injection or IC/synchrotron timescale. This may well be the case in clusters of galaxies, however, probably not in our own Galaxy. Moreover, this section neglects possible re-acceleration processes of CR electrons like continuous in-situ acceleration via resonant pitch angle scattering by compressible MHD modes.

The steady-state CR electron spectrum at high energies $p = \beta\gamma > \mathrm{GeV}/c$ is governed by the injection of shock-accelerated CR electrons, denoted by the source function s_{e}, and their cooling processes so that it can be described by the continuity equation

$$\frac{\partial}{\partial p}\left[\dot{p}(p) f_{\mathrm{e}}(p)\right] = s_{\mathrm{e}}(p)\,. \tag{A31}$$

For $\dot{p}(p) < 0$, this equation is solved by

$$f_{\mathrm{e}}(p) = \frac{1}{|\dot{p}(p)|} \int_p^\infty \mathrm{d}p'\, s_{\mathrm{e}}(p')\,. \tag{A32}$$

For the energy range of interest, the cooling of the radio emitting CR electrons is dominated by synchrotron and inverse Compton losses, $\dot{p}_{\mathrm{IC,synch}} = \dot{E}_{\mathrm{IC,synch}}/(m_{\mathrm{e}}c^2)$ where $\dot{E}_{\mathrm{IC,synch}}$ is given by Eqn. (A7). The source function of the shock-accelerated CR electrons for the energy range of interest is given by

$$s_{\mathrm{e}}(p) = \frac{f_{\mathrm{inj}}(p)}{\tau_{\mathrm{inj}}} \tag{A33}$$

In our formalism, we set $\tau_{\mathrm{inj}} = \min(\tau_{\mathrm{shock}}, \tau_{\mathrm{Hubble}})$ using τ_{shock} of Eqn. (A29) due to the following line of arguments: the freshly accelerated relativistic electron population in post-shock regions cools and finally diminishes as a result of loss processes. In the interesting observational bands such as inverse Compton (IC) γ-rays and radio synchrotron emission the electron population diminishes on such a short timescale that we could describe this by instantaneous cooling. In this approximation, there is no steady-state electron population and we would have to convert the energy from the electrons to IC and synchrotron radiation. However, we can introduce a virtual electron population that lives in the SPH broadened shock volume only which is defined to be the volume of energy dissipation. Within this volume that is comoving with the shock, we can indeed use the steady state solution for the distribution function of relativistic electrons and we assume no relativistic electrons in the post-shock volume where there is no energy dissipation. Thus, the cooled CR electron equilibrium spectrum can be derived from Eqn. (A32) yielding

$$f_{\mathrm{e}}(p)\,\mathrm{d}p = C_{\mathrm{e}}\, p^{-\alpha_{\mathrm{e}}}\, \mathrm{d}p, \tag{A34}$$

$$C_{\mathrm{e}} = \frac{3\, C_{\mathrm{inj}}\, m_{\mathrm{e}} c}{4\, (\alpha_{\mathrm{e}} - 2)\, \sigma_{\mathrm{T}}\, \tau_{\mathrm{inj}}\, (\varepsilon_B + \varepsilon_{\mathrm{ph}})} \tag{A35}$$

Here, $\alpha_{\mathrm{e}} = \alpha_{\mathrm{inj}} + 1$ is the spectral index of the equilibrium electron spectrum. The normalisation scales linearly with the gas density $C_{\mathrm{e}} \propto \rho$ which we evolve dynamically in our simulations and depends indirectly on α_{inj} and $\dot{E}_{\mathrm{diss}}$ through the variable C_{inj}.

At high energies, we have the IC/synchrotron cooled power-law electron spectrum that joins at lower energies into the shock injection spectrum which has had no time to cool radiatively yet. The low-energy regime of the CR electron distribution function is determined by Coulomb losses. It turns out that the timescale associated with the momentum scale $q_{\mathrm{Coul,IC/synch}}$ is always larger than the injection timescale τ_{inj} such that the transition from the injection spectrum (A27) to the cooled equipartition spectrum (A34) takes place at the characteristic momentum

$$q_{\mathrm{break,prim}} = \frac{3\, m_{\mathrm{e}} c}{4\, (\alpha_{\mathrm{e}} - 2)\, \sigma_{\mathrm{T}} \tau_{\mathrm{inj}}\, (\varepsilon_B + \varepsilon_{\mathrm{ph}})}. \tag{A36}$$

The injection spectrum extends down to the lower cutoff $q_{\mathrm{min,prim}} = \max(q_{\mathrm{inj}}, q_{\mathrm{inj,Coul}})$ where q_{inj} and $q_{\mathrm{inj,Coul}}$ are given by Eqns. (A17) and (A11), respectively.

The pressure of a CR electron or proton power-law population as e.g. described by Eqn. (A34), that is characterised by two momentum cutoffs p_1 and p_2 is given by

$$P_{\mathrm{CR}} = \frac{mc^2}{3} \int_0^\infty \mathrm{d}p\, f(p) \beta\, p \tag{A37}$$

$$= \frac{C\, mc^2}{6} \left[\mathcal{B}_{\frac{1}{1+p^2}} \left(\frac{\alpha - 2}{2}, \frac{3 - \alpha}{2}\right)\right]_{p_2}^{p_1}, \tag{A38}$$

where $\beta := \upsilon/c = p/\sqrt{1 + p^2}$ is the dimensionless velocity of the CR particle. The CR population can hydrodynamically be described by an isotropic pressure component as long as the CRs are coupled to the thermal gas by small scale chaotic magnetic fields. Note, that for $2 < \alpha < 3$ the kinetic energy density and pressure of the CR populations are well defined for the limit $q \to 0$, although the total CR number density diverges.

A4 Hadronically produced electron population

Considering CR protons, which are at least in our Galaxy the dominant CR species, it is convenient to introduce the dimensionless proton momentum $p_\mathrm{p} = P_\mathrm{p}/(m_\mathrm{p}\,c)$. We assume that the differential particle momentum spectrum per volume element can be approximated by a single power-law:

$$f_\mathrm{p}(p_\mathrm{p}) = \frac{\mathrm{d}N}{\mathrm{d}p_\mathrm{p}\,\mathrm{d}V} = C_\mathrm{p}\,p_\mathrm{p}^{-\alpha_\mathrm{p}}\,\theta(p_\mathrm{p} - q_\mathrm{p}), \qquad \text{(A39)}$$

where $\theta(x)$ denotes the Heaviside step function, $C_\mathrm{p} = C_\mathrm{p}(\boldsymbol{x}, t)$ denotes the normalisation, $q_\mathrm{p} = q_\mathrm{p}(\boldsymbol{x}, t)$ is the lower cutoff of the distribution function, and α_p is the CR spectral index that is taken to be constant in space and time for simplicity. In our simulation, we dynamically evolve the quantities C_p and q_p according to the dominant gain and loss processes in the intra-cluster medium. The modelling of the cosmic ray physics includes adiabatic CR transport processes, injection by supernovae and cosmological structure formation shocks, as well as CR thermalization by Coulomb interaction and catastrophic losses by hadronic interactions. As already laid out in the introduction, the hadronic reaction of CR protons with ambient thermal protons produces pions which decay into secondary electrons, positrons, neutrinos and γ-rays.

There are two analytical models in the literature that describe the hadronic proton-proton reaction while assuming isospin symmetry. Fermi (1950) proposed the *fireball model* which assumes a state of hot quark-gluon plasma in thermal equilibrium after the hadronic interaction that subsequently ablates pions with energy dependent multiplicities. Since this model is only valid in the high-energy limit for CR protons, we use the analytic formalism by Pfrommer & Enßlin (2004a) that parametrises important effects near the pion threshold and is based on an approximate description developed by Dermer (1986a,b), which combines isobaric (Stecker 1970) and scaling models (Badhwar et al. 1977; Stephens & Badhwar 1981) of the hadronic reaction.

A4.1 Injection spectrum

The pion production spectrum can be derived from general considerations including branching ratios and multiplicities of the hadronic reaction (Stecker 1971). The pion production spectrum describes the produced number of pions per unit time, volume and momentum intervals, $\mathrm{d}N/(\mathrm{d}t\,\mathrm{d}V\,\mathrm{d}p_\pi\,\mathrm{d}p_\mathrm{p})$, and reads in this context

$$s_\pi(p_\pi, p_\mathrm{p}) = c n_\mathrm{N} \xi(p_\mathrm{p}) \sigma^\pi_\mathrm{pp}(p_\mathrm{p}) \delta_\mathrm{D}(p_\pi - \langle p_\pi\rangle) \theta(p_\mathrm{p} - p_\mathrm{p,th}), \qquad \text{(A40)}$$

where $n_\mathrm{N} = n_\mathrm{H} + 4n_\mathrm{He} = \rho/m_\mathrm{p}$ is the target density of nucleons in a fluid of primordial element composition, σ^π_pp the inelastic p-p cross section, $\langle p_\pi\rangle$ the average momentum of a single produced pion, and $p_\mathrm{p,th} = 0.78$ denotes the threshold momentum for pion production. For a differential CR proton distribution, the pion source function can be marginalised over the proton energy, yielding

$$s_{\pi^\pm}(p_\pi) = \frac{2}{3} q_\pi(p_\pi) = \frac{2}{3} \int_{-\infty}^{\infty} \mathrm{d}p_\mathrm{p}\, f_\mathrm{p}(p_\mathrm{p}) s_\pi(p_\pi, p_\mathrm{p}), \qquad \text{(A41)}$$

where the CR proton population is given by Eqn. (A39). The scaling behaviour in the high-energy limit of Dermer's model can be described by a constant pion multiplicity $\xi(p_\mathrm{p}) \simeq \xi = 2$ and the dependence of the mean pion momentum is given by $\langle p_{\pi^\pm}\rangle = m_\mathrm{p} p_\mathrm{p}/(2 m_{\pi^\pm}\xi)$. The weak energy dependencies of the pion multiplicity and the inelastic cross section can be absorbed in a semi-analytical parametrisation of the cross section, $\sigma^\pi_\mathrm{pp}(\alpha_\mathrm{p})$ (for details see Pfrommer & Enßlin 2004a). The mean energy of the produced secondary electrons ($\pi^\pm \to e^\pm + 3\nu$) in the laboratory frame is given by $\langle E_\mathrm{e}\rangle = \frac{1}{4}\langle E_{\pi^\pm}\rangle$. Employing the transformation law for distribution functions and using the mean value of the electron momentum in the relativistic limit allows us to approximate the electron source function by

$$s_\mathrm{e}(p)\,\mathrm{d}p = s_{\pi^\pm}[p_\pi(p)] \frac{\mathrm{d}p_\pi}{\mathrm{d}p}\,\mathrm{d}p = \frac{4 m_\mathrm{e}}{m_{\pi^\pm}} s_{\pi^\pm}\left(\frac{4 m_\mathrm{e}}{m_{\pi^\pm}}\,p\right)\mathrm{d}p \qquad \text{(A42)}$$

$$= \frac{4}{3}\,16^{1-\alpha_\mathrm{p}} c\,\sigma_\mathrm{pp}\,n_\mathrm{N}\,C_\mathrm{p}\left(\frac{m_\mathrm{e}}{m_\mathrm{p}}\right)^{1-\alpha_\mathrm{p}} p^{-\alpha_\mathrm{p}}\,\mathrm{d}p, \qquad \text{(A43)}$$

where the effective cross section σ_pp depends in our model on the spectral index of the CRp spectrum α_p according to

$$\sigma_\mathrm{pp} \simeq 32 \cdot \left(0.96 + \mathrm{e}^{4.4\,-\,2.4\,\alpha_\mathrm{p}}\right)\ \mathrm{mbarn}. \qquad \text{(A44)}$$

Thus, we can write down the injection spectrum for CR electrons resulting from hadronic reactions of CR protons with ambient gas protons,

$$f_\mathrm{inj,pp}\,\mathrm{d}p = C_\mathrm{inj,pp}\,p^{-\alpha_\mathrm{p}}\,\mathrm{d}p \qquad \text{(A45)}$$

$$C_\mathrm{inj,pp} = \frac{4}{3}\,16^{2-\alpha_\mathrm{e}} c\,\tau_\mathrm{pp}\,\sigma_\mathrm{pp}\,n_\mathrm{N}\,C_\mathrm{p}\left(\frac{m_\mathrm{e}}{m_\mathrm{p}}\right)^{2-\alpha_\mathrm{e}}, \qquad \text{(A46)}$$

and $\tau_\mathrm{pp} = \min[(c\,\sigma_\mathrm{pp} n_\mathrm{N})^{-1}, \tau_\mathrm{Hubble}]$, and $\alpha_\mathrm{e} = \alpha_\mathrm{p} + 1$.

A4.2 Equilibrium spectrum of secondary electrons

The same line of arguments presented in Sec. A3.2 allows us to derive the equilibrium distribution of secondary CR electrons above a GeV due to IC and synchrotron cooling,

$$f_\mathrm{e}(p)\,\mathrm{d}p = C_\mathrm{e}\,p^{-\alpha_\mathrm{e}}\,\mathrm{d}p \qquad \text{(A47)}$$

$$C_\mathrm{e} = \frac{16^{2-\alpha_\mathrm{e}}\sigma_\mathrm{pp}\,n_\mathrm{N} C_\mathrm{p}\,m_\mathrm{e}\,c^2}{(\alpha_\mathrm{e} - 2)\,\sigma_\mathrm{T}\,(\varepsilon_B + \varepsilon_\mathrm{ph})}\left(\frac{m_\mathrm{p}}{m_\mathrm{e}}\right)^{\alpha_\mathrm{e}-2}, \qquad \text{(A48)}$$

where the effective CR-proton cross section σ_pp is given by Eqn. (A44), and $n_\mathrm{N} = n_\mathrm{H} + 4n_\mathrm{He} = \rho/m_\mathrm{p}$ is the target density of nucleons in a fluid of primordial element composition. As discussed in Sect. A2, the equilibrium spectrum of secondary electrons looks different depending on the ambient electron density relative to the critical electron density (A15). At average ICM densities below $n_\mathrm{e,crit}$, the equilibrium spectrum is given by the IC/synchrotron cooled spectrum (A47) with the lower cutoff

$$q_\mathrm{min,sec} = \max(q_\mathrm{Coul,IC/synch}, q_\mathrm{threshold}, q_\mathrm{pp}), \qquad \text{(A49)}$$

where $q_\mathrm{pp} = q_\mathrm{p} m_\mathrm{p}/(16 m_\mathrm{e})$ is the lower cutoff of the injected electron population that is inherited from the lower proton cutoff q_p, while $q_\mathrm{Coul,IC/synch}$ and $q_\mathrm{threshold}$ are given by Eqns. (A9) and (A12), respectively.

In the high ICM densities/ISM-regime above $n_\mathrm{e,crit}$, the equilibrium spectrum is given by the injection spectrum (A45) at low energies between $q_\mathrm{min,sec}$ and

$$q_\mathrm{break,sec} = \frac{q_\mathrm{pp,IC/synch}}{\alpha_\mathrm{e} - 2}. \qquad \text{(A50)}$$

Above $q_\mathrm{break,sec}$, the equipartition spectrum steepens and and joins continuously into the IC/synchrotron cooled spectrum (A47).

APPENDIX B: RADIATIVE PROCESSES

The non-thermal radio and hard X-ray emission is generated by CR electrons with energies $E_\mathrm{e} >$ GeV (cf. Eqns. (1) and (2)). For convenience, we rescale the cooled CR electron equilibrium spectra of Eqns. (A34) and (A47) to the energy scale of a GeV,

$$f_\mathrm{e}(E_\mathrm{e})\mathrm{d}E_\mathrm{e} = \frac{\tilde{C}_\mathrm{e}}{\mathrm{GeV}}\left(\frac{E_\mathrm{e}}{\mathrm{GeV}}\right)^{-\alpha_\mathrm{e}}\mathrm{d}E_\mathrm{e}, \qquad \text{(B1)}$$

$$\tilde{C}_\mathrm{e} = C_\mathrm{e}\left(\frac{m_\mathrm{e}c^2}{\mathrm{GeV}}\right)^{\alpha_\mathrm{e}-1}, \tag{B2}$$

and C_e is given by Eqn. (A35) respectively (A48), depending on the electron population.

B1 Cluster magnetic fields

In principle, cosmological structure formation calculations with SPH are capable of following magneto-hydrodynamics (Dolag et al. 1999, 2005; Price & Monaghan 2004, 2005), although this is presently still fraught with numerical and physical difficulties. Secondly, the origin of cluster magnetic fields is still an open question (Widrow 2002, and references therein). There are studies of the Faraday rotation measure (RM) as a function of cluster impact parameter using the position of a sample of radio lobes in different clusters (Clarke et al. 2001) which hints at a magnetic profile centred on the cluster with μG field strengths. Field reversals along the line-of-sight lead to cancellations in RM, since $RM \propto \int n_\mathrm{e}\boldsymbol{B}\cdot\mathrm{d}\boldsymbol{l}$. The unknown behaviour of the characteristic length scale of the magnetic field with cluster radius leaves us with some degree of freedom for the magnetic profile that is unconstrained by current observations. Assuming primordial origin, and amplification of magnetic fields in the process of structure formation would still require scanning the parameter space of the field strengths in the initial conditions (Dolag et al. 1999).

Thus, we refrain from running self-consistent MHD simulations on top of the radiative gas and CR physics and postpone a detailed analysis of the influence of MHD on the radio emission to future work. We chose the following simple model for the magnetic energy density:

$$\varepsilon_B = \varepsilon_{B,0}\left(\frac{\varepsilon_\mathrm{th}}{\varepsilon_\mathrm{th,0}}\right)^{2\alpha_B}, \tag{B3}$$

where $\varepsilon_{B,0}$ and α_B are free parameters in our model. Rather than applying a scaling with the gas density as non-radiative MHD simulations by Dolag et al. (1999, 2001) suggest, we chose the energy density of the thermal gas. This quantity is well behaved in the centres of clusters where current cosmological radiative simulations, that do not include feedback from AGN, have an overcooling problem which results in an overproduction of the amount of stars, enhanced central gas densities, too small central temperatures, and too strong central entropy plateaus compared to X-ray observations. Theoretically, the growth of magnetic field strength is determined through turbulent dynamo processes that will saturate on a level which is determined by the strength of the magnetic backreaction (e.g., Subramanian 2003; Schekochihin & Cowley 2006) and is typically a fraction of the turbulent energy density that itself should be related to the thermal energy density, thus motivating our model theoretically.

B2 Synchrotron radiation

The synchrotron emissivity j_ν at frequency ν and per steradian of a CR electron population described by Eqn. (B1), which is located in an isotropic distribution of magnetic fields (Eqn. (6.36) in Rybicki & Lightman 1979), is obtained after averaging over an isotropic distribution of electron pitch angles, yielding

$$j_\nu = A_{E_\mathrm{synch}}(\alpha_\mathrm{e})\,\tilde{C}_\mathrm{e}\left[\frac{\varepsilon_B}{\varepsilon_{B_\mathrm{c}}}\right]^{(\alpha_\nu+1)/2} \propto \varepsilon_\mathrm{CRe}\,B^{\alpha_\nu+1}\nu^{-\alpha_\nu}, \tag{B4}$$

$$B_\mathrm{c} = \sqrt{8\pi\,\varepsilon_{B_\mathrm{c}}} = \frac{2\pi\,m_\mathrm{e}^3\,c^5\,\nu}{3\,e\,\mathrm{GeV}^2} \simeq 31\left(\frac{\nu}{\mathrm{GHz}}\right)\mu\mathrm{G}, \tag{B5}$$

$$A_{E_\mathrm{synch}} = \frac{\sqrt{3\pi}}{32\pi}\,\frac{B_\mathrm{c}\,e^3}{m_\mathrm{e}c^2}\,\frac{\alpha_\mathrm{e}+\frac{7}{3}}{\alpha_\mathrm{e}+1}\,\frac{\Gamma\left(\frac{3\alpha_\mathrm{e}-1}{12}\right)\Gamma\left(\frac{3\alpha_\mathrm{e}+7}{12}\right)\Gamma\left(\frac{\alpha_\mathrm{e}+5}{4}\right)}{\Gamma\left(\frac{\alpha_\mathrm{e}+7}{4}\right)}, \tag{B6}$$

where $\Gamma(a)$ denotes the Γ-function (Abramowitz & Stegun 1965), $\alpha_\nu = (\alpha_\mathrm{e}-1)/2 = \alpha_\mathrm{inj}/2$, $\tilde{C}_\mathrm{e}$ is given by Eqn. (B2), and B_c denotes a (frequency dependent) characteristic magnetic field strength which implies a characteristic magnetic energy density $\varepsilon_{B_\mathrm{c}}$. Line-of-sight integration of the radio emissivity j_ν yields the surface brightness of the radio emission S_ν.

For later convenience, we calculate the radio luminosity per unit frequency interval of a steady state population of hadronically generated electrons (A47),

$$L_\nu = 4\pi\int\mathrm{d}V\,j_\nu = A_\nu\int\mathrm{d}V\,C_\mathrm{p}n_\mathrm{N}\,\frac{\varepsilon_B}{\varepsilon_B+\varepsilon_\mathrm{ph}}\left(\frac{\varepsilon_B}{\varepsilon_{B_\mathrm{c}}}\right)^{(\alpha_\nu-1)/2}$$
$$\simeq A_\nu\int\mathrm{d}V\,C_\mathrm{p}n_\mathrm{N},\ \text{for } \varepsilon_B \gg \varepsilon_\mathrm{ph}, \tag{B7}$$

$$A_\nu = 4\pi\,A_{E_\mathrm{synch}}\,\frac{16^{2-\alpha_\mathrm{e}}\sigma_\mathrm{pp}\,m_\mathrm{e}\,c^2}{(\alpha_\mathrm{e}-2)\,\sigma_\mathrm{T}\,\varepsilon_{B_\mathrm{c}}}\left(\frac{m_\mathrm{p}}{m_\mathrm{e}}\right)^{\alpha_\mathrm{e}-2}\left(\frac{m_\mathrm{e}c^2}{\mathrm{GeV}}\right)^{\alpha_\mathrm{e}-1}, \tag{B8}$$

where we introduced the abbreviation A_ν with the dimensions $[A_\nu] = \mathrm{erg\ cm^3\ s^{-1}\ Hz^{-1}}$ and the volume integral extends over the entire cluster. In the last step of Eqn. (B7), we assumed typical radio spectral indices of cluster radio halos of $\alpha_\nu \sim 1$ such that the radio luminosity of the equilibrium distribution of CR electrons becomes independent of the magnetic field in the synchrotron dominated regime for $\varepsilon_B \gg \varepsilon_\mathrm{ph}$ (cf. Fig. 3).

B3 Inverse Compton radiation

Inverse Compton (IC) scattering of cosmic microwave background (CMB) photons off ultra-relativistic electrons with Lorentz factors of $\gamma_\mathrm{e} \sim 10^4$ redistributes these photons into the hard X-ray regime according to Eqn. (2). The integrated IC source density λ_IC for an isotropic power law distribution of CR electrons as described by Eqn. (A34) or (A47), can be obtained by integrating the IC source function $s_\gamma(E_\gamma)$ in Eqn. (43) of Pfrommer & Enßlin (2004a) (in the case of Thomson scattering) over an energy interval between observed photon energies E_1 and E_2 yielding

$$\lambda_\mathrm{IC}(E_1,E_2) = \int_{E_1}^{E_2}\mathrm{d}E_\mathrm{IC}\,s_\mathrm{IC}(E_\mathrm{IC}) \tag{B9}$$

$$= \tilde{\lambda}_0\,f_\mathrm{IC}(\alpha_e)\left(\frac{m_\mathrm{e}\,c^2}{\mathrm{GeV}}\right)^{1-\alpha_\mathrm{e}}\left[\left(\frac{E_\mathrm{IC}}{kT_\mathrm{CMB}}\right)^{-\alpha_\nu}\right]_{E_2}^{E_1}, \tag{B10}$$

$$f_\mathrm{IC}(\alpha_e) = \frac{2^{\alpha_\mathrm{e}+3}\,(\alpha_\mathrm{e}^2+4\,\alpha_\mathrm{e}+11)}{(\alpha_\mathrm{e}+3)^2\,(\alpha_e+5)\,(\alpha_e+1)} \times\Gamma\left(\frac{\alpha_e+5}{2}\right)\zeta\left(\frac{\alpha_e+5}{2}\right), \tag{B11}$$

$$\text{and } \tilde{\lambda}_0 = \frac{16\,\pi^2\,r_\mathrm{e}^2\,\tilde{C}_\mathrm{e}\,(kT_\mathrm{CMB})^3}{(\alpha_\mathrm{e}-1)\,h^3\,c^2}, \tag{B12}$$

where $\alpha_\nu = (\alpha_\mathrm{e}-1)/2$ denotes the spectral index, $r_\mathrm{e} = e^2/(m_\mathrm{e}\,c^2)$ the classical electron radius, $\zeta(a)$ the Riemann ζ-function (Abramowitz & Stegun 1965), and $\tilde{C}_\mathrm{e}$ is given by Eqn. (B2). The IC photon number flux $\mathcal{F}_\gamma$ is derived by means of volume integration over the emission region and correct accounting for the growth of the area of the emission sphere on which the photons are distributed:

$$\mathcal{F}_\gamma(E_1,E_2) = \frac{1+z}{4\pi\,D^2}\int\mathrm{d}V\,\lambda_\mathrm{IC}[(1+z)E_1,(1+z)E_2]. \tag{B13}$$

Here D denotes the luminosity distance and the additional factors of $1 + z$ account for the cosmological redshift of the photons.

B4 γ-ray emission from decaying pions

Provided the CR population has a power-law spectrum, the integrated γ-ray source density λ_γ for pion decay induced γ-rays can be obtained by integrating the γ-ray source function $s_\gamma(E_\gamma)$ (cf. Enßlin et al. 2007),

$$\lambda_\gamma = \lambda_\gamma(E_1, E_2) = \int_{E_1}^{E_2} \mathrm{d}E_\gamma\, s_\gamma(E_\gamma) \tag{B14}$$

$$= \frac{4\, C_\mathrm{p}}{3\,\alpha\delta_\gamma} \frac{m_{\pi^0} c\, \sigma_\mathrm{pp} n_\mathrm{N}}{m_\mathrm{p}} \left(\frac{m_\mathrm{p}}{2 m_{\pi^0}}\right)^\alpha \left[\mathcal{B}_x\left(\frac{\alpha+1}{2\,\delta_\gamma}, \frac{\alpha-1}{2\,\delta_\gamma}\right)\right]_{x_1}^{x_2}, \tag{B15}$$

$$x_i = \left[1 + \left(\frac{m_{\pi^0} c^2}{2\, E_i}\right)^{2\,\delta_\gamma}\right]^{-1} \quad \text{for} \quad i \in \{1, 2\}, \tag{B16}$$

where we used the abbreviation $\alpha = \alpha_\gamma$. C_p is the normalisation of the proton distribution function which we follow dynamically in our simulations (cf. Eqn. (A39)), and the rest mass of a neutral pion is $m_{\pi^0} c^2 \simeq 135\,\mathrm{MeV}$. The shape parameter δ_γ depends on the spectral index of the γ-ray spectrum α according to

$$\delta_\gamma \simeq 0.14\, \alpha_\gamma^{-1.6} + 0.44. \tag{B17}$$

There is a detailed discussion in Pfrommer & Enßlin (2004a) how the γ-ray spectral index α_γ relates to the spectral index of the parent CR population α_p. In Dermer's model, the pion multiplicity is independent of energy yielding the relation $\alpha_\gamma = \alpha$ (Dermer 1986a,b). The formalism underlying Eqns. (B14) and (B15) includes the detailed physical processes at the threshold of pion production like the velocity distribution of CRs, momentum dependent inelastic CR-proton cross section, and kaon decay channels. The γ-ray luminosity is defined by

$$\mathcal{L}_\gamma = \int \mathrm{d}V\, \lambda_\gamma = A_\gamma \int \mathrm{d}V\, C_\mathrm{p} n_\mathrm{N}, \tag{B18}$$

where we introduced the constant A_γ with the dimensions $[A_\gamma] = \gamma\,\mathrm{cm}^3\,\mathrm{s}^{-1}$ that is given by $A_\gamma = \lambda_\gamma/(C_\mathrm{p} n_\mathrm{N}) = \mathrm{const}$, according to Eqn. (B15). $\mathcal{F}_\gamma$ is derived by Eqn. (B13) substituting λ_IC by λ_γ.

B5 SPH projections and Hubble scaling

We produced projected maps of the density, Mach number of shocks, relative CR pressure of protons and electrons, and non-thermal cluster observables in the radio, hard X-ray, and γ-ray regime. Generally, a three-dimensional scalar field $a(\boldsymbol{r})$ along any ray was calculated by distributing the product of $a(\boldsymbol{r})$ and the specific volume M_α/ρ_α of the gas particles over a grid comoving with the cosmic expansion. This yields the projected quantity $A(\boldsymbol{r}_\perp)$:

$$A(\boldsymbol{r}_{\perp,ij}) = \frac{1}{L_\mathrm{pix}^2} \sum_\alpha a_\alpha \frac{M_\alpha}{\rho_\alpha} W_{\alpha,ij}(\boldsymbol{r}_{\perp,ij} - \boldsymbol{r}_\alpha), \tag{B19}$$

where $W_{\alpha,ij}$ is the value of the projected smoothing kernel (normalised to unity for the pixels covered) of an SPH particle α at comoving grid position $\boldsymbol{r}_{\perp,ij}$, and L_pix^2 is the comoving area of the pixel. In order to obtain a line-of-sight average of some mass-weighted quantity, say temperature, we project the quantity $a_\alpha = T_\alpha \rho_\alpha$ divided each pixel by the mass projection (e.g. setting $a_\alpha = \rho_\alpha$).

Combining primary and secondary non-thermal emissivities requires the knowledge of the scaling with the Hubble constant. It turns out that the primary synchrotron/IC emissivities scale as $j_{\nu/IC,\mathrm{prim}} \propto h^3$ leading to a scaling of the surface brightness of $S_{\nu/IC,\mathrm{prim}} \propto h^2$. In contrast, the secondary synchrotron/IC/γ-ray emissivities scale as $j_{\nu/IC,\mathrm{sec}} \propto h^4$ which results in a scaling of the surface brightness of $S_{\nu/IC,\mathrm{prim}} \propto h^3$. The different scaling of the primary and secondary non-thermal emission components with the Hubble constant is the reason why we choose to show all non-thermal luminosities in units of the currently favoured Hubble constant, h_{70}, where $H_0 = 70\, h_{70}\,\mathrm{km\,s^{-1}\,Mpc^{-1}}$.

This paper has been typeset from a TEX/ LATEX file prepared by the author.